NASA CR-174980
SwRI-7576/30

NASA

CONSTITUTIVE MODELING FOR ISOTROPIC MATERIALS (HOST)

(Second Annual Status Report)

By
U. S. Lindholm
K. S. Chan
S. R. Bodner
R. M. Weber
K. P. Walker
B. N. Cassenti

Southwest Research Institute
P. O. Drawer 28510
San Antonio, TX 78284

Prepared for
NATIONAL AERONAUTICS AND SPACE ADMINISTRATION
NASA-Lewis Research Center
Contract NAS3-23925

SOUTHWEST RESEARCH INSTITUTE
SAN ANTONIO HOUSTON

1 Report No.	2 Government Accession No.	3. Recipient's Catalog No.
NASA CR 174980		

4. Title and Subtitle	5. Report Date
Constitutive Modeling for Isotropic Materials	July 1985
	6. Performing Organization Code

7. Author(s)	8. Performing Organization Report No.
U. S. Lindholm, K. S. Chan, S. R. Bodner, R. M. Weber, K. P. Walker, B. N. Cassenti	SwRI Project No. 06-7576
	10. Work Unit No.

9. Performing Organization Name and Address	11. Contract or Grant No.
Southwest Research Institute Department of Materials Sciences P.O. Drawer 28510 San Antonio, TX 78284	NAS3-23925
	13. Type of Report and Period Covered
12. Sponsoring Agency Name and Address	Second Annual Report
National Aeronautics & Space Administration Washington, DC 20546	14. Sponsoring Agency Code
	RTOP 533-04-1A

15. Supplementary Notes

Project Manager, A. Kaufman
NASA Lewis Research Center (MS 49-7)
21000 Brookpark Road
Cleveland, OH 44135

16. Abstract

This report presents the results of the second year of work on a program which is part of the NASA HOST Program. The program goals are: (1) to develop and validate unified constitutive models for isotropic materials, and (2) to demonstrate their usefulness for structural analyses of hot section components of gas turbine engines. The unified models selected for development and evaluation are that of Bodner-Partom and of Walker.

For model evaluation purposes, a large constitutive data base was generated for a B1900+Hf alloy by performing uniaxial tensile, creep, cyclic, stress relaxation, and thermo-mechanical fatigue (TMF) tests as well as biaxial (tension/torsion) tests under proportional and nonproportional loading over a wide range of strain rates and temperatures. Systematic approaches for evaluating material constants from a small subset of the data base were developed. Correlations of the uniaxial and biaxial test data with the theories of Bodner-Partom and Walker were performed to establish the accuracy, range of applicability, and integrability of the models. Both models were implemented in the MARC finite element computer code and used for TMF analyses. Benchmark notch round experiments were conducted and the results were compared with finite-element analyses using the MARC code and the Walker model.

The results of this program provide strong evidence for the applicability of the unified constitutive equation approach to describe the strongly nonlinear, time and temperature dependent response of isotropic alloys to arbitrary load or deformation histories. The two models demonstrated reasonable agreement with all the experimental data generated over a very wide range of temperature, deformation rate and load cycle. In a broader sense, the models can be considered to be predictive in that the functional representations and the material constants were obtained from a small subset of the total tests performed. The practical application of the unified models depends on their adaptability in efficient computational algorithms when incorporated into finite element methods for structural analysis.

17. Key Words (Suggested by Author(s))	18. Distribution Statement
Hot Section Technology, Nonlinear Structural Analysis, Unifed Constitutive Model	Unclassified Unlimited

19. Security Classif. (of this report)	20. Security Classif. (of this page)	21. No. of pages	22. Price*
Unclassified	Unclassified		

*For sale by the National Technical Information Service, Springfield, Virginia 22161

PREFACE

This Second Annual Status Report covers the effort of the base program on the NASA HOST program titled "Constitutive Modeling for Isotropic Materials" conducted under Contract NAS3-23925. The NASA program manager for this project is Mr. Albert Kaufman. The program manager at Southwest Research Institute is Dr. Ulric Lindholm. Contributors to this report are Dr. Kwai Chan and Mr. Andrew Nagy of SwRI, Messrs. Brice Cassenti and R. M. Weber of Pratt & Whitney Aircraft, and Dr. Kevin Walker and Prof. Sol R. Bodner, consultants.

TABLE OF CONTENTS

TABLE OF CONTENTS (CONTINUED)

LIST OF FIGURES

LIST OF FIGURES (CONTINUED)

LIST OF FIGURES (CONTINUED)

LIST OF FIGURES (CONTINUED)

LIST OF FIGURES (CONTINUED)

LIST OF FIGURES (CONTINUED)

LIST OF TABLES

1.0 INTRODUCTION

The objective of the present program is to develop a unified constitutive model for finite-element structural analysis of turbine engine hot section components. This effort constitutes a different approach for non-linear finite-element computer codes which have heretofore been based on classical inelastic methods. The unified constitutive theory to be developed will avoid the simplifying assumptions of classical theory and should more accurately represent the behavior of superalloy materials under cyclic loading conditions and high temperature environments. This class of constitutive theory is characterized by the use of kinetic equations and internal variables with appropriate evolution equations for treating all aspects of inelastic deformation including plasticity, creep and stress relaxation. Model development is directed toward isotropic, cast nickel-base alloys used for air-cooled turbine blades and vanes. Recent studies have shown that this approach is particularly suited for determining the cyclic behavior of superalloy type blade and vane materials and is entirely compatible with three dimensional inelastic finite-element formulations. More efficient and accurate inelastic analysis of hot section components--turbine blades, turbine vanes, combustor liners and seals--fabricated from "age hardenable" isotropic superalloy materials will be realized as the result of these developments.

The program is being conducted in two phases. A basic program (Tasks A through I) and an optional follow-on program (Tasks J through M). In the basic program of twenty-six months' duration, a unified constitutive model will be developed for the prediction of the structural response of isotropic materials for temperatures and strain range characteristics of cooled turbine

vanes in advanced gas turbine engines (Task A). A data base of uniaxial and multiaxial material properties required for the constitutive model development will be obtained for the base material (Tasks C and E). The constitutive model will then be incorporated into a finite-element computer code (Task D). An evaluation will be made of the capability of the analytical method to predict the structural response for multiaxial stress states (Task E) and nonisothermal conditions by conducting thermomechanical loading and benchmark notch verification experiments and analysis (Task F). As a final evaluation of the analytical model, a structural analysis will be performed for a hot section component fabricated from the base material for simulated engine operating conditions (Task G). In the optional program, material property test procedures will be further developed to minimize the amount of testing required, and to study the possibility for estimating the material model constants from conventional property data (Task J). Further development of the model will be undertaken to consider thermal history effects and to correct any deficiencies indicated in the model or the computational algorithms in the code (Task K). In addition, the constitutive model development will be verified for an alternate material (Task L).

The work under this program is being conducted as a joint effort between Pratt & Whitney Aircraft (PWA) and Southwest Research Institute (SwRI) with technical assistance from Prof. Sol R. Bodner and Dr. Kevin Walker in the area of constitutive model development. The work and data base generated is being coordinated closely with another NASA funded HOST program at PWA (NAS3-23288) to develop advanced life prediction techniques for isotropic superalloy vane and blade materials.

This report documents the efforts in the base program (Task A through I). Although efforts in certain tasks were completed and reported last year [1], some of those results will also be included in this report for the sake of clarity and completeness.

2.0 MATERIAL AND CONSTITUTIVE MODELS SELECTION

2.1 Material Selection

The model material selected for study in the base program is B1900+Hf and MAR-M247 has been chosen for the optional tasks. Both materials are extensively utilized in the gas turbine industry and considerable benefit will derive from their characterization. A major factor in the selection of B1900+Hf is the availability of cyclic and monotonic constitutive data from a concurrent NASA HOST program, NAS3-23288, conducted by PWA to develop life prediction analysis methodology for isotropic blades and vanes. Selection of the same material, material processing, and specimen configurations in both efforts significantly enhances the data base available for life prediction and constitutive model development.

The B1900+Hf material was part of a single heat, designated W-0098, obtained from Certified Alloy Products Inc., Long Beach, California. The chemical composition of this heat is compared to nominal specification in Table 2.1. Casting configurations, pour and mold temperatures for the B1900+Hf specimens were selected to assure that grain size, material structure and integrity match, as closely as possible, those in the PWA test specimens. Goals for this phase of the fabrication effort were:

1. A grain size of ASTM No. 1 to 2 in the gage section when measured using standard procedures.
2. A porosity-free casting.
3. A γ' size of .9 μm in the fully heat treated condition.

TABLE 2.1

CHEMICAL COMPOSITION OF B1900+Hf (HEAT W-0098)

Element	Nominal (%)	Heat W-0098
C	0.11	0.09
Cr	8.0	7.72
Co	10.0	9.91
Mo	6.0	5.97
Al	6.0	6.07
Ta	4.3	4.21
Ti	1.0	0.99
B	0.015	0.016
Zr	0.08	0.04
Fe	0.35*	0.17
W	0.1*	0.04
Cb	0.1*	0.08
Bi	0.5 ppm	0.1
Pb	10.0 ppm	0.1
Hf	1.5	1.19
Ni	Remainder	Remainder

* Maximum

Following casting, all B1900+Hf test bars were fully heat treated according to the following schedule:

Solution: 1079±14°C (1975±25°F) for 4 hours; air cool

Precipitation: 899±14°C (1695±25°F) for 10 hours; air cool.

Figure 2.1 shows the grain size of the as-cast and the fully heat-treated material. The γ' size is approximately .6 μm in the as-cast material and is .9 μm in the fully heat-treated condition, as shown in Figure 2.2.

2.2 Constitutive Model Selection

A literature survey has been conducted to assess the state-of-the-art of time-temperature dependent elastic-viscoplastic constitutive theories which are based on the unified approach. This class of constitutive theories is characterized by the use of kinetic equations and internal variables with appropriate evolution equations for treating all aspects of inelastic deformation including plasticity, creep, and stress relaxation. As reported earlier [1], the review identified more than ten such unified theories which are shown to satisfy the uniqueness and stability criteria imposed by Drucker's postulate and Ponter's inequalities. These theories are compared on the basis of the types of flow law, kinetic equation, evolution equation of the internal variables, and treatment of temperature dependence.

As a result of the literature survey and based upon SwRI recommendations, the models of Bodner and Partom [2] and of Walker [3] have been selected and approved for further study. These two models are both representative of the class of unified models considered in the review process but differ significantly in the choice of particular functional forms for the basic flow law, the kinetic relationship, the parameter used as a measure of hardening

AS - CAST

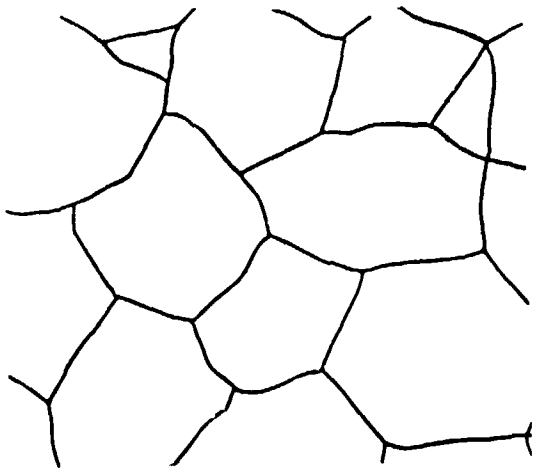

ASTM STANDARD No. 1 100 μm

FULLY HEAT TREATED

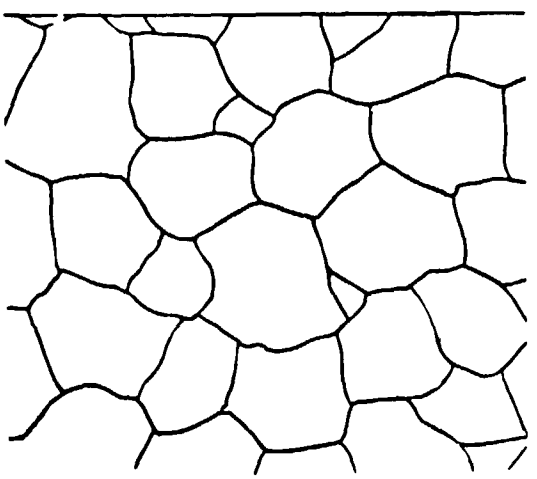

ASTM STANDARD No. 2 100 μm

FIGURE 2.1. GRAIN SIZE OF AS-CAST AND FULLY HEAT TREATED MATERIAL.

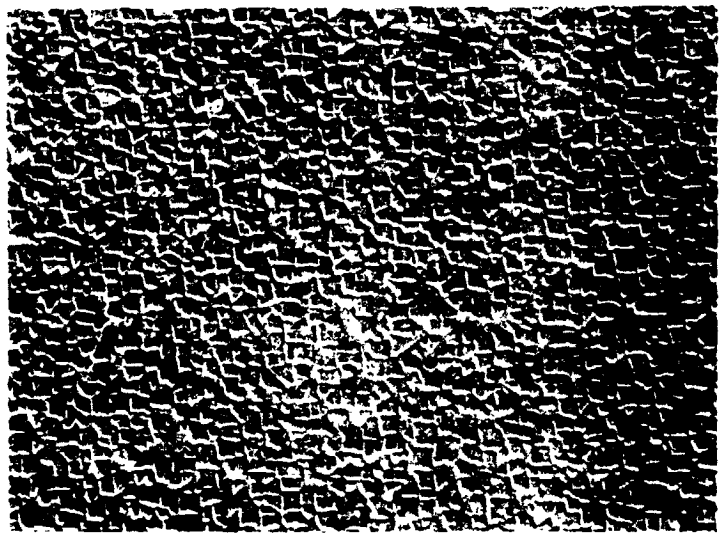

As-Cast $\gamma' = 0.6\ \mu m$ 10μm

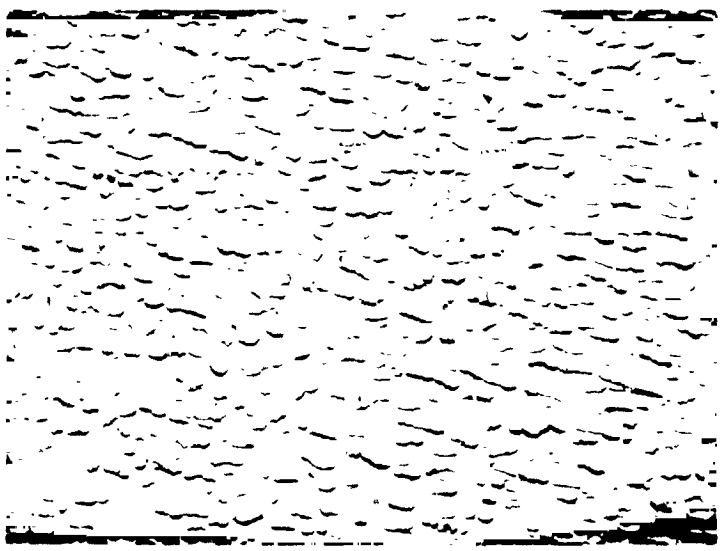

Fully Heat Treated $\gamma' = 0.9\ \mu m$ 10μm

FIGURE 2.2. GAMMA PRIME (γ') SHOWS INCREASE WITH HEAT TREATMENT.

and the evolution equations for the internal variables describing work hardening. Thus, a direct comparison between these two models and the experiments should illustrate well the consequences of a wide range in constitutive modeling approach. It is also significant that both models have already found significant application to analysis of gas turbine materials and to hot section components. Therefore, they are further along in their development and evaluation than most of the other comparable models.

As a result of the literature survey and of direct experience in working with existing models, modifications to the Bodner-Partom and Walker models have been made to account for additional hardening resulting from multiaxial, non-proportional load or strain histories. Modifications have also been made to the kinetic equation and the evolution equations of the internal variables of the Walker model. The updated Bodner-Partom and Walker models will be discussed individually in Section 3.0.

3.0 BRIEF REVIEW OF CONSTITUTIVE MODELS

3.1 Bodner and Partom Model

The elastic-viscoplastic theory of Bodner and Partom, published in 1968 [4], was probably the first "unified" set of constitutive equations without a yield criterion or loading/unloading conditions to be developed. Those equations include certain physical concepts provided by the work on dislocation dynamics during the 1950's and early 1960's. The equations are placed in the context of multi-dimensional continuum mechanics which makes them capable of solving problems by analytical and numerical methods. One of the initial papers, in 1972, considered large deformations [5] and another the same year included isotropic hardening [6]. At the present stage of development, the constitutive theory includes isotropic and directional hardening, thermal recovery of hardening, general temperature dependence of plastic flow, and isotropic and directional damage development [7-9].

A summary of the current Bodner-Partom model without the damage term is shown in Table 3.1. As listed in Table 3.2, there are 13 material constants in the model, most of which are temperature independent, and generally fewer (about 9) are needed in an actual material representation. The basic equation for plastic strain rate as a function of stress and history dependent internal variables is taken to be of exponential form. The initial work [4], before 1970, was based on a power law relation which seems to have been adopted by other investigators. Properties of the exponential function used in the B-P formulation that may be especially useful are its very low value, almost zero, at low stress levels and its limiting value of plastic strain rate. As a consequence, that particular function seems to be suitable to

TABLE 3.1

A SUMMARY OF BODNER-PARTOM'S MODEL

BODNER-PARTOM'S MODEL

1. Flow Law:

$$\dot{\varepsilon}_{ij} = \dot{\varepsilon}_{ij}^{e} + \dot{\varepsilon}_{ij}^{p}$$

$$\dot{\varepsilon}_{ij}^{p} = \lambda S_{ij} \; ; \; \dot{\varepsilon}_{kk}^{p} = 0$$

with $S_{ij} = \sigma_{ij} - \frac{1}{3}\delta_{ij}\sigma_{kk}$

2. Kinetic Equation:

$$D_2^p = D_o^2 \exp\left\{-\left[\frac{Z^2}{3J_2}\right]^n\right\}$$

with $Z = Z^I + Z^D$

$$D_2^p = \frac{1}{2}\dot{\varepsilon}_{ij}^{p}\dot{\varepsilon}_{ij}^{p}$$

$$J_2 = \frac{1}{2}S_{ij}S_{ij}$$

$$\lambda^2 = D_2^p/J_2$$

3. Evolution Equations of Internal Variables:

a. Isotropic Hardening

$$\dot{Z}^I = m_1\left[Z_1 + \alpha Z_3 - Z^I\right]\dot{W}_p - A_1 Z_1\left[\frac{Z^I - Z_2}{Z_1}\right]^{r_1}$$

where $\dot{\alpha} = m_2(\alpha_1 - \alpha)\,\dot{W}_p \sin\theta$

$$\theta = \cos^{-1}(V_{ij}\bar{V}_{ij}) \quad \text{or} \quad \theta = \cos^{-1}(u_{ij}\bar{u}_{ij})$$

$$V_{ij} = \beta_{ij}/(\beta_{kl}\beta_{kl})^{1/2}, \; \bar{V}_{ij} = \dot{\beta}_{ij}/(\dot{\beta}_{kl}\dot{\beta}_{kl})^{1/2}$$

$$u_{ij} = \sigma_{ij}/(\sigma_{kl}\sigma_{kl})^{1/2}, \; \bar{u}_{ij} = \dot{\sigma}_{ij}/(\dot{\sigma}_{kl}\dot{\sigma}_{kl})^{1/2}$$

with $Z^I(o) = Z_o$; $\dot{W}_p = \sigma_{ij}\dot{\varepsilon}_{ij}^{p}$; $W_p(o) = 0$; $\alpha(0) = 0$

b. Directional Hardening

$$\dot{\beta}_{ij} = m_2(Z_3 u_{ij} - \beta_{ij})\,\dot{W}_p - A_2 Z_1\left[\frac{(\beta_{kl}\beta_{kl})^{1/2}}{Z_1}\right]^{r_2} V_{ij}$$

with $Z^D = \beta_{ij}u_{ij}$; $Z^D(o) = 0$, $\beta_{ij}(o) = 0$

Material Constants: D_o, Z_o, Z_1, Z_2, Z_3, m_1, m_2, α_1

A_1, A_2, r_1, r_2, n, and elastic constants

In most cases can set: $r_1 = r_2$, $A_1 = A_2$, $Z_o = Z_2$

TABLE 3.2

MATERIAL CONSTANTS IN BODNER-PARTOM CONSTITUTIVE MODEL

Constants	Descriptions
D_o	Limiting shear strain rate, sec^{-1}
Z_o	Initial value of the isotropic hardening variable, MPa
Z_1	Limiting (maximum) value of Z^I, MPa
Z_2	Fully recovered (minimum) value of Z^I, MPa
Z_3	Limiting (maximum) value of Z^D, MPa
m_1	Hardening rate coefficient of Z^I, MPa^{-1}
m_2	Hardening rate coefficient of Z^D, MPa^{-1}
n	Kinetic parameter
A_1	Recovery coefficient for Z^I, sec^{-1}
A_2	Recovery coefficient for Z^D, sec^{-1}
r_1	Recovery exponent for Z^I
r_2	Recovery exponent for Z^D
α_1	Limiting coefficient for non-proportional hardening effect

represent material behavior over a wide range of strain rates including the very high rates, i.e., about 10^5 sec^{-1}.

The treatment of directional hardening by Bodner and his associates has been based on the general anisotropic form of the flow law rather than on the "back stress" concept. An incremental isotropic form of the flow law has been proposed as an approximation which would simplify the numerical computations. In the incremental isotropic equation, the scalar coefficient is a function of both the isotropic and directional hardening variables which depend on the loading history. The isotropic hardening variable controls the cyclic hardening or softening characteristic.

The scalar measure for hardening is taken to be the plastic work rate. However, the overall theory is not dependent on this point and other measures, e.g., plastic strain rate or a function of the plastic strain rate history, are admissible within the context of the theory. For directional hardening, the stress is used as the directional index of hardening to avoid cross softening effects. The plastic strain rate had been used previously for that purpose and most other theories still rely on that variable.

Multiaxial, non-proportional hardening is taken into account by introducing a load history dependent variable, α, into the evolution equation for isotropic hardening. As can be seen from the expression in Table 3.1, the parameter α increases with non-proportional loading history from zero to a limiting value of α_1. The saturation value of Z^I under such loading is then $(Z_1 + \alpha_1 Z_3)$. Non-proportionality of loading path is measured in terms of an angular parameter θ defined by either of the following expressions:

$$\theta = \cos^{-1} (V_{ij} \overline{V}_{ij}) \qquad (3.1)$$

or $$\theta = \cos^{-1}(U_{ij}\,\bar{U}_{ij}) \qquad (3.2)$$

where U_{ij}, $\bar{U}_{ij}$, V_{ij} and $\bar{V}_{ij}$, as given in Table 3.1, are the directional cosines of the current values of σ_{ij}, β_{ij}, $\dot{\sigma}_{ij}$, and $\dot{\beta}_{ij}$, respectively.

3.2 Walker Model

Two internal variables are used in the Walker theory. The equilibrium stress Ω_{ij} represents nonlinear kinematic hardening and accounts for the Bauschinger effect, while the drag stress K represents isotropic hardening and accounts for cyclic hardening of the material.

The growth law for the equilibrium stress, Ω_{ij}, is the sum of two components, Ω_{ijo} and Ω_{ij1}. Ω_{ijo} is the initial equilibrium stress offset which accounts for the difference in the tensile and compressive yield strength. The growth law for the second component, Ω_{ij1}, contains hardening, dynamic recovery and thermal recovery terms. At high strain rates thermal recovery is small in comparison to the dynamic recovery and the equilibrium stress saturates to a limiting value at large plastic strain that is independent of the strain rate. The drag stress, K, is assumed to be a function of only the accumulated effective plastic strain, R.* The isotropic hardness is initially $K_1 - K_2$ and saturates at a value of K_1 with increasing plastic strain. Cyclic hardening or softening can be modelled using this feature. The kinetic relationship that relates the nonlinear strain rate to the excess stress, $S_{ij}-\Omega_{ij}$, was assumed to be a power law expression. This form of the model [3] has been found to capture most of the behaviors noted in testing of the solid solution strengthened alloys such as Hastelloy-X.

---

* $$R = \int \sqrt{\frac{2}{3}\,\dot{\varepsilon}^{p}_{ij}\,\dot{\varepsilon}^{p}_{ij}}\,dt$$

The Walker model, as described in [3] and summarized in [1], has been significantly modified for describing the constitutive behavior of B1900+Hf. Modifications to the unified constitutive model to capture some of the features of the B1900+Hf deformation behavior are indicated:

(1) **Form of the Kinetic Relationship** - At low to intermediate temperatures the limit stress in a monotonic tensile test does not vary with strain rate to a power but exponentially. A more appropriate equation relating the inelastic strain rate and the effective stress is the exponential function:

$$\dot{\varepsilon}^{p} = \frac{1}{\beta} \exp\left\{ \frac{\sqrt{\frac{2}{3}\left(\frac{3}{2} S_{ij}-\Omega_{ij}\right)\left(\frac{3}{2} S_{ij}-\Omega_{ij}\right)}}{K} - 1 \right\} \qquad (3.3)$$

(2) **Form of the Drag Stress Relationship, K** - Cyclic hardening or softening observed during the uniaxial testing is simulated by assuming that the isotropic hardening variable, K, varies with accumulated inelastic strain, R. Addition of a similar term, $K_3 \times \exp(-n_8 L)$, can approximate the cyclic hardening observed under nonproportional loading cycles. $\dot{L}$, a measure of the nonproportionality of the strain path, is defined as the difference between the effective strain rate and the rate of effective strain, as shown in Eq. 3 of Table 3.3. n_8 and K_3 are shape and level parameters, respectively, and can be determined from a single nonproportional multiaxial loading test at each test temperature.

TABLE 3.3

MODIFIED WALKER THEORY (DIFFERENTIAL FORM)

$$\dot{\epsilon}_{ij}^{p} = \frac{\left(\frac{3}{2} S_{ij} - \Omega_{ij}\right)}{\sqrt{\frac{2}{3}\left(\frac{3}{2} S_{ij} - \Omega_{ij}\right)\left(\frac{3}{2} S_{ij} - \Omega_{ij}\right)}} \left\{ \exp\left(\frac{\sqrt{\frac{2}{3}\left(\frac{3}{2} S_{ij} - \Omega_{ij}\right)\left(\frac{3}{2} S_{ij} - \Omega_{ij}\right)}}{K}\right) - 1 \right\} / \beta \qquad (1)$$

$$K = K_1 - K_2 e^{-\eta_7 R} - K_3 e^{-\eta_8 L} \qquad (2)$$

$$\dot{L} = \left| \sqrt{\frac{2}{3} \dot{\epsilon}_{ij}^{p} \dot{\epsilon}_{ij}^{p}} - \left| \sqrt{\frac{2}{3} \epsilon_{ij}^{p} \epsilon_{ij}^{p}} \right| \right| \qquad (3)$$

$$\dot{R} = \sqrt{\frac{2}{3} \dot{\epsilon}_{ij}^{p} \dot{\epsilon}_{ij}^{p}} \qquad (4)$$

$$\Omega_{ij} = \Omega_{ij0} + \Omega_{ij1} + \Omega_{ij2} \qquad (5)$$

$$\dot{\Omega}_{ij1} = \eta_2 \dot{\epsilon}_{ij}^{p} - \Omega_{ij1}\left[\left(\eta_3 + \eta_4 e^{-\eta_5 \left|\log \frac{\dot{R}}{\dot{R}_0}\right|}\right) \dot{R} + \eta_6 + \frac{1}{\eta_2} \frac{\partial \eta_2}{\partial \theta} \dot{\theta} - \frac{1}{\eta_3} \frac{\partial \eta_3}{\partial \theta} \dot{\theta}\right] + \left(\frac{\eta_2}{\eta_3} - \Omega_{ij1}\right) \frac{\partial \eta_3}{\partial \theta} \epsilon_{ij}^{p} \dot{\theta} \qquad (6)$$

$$\dot{\Omega}_{ij2} = \eta_{11} \dot{\epsilon}_{ij}^{p} - \Omega_{ij2}\left(\eta_9 \dot{R} + \eta_{10} + \frac{1}{\eta_{11}} \frac{\partial \eta_{11}}{\partial \theta} \dot{\theta} - \frac{1}{\eta_9} \frac{\partial \eta_9}{\partial \theta} \dot{\theta}\right) + \left(\frac{\eta_{11}}{\eta_9} - \Omega_{ij2}\right) \frac{\partial \eta_9}{\partial \theta} \epsilon_{ij}^{p} \dot{\theta} \qquad (7)$$

$$\mathring{\Omega}_{ij} = 3\dot{\mathring{\Omega}}\left[\frac{\dot{C}_{ik} C_{kj}}{C_{pq} C_{pq}} + \frac{C_{ik} \dot{C}_{kj}}{C_{pq} C_{pq}} - \left(\frac{2 C_{ik} C_{kj}}{C_{pq} C_{pq}}\right)\left(\frac{C_{rs} \dot{C}_{rs}}{C_{uv} C_{uv}}\right)\right] + \left[3 \frac{C_{ik} C_{kj}}{C_{pq} C_{pq}} - \delta_{ij}\right] \frac{\partial \dot{\Omega}}{\partial \theta} \qquad (8)$$

$$S_{ij} = \sigma_{ij} - \frac{1}{3} \delta_{ij} \sigma_{kk} \qquad (9)$$

Material Constants: λ, μ, $\mathring{\Omega}$, β, η_2, η_3, η_4, η_5, η_6, η_7, η_8, η_9, η_{10}, η_{11}, K_1, K_2, K_3, dependent on temperature, θ

(3) **Form of the Equilibrium Stress Relationship** - The equilibrium stress is now assumed to be the sum of three terms, $\Omega_{ij1} + \Omega_{ijo}$, and an additional term, Ω_{ij2}, introduced to predict linear hardening at high strain rates. The expression for Ω_{ij2} is

$$\dot{\Omega}_{ij2} = \eta_{11}\dot{\epsilon}^{p}_{ij} - \Omega_{ij2}\,(\eta_9\dot{R} + \eta_{10}) \tag{3.4}$$

For plastic strain rates sufficient to saturate $\Omega_{ijo} + \Omega_{ij1}$ but insufficient to saturate Ω_{ij2}, $\dot{\Omega}_{ij2}$ varies linearly with the plastic strain rate. Assuming a constant strain rate tensile test, the flow stress will therefore increase directly with Ω_{ij2} in a linear fashion for small strains. With increasing strain and for high strain rates, Ω_{ij2} will eventually saturate to a value η_{11}/η_9. With increasing strain and at low strain rates, the rate of strain hardening in Ω_{ij2} can be minimized by a judicious selection of η_{10}, representing thermal recovery. A modification to the evolutionary expression for Ω_{ij1} is also required to capture the inverse strain rate sensitivity observed in the B1900+Hf monotonic tensile data at 760°C. The dynamic recovery term is now assumed to be a function of the strain rate, vis:

$$\left(\eta_3 + \eta_4 \exp\left(-\eta_5 \left|\log\left(\frac{\dot{R}}{\dot{R}_o}\right)\right|\right)\right)\dot{R} \tag{3.5}$$

By judicious selection of the constants n_4 and n_5 the flow strength can be made to decrease either side of the strain rate R_0.

(4) **Thermal Effects** - The constants in Walker's unified theory are generally functions of temperatures, T. If a material is subjected to a strain and temperature change simultaneously, the incremental change in a state variable, SV, will be:

$$\frac{dSV}{dt} = \frac{\partial SV}{\partial t} + \frac{\partial SV}{\partial T}\frac{dT}{dt} \qquad (3.6)$$

The Walker theory has been modified to include the rate of change of temperature terms.

Table 3.3 presents the modified Walker theory employed by PWA to correlate the B1900+Hf data. The modified Walker model contains 15 material constants which are all temperature dependent. Generally, fewer will be needed (about 10 for B1900+Hf) in an actual material representation.

4.0 UNIAXIAL EVALUATION OF CONSTITUTIVE MODELS

4.1 Experimental Procedures

Five different mechanical testing modes were used for developing the uniaxial constitutive data of B1900+Hf in the present program. They included tensile, creep, isothermal cyclic, stress relaxation, and thermomechanical fatigue (TMF) tests. A large quantity of constitutive information was also generated as part of the data acquisition efforts in the HOST Isotropic Fatigue Contract (NAS3-23288). Results of these two programs were integrated to form a large data base for constitutive model evaluation.

All the isothermal, uniaxial tests in the present program were conducted in a closed-loop, servo-hydraulic test machine at SwRI. Figure 4.1 shows the configuration of the test specimen and the experimental set-up. Strain was measured using an externally mounted extensometer with ceramic reach-rods attached to the specimen. Induction heating was used for providing the elevated temperature; temperature variations over the specimen gage section are within ASTM specifications for short-term tests. The specimen designs utilized in various constitutive tests are schematically illustrated in Figure 4.2. Figure 4.3 shows photographs of: (A) an isothermal constitutive specimen, (B) a thermomechanical constitutive specimen, and (C) a biaxial specimen.

Tensile tests were performed at various strain rates ranging from $4x10^{-2}$ to $4x10^{-7}$ sec^{-1} at 25, 649, 760, 871, 982, and 1093°C. A summary of the tensile test matrix can be found in last year annual report [1]. Creep tests were conducted at the latter five temperatures.

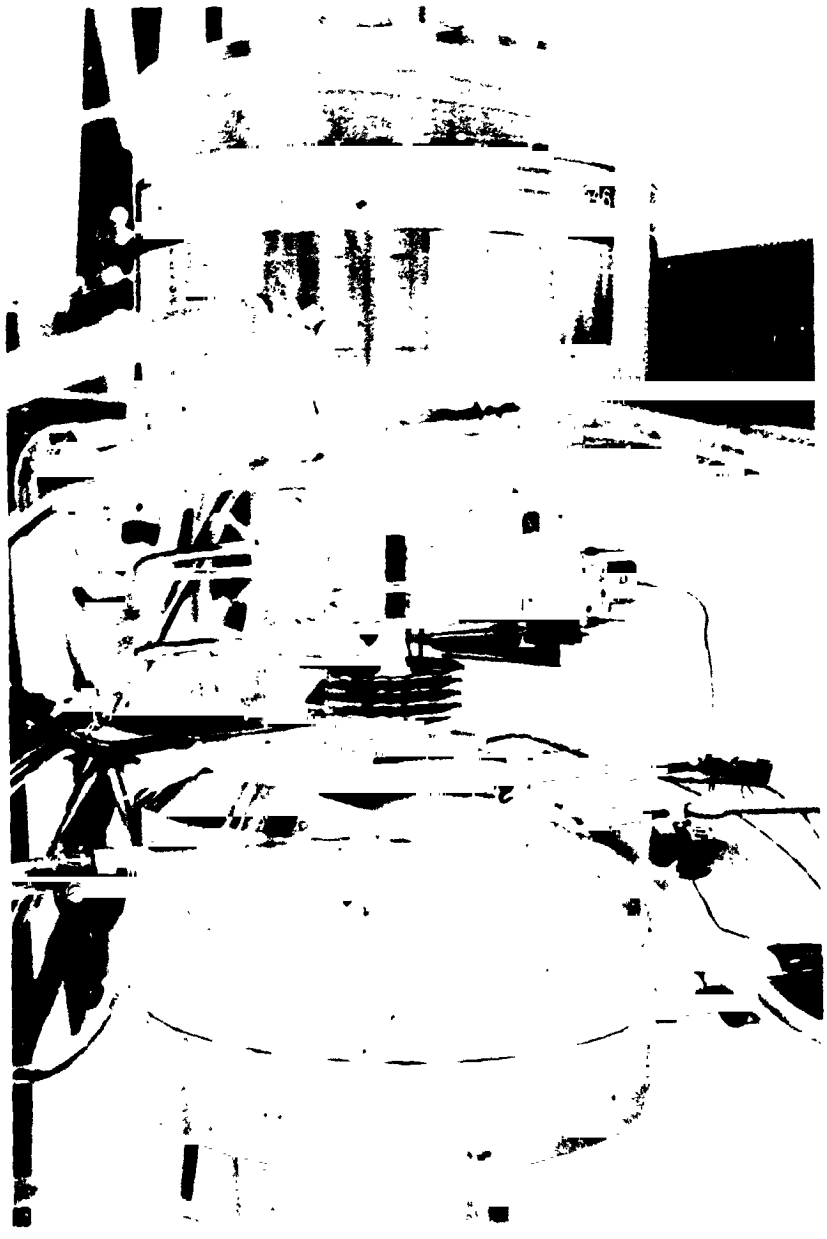

FIGURE 4.1. TENSILE SPECIMEN UNDER TEST AT 871°C.

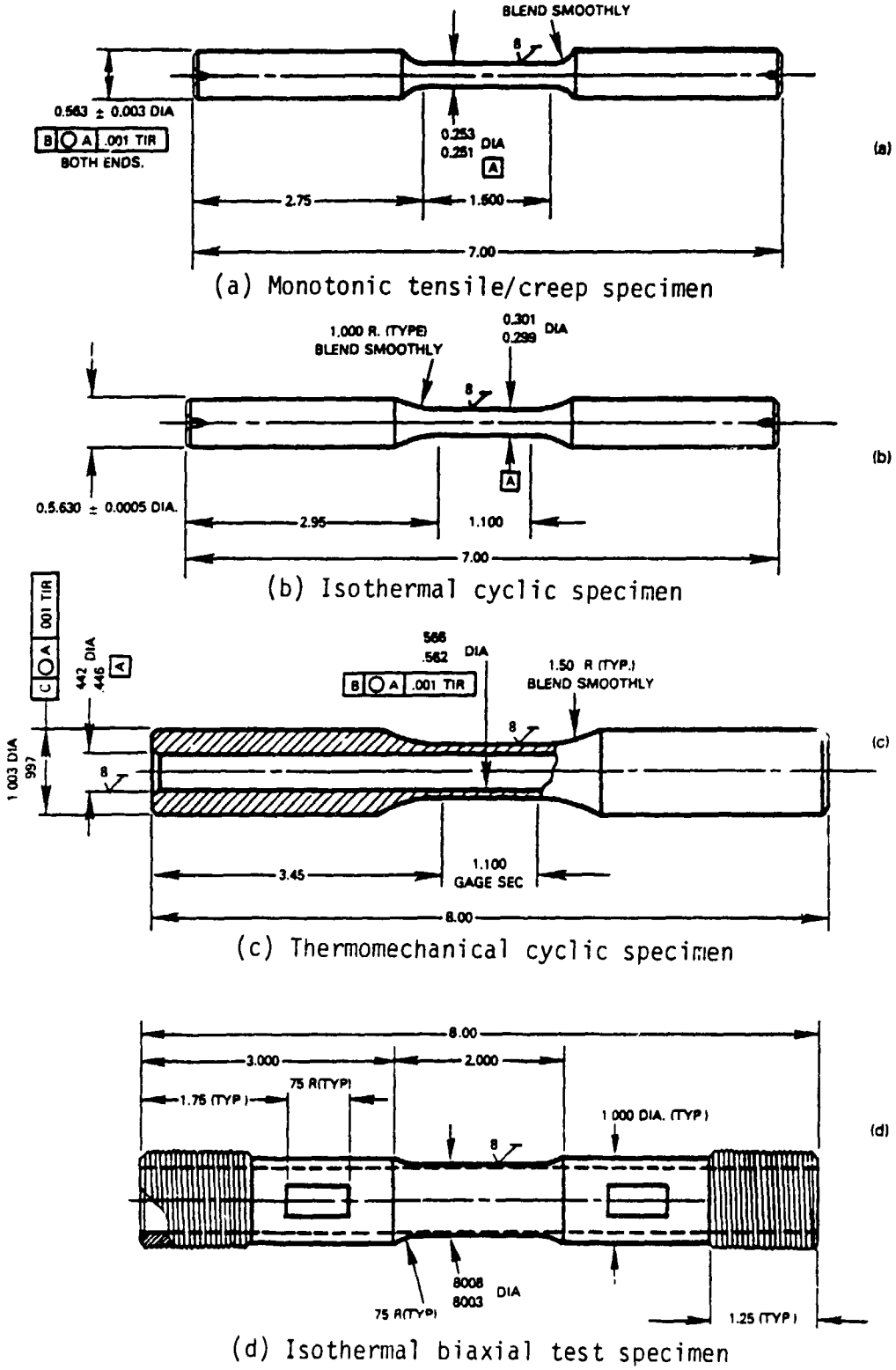

FIGURE 4.2. SPECIMEN DESIGNS UTILIZED IN VARIOUS CONSTITUTIVE TESTS. (All units are in inches.)

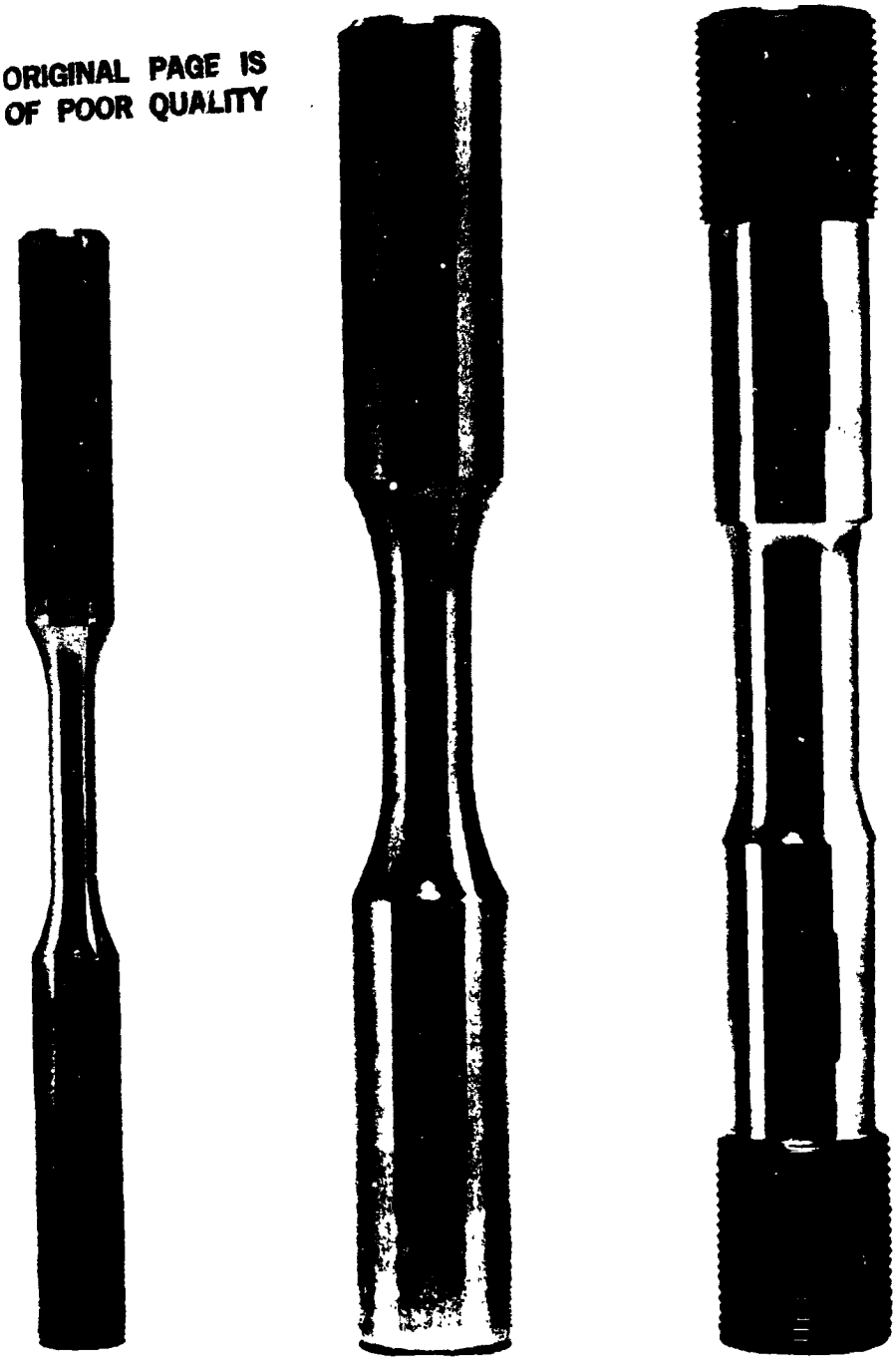

FIGURE 4.3. PHOTOGRAPHS OF (A) ISOTHERMAL CONSTITUTIVE SPECIMEN, (B) THERMOMECHANICAL CONSTITUTIVE SPECIMEN, AND (C) BIAXIAL SPECIMEN.

TABLE 4.1

ISOTHERMAL CYCLIC CONSTITUTIVE TESTS

Temp(°C)	R	$\dot{\varepsilon}(sec^{-1})$	Strain Range .25%	.4%	.6%	.8%
o Effect of Temperature and Strain Rate						
427	0	$4x10^{-3}$	X	X	X	X
538	0	$4x10^{-4}$	X	X	X	X
649	0	$4x10^{-4}$	X	X	X	X
760	-1	$4x10^{-3}$	X	X	X	X
871	-1	$4x10^{-4}$	X	X	X	X
982	-1	$4x10^{-4}$	X	X	X	X
1093	-1	$4x10^{-5}$	X	X	X	X
o Effect of Mean Strain						
538	-1	$4x10^{-4}$	X	X	X	X
760	0	$4x10^{-3}$	X	X	X	X
760	$-\infty$	$4x10^{-3}$	X	X	X	X
871	$-\infty$	$4x10^{-4}$	X	X	X	X
1093	$-\infty$	$4x10^{-5}$	X	X	X	X
o Strain Hold to Probe for Equilibrium Stress						
760	-1	$4x10^{-4}$	X	X	X	X
871	-1	$4x10^{-4}$	X	X	X	X
1093	-1	$4x10^{-4}$	X	X	X	X

Temp(°C)	R	$\dot{\sigma}$ (MPa/sec)	$\pm\Delta\sigma_1$	$\pm\Delta\sigma_2$	$\pm\Delta\sigma_3$	$\pm\Delta\sigma_4$
o Effect of Stress Hold			(MPa)			
760	-1/T	59.3	± 350	± 550	± 650	± 750
871	-1/TC	55.2	± 310	± 400	± 500	± 600
982	-1/C	51.0	± 241	± 345	--	--

T - Stress hold at peak tension for 120 sec.
C - Stress hold at peak compression for 120 sec.

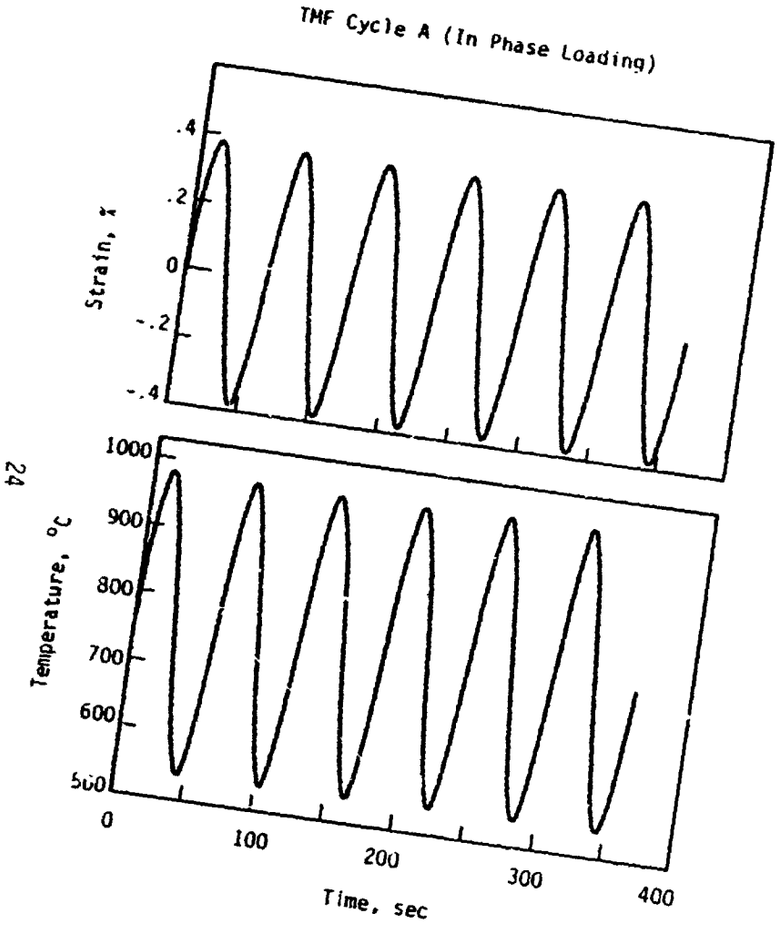

(a)

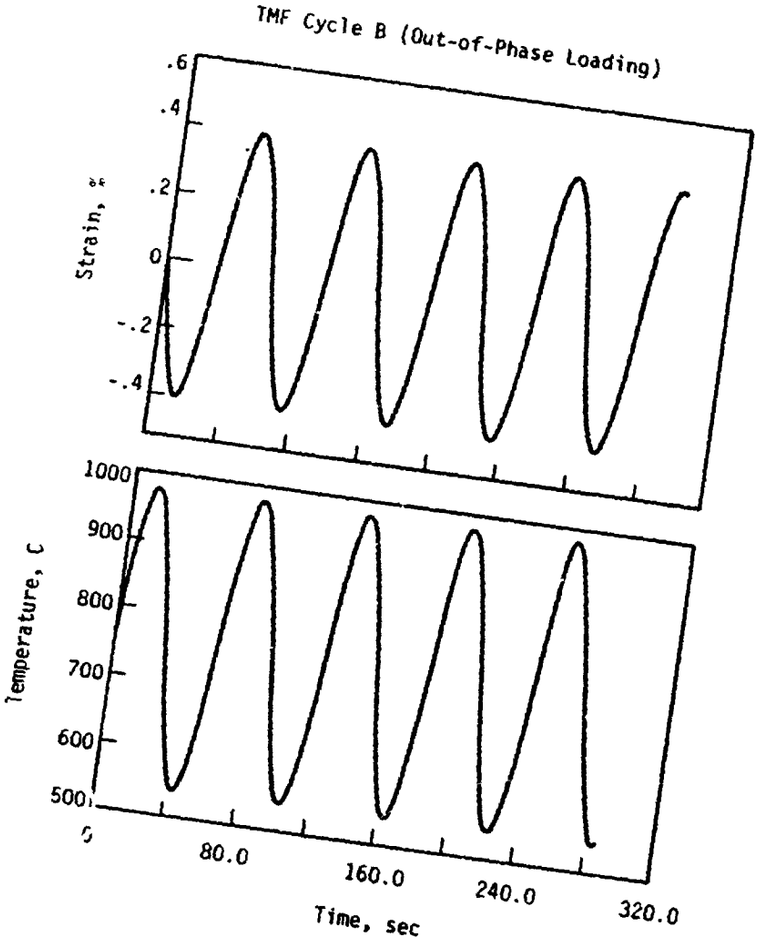

(b)

FIGURE 4.4. TMF LOADING HISTORIES: (A) IN-PHASE LOADING, (B) OUT-OF-PHASE LOADING.

Isothermal cyclic tests were conducted either with or without dwell. As indicated in Table 4.1, the cyclic constitutive tests were performed at four different strain range levels (±.25%, ±.4%, ±.6% and ±.8%). Testing was performed at R ratios ($R = \varepsilon_{min}/\varepsilon_{max}$) of 0, -1, and $-\infty$ at temperatures ranging from 427 to 1093°C and at strain rates of $\pm 4 \times 10^{-3}$ to $\pm 4 \times 10^{-5}$ sec^{-1}. Cyclic tests with dwell were conducted at a loading rate of approximately 58.6 MPa/s. The load was held constant for two minutes when the prescribed maximum or minimum stress was reached. For determining equilibrium stress values, stress relaxation at various strain levels of the first cycle hysteresis loop and of the saturated one was measured. The time of strain hold was 30 seconds to 2 minutes. The stress relaxation test conditions are also shown in Table 4.1.

The thermomechanical fatigue (TMF) loading histories were run with a sinusoidally varying mechanical strain and temperature with a cycle period of sixty seconds (Figure 4.4). The strain for three of the tests varied from a nominal -0.4 percent to +0.4 percent, and the temperature varied sinusoidally from 538° to 982°C. For the first TMF loading cycle, the temperature and strain varied in phase, i.e., the maximum temperature occurred at the same time as the maximum strain (Figure 4.4a). For the second loading case, the temperature and strain loads were applied 180° out of phase, and in this case the maximum temperature coincided with the minimum strain (Figure 4.4b). The third TMF cycle was a repeat of the second case but with the addition of a sixty second constant strain hold at -0.4 percent strain.

4.2 Evaluation of Model Constants

4.2.1 Bodner-Partom Model

A systematic procedure for determining the material constants in the Bodner-Partom model is outlined in Figure 4.5. The procedure is developed by

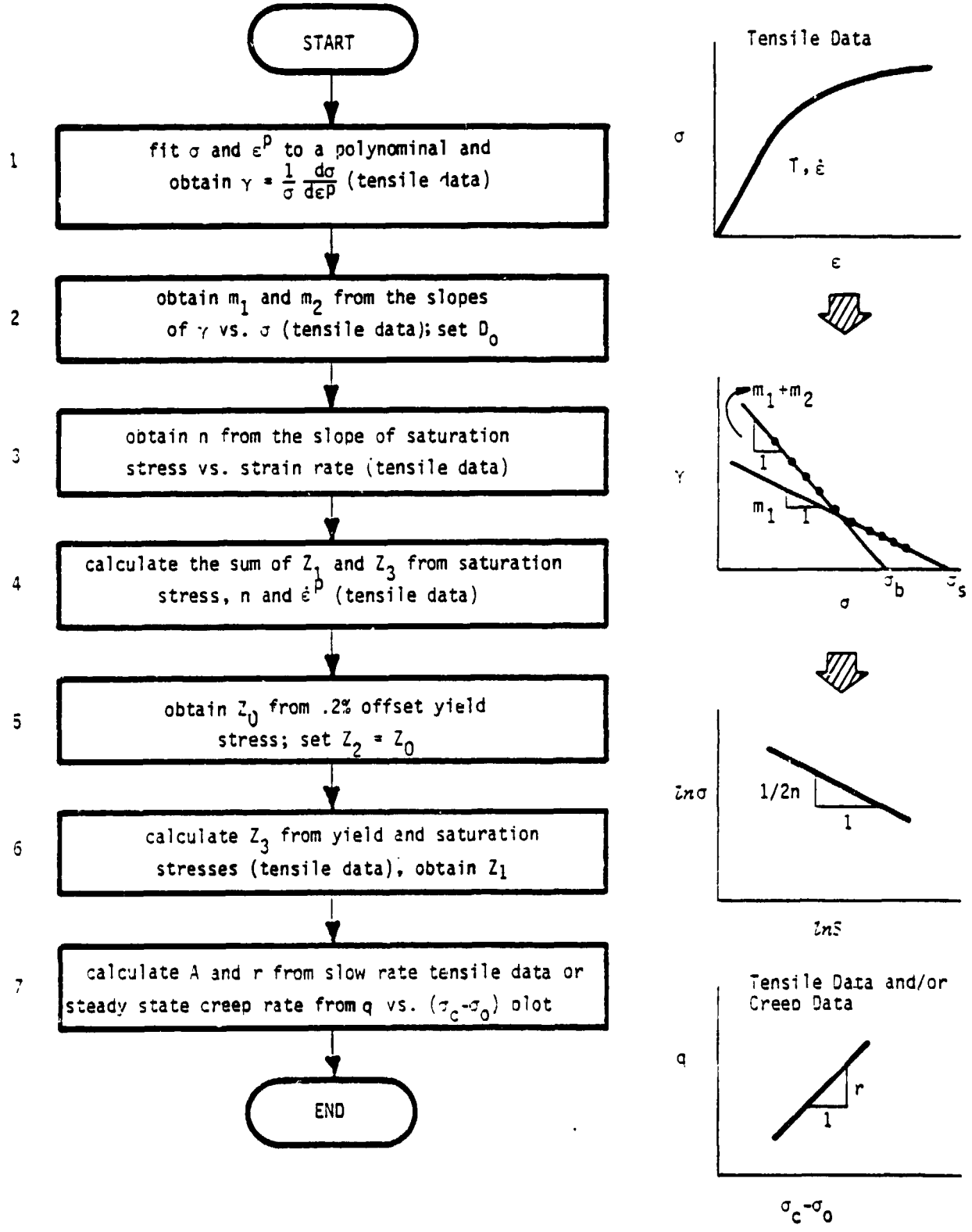

FIGURE 4.5. A FLOW CHART SHOWING A SYSTEMATIC PROCEDURE FOR EVALUATING THE MATERIAL CONSTANTS IN THE BODNER-PARTOM THEORY.

recasting the Bodner-Partom equations into convenient forms such that the material constants can be evaluated from the experimental data by separate consideration of basic physical effects such as hardening, strain rate dependence, and thermal recovery. The theoretical basis of the method is outlined here. Excluding the elastic constants, a total of 13 material constants must be evaluated from pertinent experimental data. In most cases, including non-proportional loading paths, only nine model constants need to be determined. Most of the constants, tabulated and briefly discussed in Table 3.2, can be evaluated from monotonic tensile data. Creep data would also be required if slow strain rate tensile data were not available.

As shown in Figure 4.5, step (1) in determining the material constants in the Bodner-Partom model is to develop a set of work hardening rate data from the experimental stress-strain results. A simple computer program has been developed for this purpose. Using the monotonic tensile stress-strain data and the elastic modulus as inputs, the computer program calculates the plastic strain component by subtracting the elastic component from the total strain. The stress is then expressed as a polynominal function of the plastic strain.

$$\sigma = a_0 + a_1\varepsilon^p + a_2(\varepsilon^p)^2 + \ldots\ldots + a_m(\varepsilon^p)^m \qquad (4.1)$$

The coefficients a_0, a_1, a_2, ... a_m are computed using the least-square method. The work hardening rate, $\gamma = d\sigma/dW_p = (1/\sigma)(d\sigma/d\varepsilon^p)$, can then be calculated as:

$$\gamma = \frac{1}{\sigma}\left[a_1 + 2a_2\varepsilon^p + \ldots + ma_m(\varepsilon^p)^{m-1}\right] \qquad (4.2)$$

where σ is obtained from Equation 4.1. The number of terms required in Equation 4.1 is usually obtained by trial and error. For B1900+Hf, the cubic polynominal (m = 3) is generally sufficient, but a fourth-order (m = 4) polynominal has also been used occasionally.

Step (2) is to evaluate the constants m_1 and m_2 from the plot of γ versus σ (Figure 4.6). The Bodner-Partom model can be written for uniaxial stress case as:

$$\sigma = L_1 Z (W_p) \tag{4.3}$$

with $$L_1 = [2 \ln (2D_o/\sqrt{3}\ \dot{\varepsilon}^p)]^{-1/2n}$$

$$Z = Z^I + Z^D$$

where Z^I and Z^D are the isotropic and the directional hardening variables.

In the absence of thermal recovery and on the physical basis that Z^D saturates much more rapidly than Z^I for most materials, i.e., $m_2 > m_1$, the following approximations to Equation (4.3) can be made in the region of small plastic strains,

$$Z^I = (\sigma/L_1) - Z^D \approx (\sigma/L_1) - Z_3$$

$$Z^D = (\sigma/L_1) - Z^I \approx (\sigma/L_1) - Z_o$$

where the additional terms are defined in Table 3.2. These approximations are then substituted in the general expression for $\gamma = d\sigma/dW_p$ obtained from Equation (4.3) and the evolution equations for Z^I and Z^D, namely

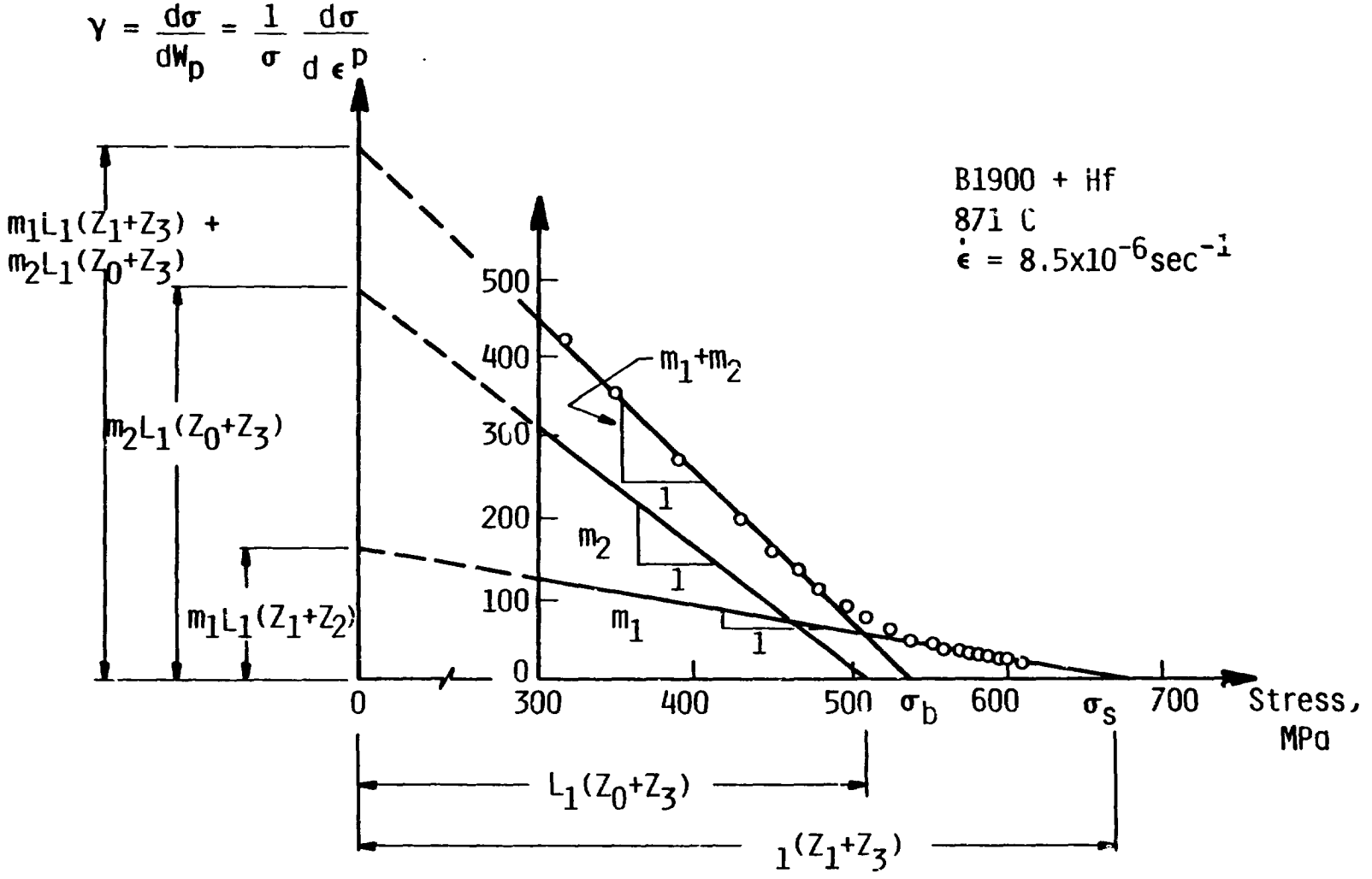

FIGURE 4.6. A SCHEMATIC SHOWING THE ISOTROPIC AND DIRECTIONAL HARDENING COMPONENTS IN A γ-σ PLOT.

$$\gamma = L_1 \left[m_1(Z_1 - Z^I) + m_2(Z_3 - Z^D) \right] \qquad (4.4)$$

Upon reduction, the expression for γ becomes

$$\gamma = L_1[m_1(Z_1+Z_3) + m_2(Z_o+Z_3)] - (m_1+m_2)\sigma \qquad (4.5)$$

This indicates that a plot of γ against σ should be linear with slope (m_1 + m_2) in the range of small plastic strains.

At the larger strains, Z^D fully saturates to the limiting value Z_3 so that setting $Z^D = Z_3$ and again using the above approximation for Z^I gives

$$\gamma = L_1 m_1(Z_1+Z_3) - m_1\sigma \qquad (4.6)$$

which is a linear relation with slope m_1. These relations indicate that the γ-σ function should be essentially linear at both the low and high plastic strain regions.

Plots of γ-σ in Figure 4.7 indicates the bilinear behavior. For temperatures at and below 871°C, the effects of the strain rate and temperature are to shift the γ-σ curves along the horizontal axis without causing any significant changes in the slopes of the curves. This hardening behavior can be rationalized on the basis that both the isotropic and the directional hardening components are present and they are not significantly affected by static thermal recovery at these temperatures. On this basis, the constants m_1 and

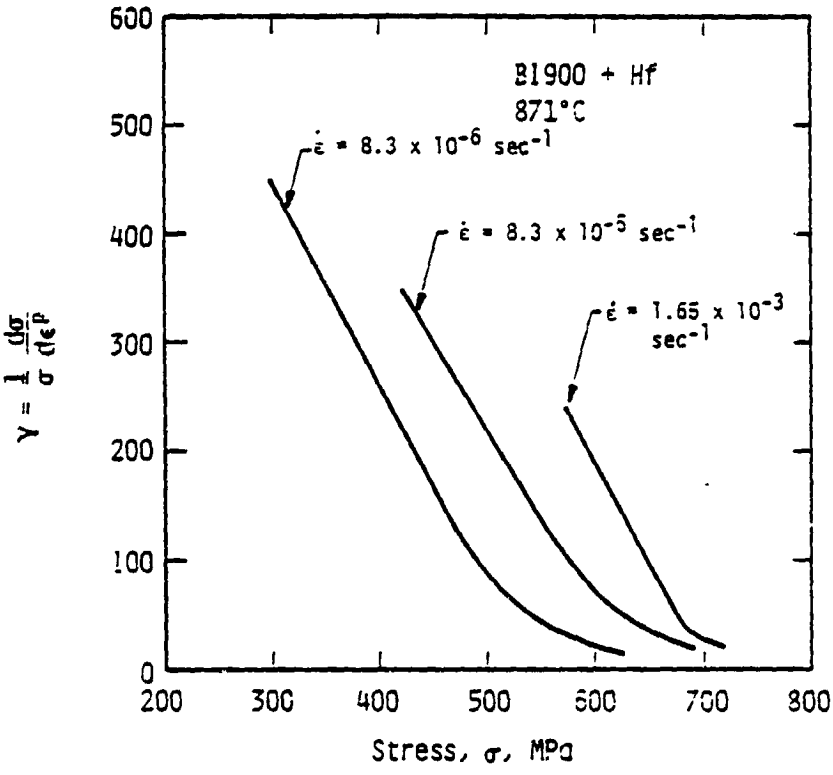

(a)

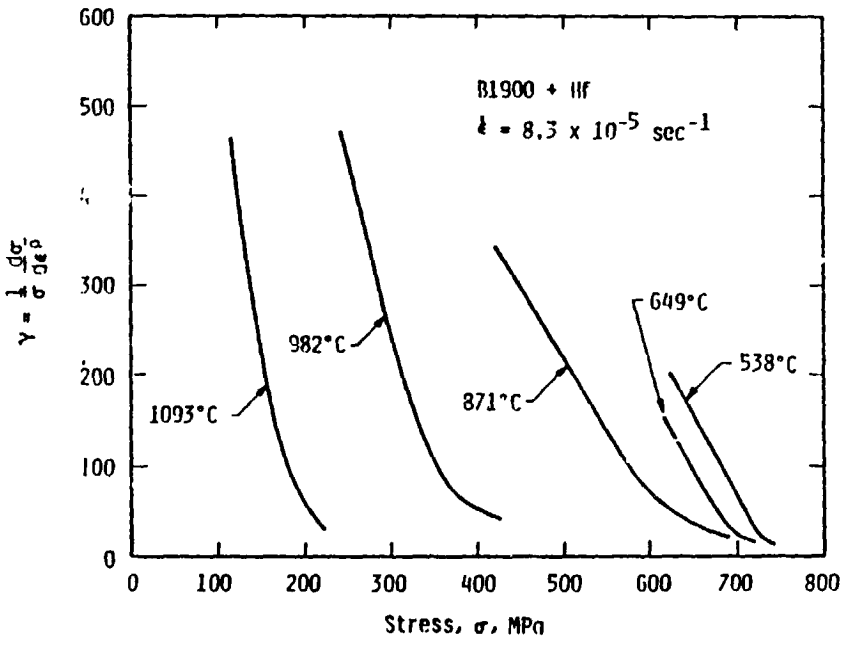

(b)

FIGURE 4.7. THE γ-σ CURVES OF B1900+Hf (A) AT 871°C SHOWING SHIFTS TO HIGHER STRESSES AS THE STRAIN RATES ARE INCREASED, AND (B) AT A GIVEN STRAIN RATE SHOWING TEMPERATURE SHIFTS ALONG THE σ-AXIS AND SLOPE CHANGES FOR TEMPERATURES ABOVE 982°C.

m_2 can be evaluated from a γ-σ plot. As shown in Figure 4.6, the initial linear slope of the γ-σ curve for B1900+Hf at 871°C is given by the sum of m_1 and m_2, while at high stress values the slope is then given by m_1. The extrapolated intercept at the σ axis for $\gamma = 0$ is σ_s (the saturation stress) which is given by:

$$\sigma_s = L_1(Z_1+Z_3) \tag{4.7}$$

The measured values of m_1, $m_1 + m_2$, σ_s, and the calculated values of m_2 for a number of specimens tested at various temperatures are summarized in Table 4.2.

Step (3) is to evaluate the constants n and D_o in the kinetic equation. D_o is the limiting inelastic strain rate in shear and is usually taken to be 1×10^4 sec^{-1} unless high strain rates are being considered. The constant n is evaluated from the stress dependence on strain rate at a constant value of Z. Equations 4.3 and 4.4 are rearranged to give the following expressions:

$$ln\sigma = -\frac{1}{2n} ln\ S + ln\ Z \tag{4.8}$$

$$\text{and } \frac{1}{n} = -\frac{2d ln\sigma}{d ln S}; \quad Z = \text{constant}; \quad W_p = \text{constant} \tag{4.9}$$

$$\text{where } S = 2\ ln\ (2D_o/\sqrt{3}\ \dot{\varepsilon}^p) = L_1^{-2n} \tag{4.10}$$

TABLE 4.2

EVALUATIONS OF BODNER-PARTOM MATERIAL CONSTANTS FOR B1900+Hf

Specimen	Temp. °C	$\dot{\varepsilon}$, sec^{-1}	m_1	MPa^{-1} m_1+m_2	m_2	σ_s MPa	n	Z_1+Z_2 MPa	σ_o MPa	σ_b MPa	Z_3 MPa	Z_o MPa
39A	871	$8.5x10^{-6}$	.321	1.852	1.531	670	1.03	4078	300	540	1278	1802
39B	871	$8.5x10^{-5}$	.272	1.545	1.273	740	1.03	4218	400	640	1240	2280
24A	871	$1.65x10^{-3}$	.273	1.830	1.557	-	1.03	4119	530	701	830	2641
19A	649	$8.5x10^{-5}$	.233	1.663	1.430	790	1.055	--				
2A	538	$8.5x10^{-5}$	.266	1.822	1.556	797	1.055	4423				
Average			.27		1.52			4200			1120	2300

Thus, n can be evaluated either from the slope of a plot of $\ln\sigma$ versus $\ln\dot{S}$ at a constant value of Z (W_p) or from Equation (4.9). When static thermal recovery is not important, the stresses for evaluating the parameter n could be (1) the saturation stress σ_s at different strain rates where σ_s corresponds to the limiting value of Z or ($Z_1 + Z_3$) which can be obtained by extrapolating the γ-σ curve to the stress at which γ is equal to zero (Figure 4.6); (2) the peak stresses of saturated cyclic hysteresis loops at different strain rates and at a constant value of large strain amplitude for which both Z^I and Z^D saturate; and (3) the flow stresses at different strain rates and at constant values of plastic work. The n values for B1900+Hf at 871°C and 539°C have been calculated based on method (1) using Equation (4.9). The results are shown in Table 4.2.

It is important to note that stress values under steady state conditions during creep or tensile straining do not always correspond to the same value of Z. In addition, plastic work does not have a one-to-one relationship with Z at elevated temperatures for which static thermal recovery is significant. Consequently, stresses under steady state conditions involving thermal recovery should not be used in conjunction with Equations 4.8 and 4.9 for evaluating n. Once the n value is evaluated for a lower temperature at which static thermal recovery is insignificant, the constants Z_1 and Z_3 can be computed (see Step 4). Since both Z_1 and Z_3 are considered to be temperature-independent, the n value at high temperatures can be obtained by fitting a stress-strain curve at a strain rate above 10^{-3} sec^{-1} or by using Equation (4.7) if σ_s is known. The n values for B1900+Hf at 982 and 1093°C have been obtained using the former procedure.

Step (4) is to calculate the sum of Z_1 and Z_3. Using the saturation stresses obtained in Step (2) and the L_1 value obtained in Step (3), the sum of Z_1 and Z_3 is calculated using Equations (4.7). The results are shown in Table 4.2.

Step (5) is to evaluate the relative contributions of Z_1 and Z_3, the limiting values of the isotropic hardening, and the directional hardening variables, respectively, in the total hardening. From Equation 4.6 and Figure 4.6, it can be shown that σ_b is given by:

$$\sigma_b = \frac{m_1 L_1 (Z_1 + Z_3) + m_2 L_1 (Z_o + Z_3)}{m_1 + m_1} \tag{4.11}$$

Equation 4.11 can be rearranged to yield

$$Z_3 = \frac{(m_1+m_2)\ \sigma_b - m_1\sigma_s - m_2\sigma_o}{m_2 L_1} \tag{4.12}$$

with

$$\sigma_o = L_1 Z_o(T) \tag{4.13}$$

where σ_o is taken as the .2% offset yield stress, i.e., an initial value of Z. The values of σ_b and σ_o and the calculated values of Z_3 are summarized in Table 4.2. Also, it is assumed $Z_2 = Z_o$ for most materials (Step 6). For specimens subjected to full thermal recovery, Z_o is best estimated using slow rate tensile results. Once Z_3 and Z_1 are obtained, Z_o can be refined by fitting the model calculation to the tensile stress-strain curve (Step 6), and Z_2 is again set to equal Z_o.

The effect of static thermal recovery on the work hardening rate can be included in a similar manner. Assuming $A_1 = A_2 = A$ and $r_1 = r_2 = r$, the

expression for γ including the recovery term can be shown to have the form (see Appendix):

$$\gamma = L_1[m_1(Z_1+Z_3) + m_2(Z_o+Z_3)] - (m_1+m_2)\sigma - \frac{A(L_1Z_1)^{1-r}}{\sigma\dot{\varepsilon}^p}\left[\sigma-\sigma_o\right]^r \qquad (4.14)$$

Equation 4.14 is reduced to Equation 4.6 when A is zero; this occurs when static thermal recovery is unimportant. Equation 4.14 also indicates that the dependence of γ on σ is altered when static thermal recovery is present. Thus, it is possible to identify the temperature regime at which static thermal recovery is important by comparing γ-σ data over a range of temperatures (e.g., see Figure 4.7).

The final step (Step 7) is to evaluate the recovery constants. For B1900+Hf, r_1 is assumed to be equal to r_2 ($r_1 = r_2 = r$) and A_1 is also assumed to be equal to A_2 ($A_1 = A_2 = A$) for the following reasons: (1) there is a need to reduce the number of constants and to simplify the procedures for evaluating these constants, (2) the γ-σ curves in Figure 4.7 suggest that they need not be different and might be difficult to distinguish if they were, and (3) no physical mechanisms suggest that they should be different. The recovery constants can be evaluated from either the steady state stress (σ_c) and associated strain rate ($\dot{\varepsilon}_c$) of a slow rate tensile test or the steady state creep rate ($\dot{\varepsilon}_c$) and corresponding stress (σ_c) of a creep test. In both cases, the stresses and the plastic strain rates do not change with time or deformation. Under these conditions, the work hardening parameter, γ, is zero and Equation 28 can be rewritten as:

$$q - A(L_1 Z_1)^{1-r} (\sigma_c - \sigma_o)^r = 0 \qquad (4.15)$$

where $q = \{L_1[m_1(Z_1+Z_3) + m_2(Z_o+Z_3)] - (m_1+m_2)\sigma_c\} \sigma_c \dot{\varepsilon}_c^p$

The recovery exponent r can be obtained from Equation (4.15) as:

$$r = \frac{d \log q}{d \log (\sigma_c - \sigma_o)} \quad ; \quad \sigma_o = L_1 Z_o \qquad (4.16)$$

Figure 4.8 shows data of q vs $\sigma_c - \sigma_o$ in a log-log plot for B1900+Hf at 871, 982,, and 1093°C. The results indicate that the values of r are equal to 2 at these temperatures. Once r is obtained, the recovery constant A can be calculated using Equation (4.15). Alternately, A can also be evaluated by considering individually the conditions for which the isotropic hardening and the directional hardening rates are zero. In general, they both give the same result. If different A values are obtained, the one which gives the best fit to the tensile stress-strain curve at $\dot{\varepsilon} = 4 \times 10^{-7}$ sec^{-1} is used.

A summary of the material constants of B1900+Hf using this set of procedures is shown in Table 4.3 as well as in Figure 4.9. There are only four temperature-dependent materials constants in the Bodner-Partom model, namely, n, Z_o, Z_2 and A. Since Z_2 is generally taken to equal Z_o, only Z_o, n and A need to be evaluated as a function of temperature. For the B1900+Hf alloy, Z_o, n, and A are temperature-dependent only at temperatures above 760°C. The dependence of Z_o or temperature can be described by the following two empirical expressions:

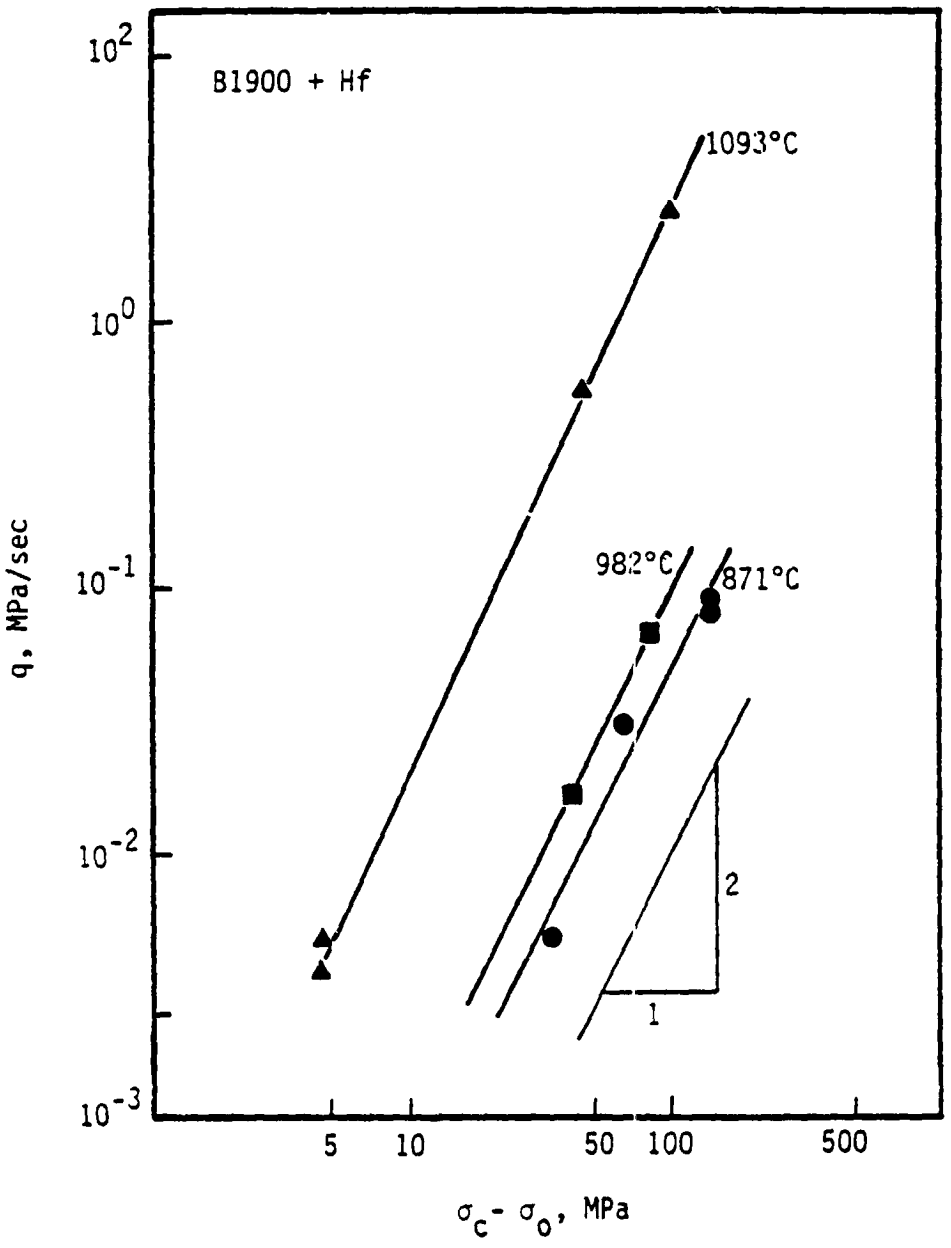

FIGURE 4.8. THE SLOPES OF THE q VS. σ_c-σ_o CURVES FOR B1900+Hf ARE APPROXIMATELY TWO AT 871, 982, AND 1093°C.

TABLE 4.3

BODNER-PARTOM MODEL CONSTANTS FOR B1900+Hf

- **Temperature-Independent Constants**

$m_1 = .270\ MPa^{-1}$

$m_2 = 1.52\ MPa^{-1}$

$\alpha_1 = 0.0$

$Z_1 = 3000\ MPa$

$Z_3 = 1150\ MPa$

$r_1 = r_2 = 2$

$D_o = 1 \times 10^4\ sec^{-1}$

- **Temperature-Dependent Constants**

Constants	Temperature, °C			
	T ≤ 760°C	871°C	982°C	1093°C
n	1.055	1.03	.850	.70
Z_o (MPa)	2700	2400	1900	1200
$A_1 = A_2\ (sec^{-1})$	0	.0055	.02	.25
$Z_2 (= Z_o)$ (MPa)	2700	2400	1900	1200

- **Elastic Moduli for B1900+Hf**

$E = 1.987 \times 10^5 + 16.78\ T - .1034\ T^2 + 1.143 \times 10^{-5}\ T^3$ MPa with T in °C.

$G = 8.650 \times 10^4 - 17.58\ T + 2.321 \times 10^{-2}\ T^2 - 3.464 \times 10^{-5}\ T^3$ MPa with T in °C

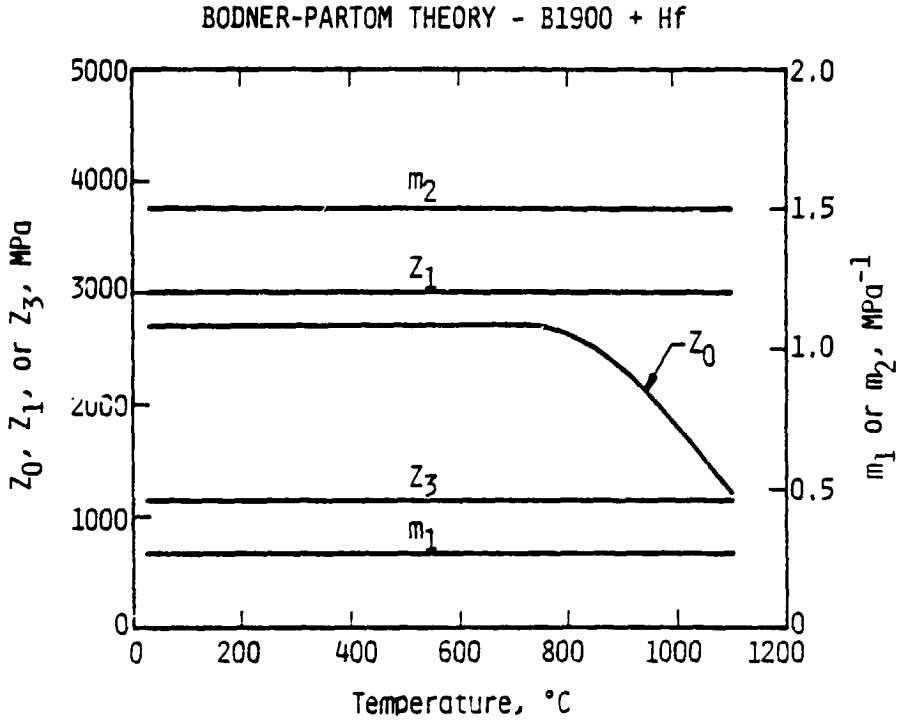

(a)

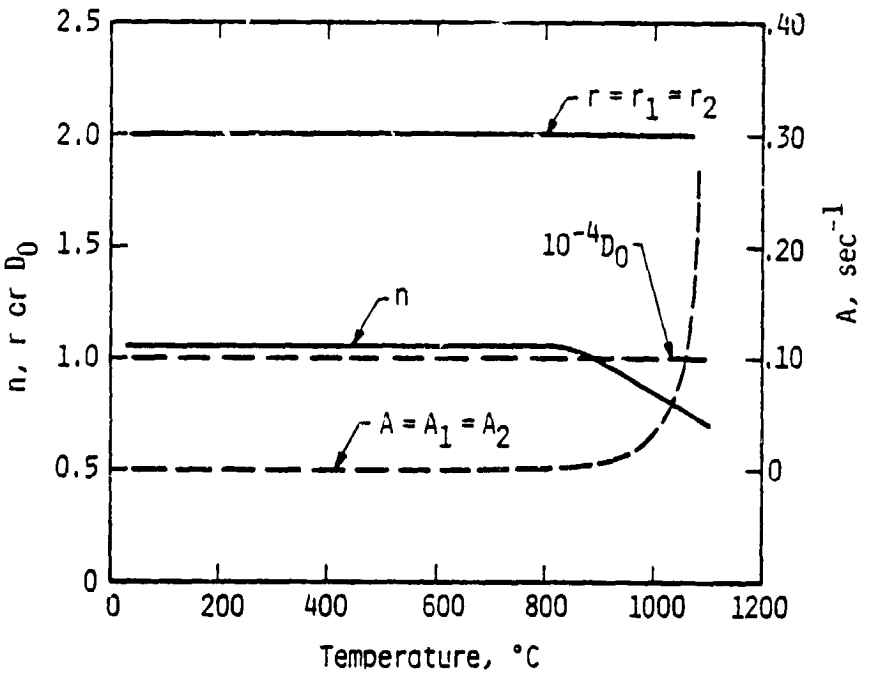

(b)

FIGURE 4.9. BODNER-PARTOM MODEL CONSTANTS FOR B1900+Hf AS FUNCTION OF TEMPERATURE.

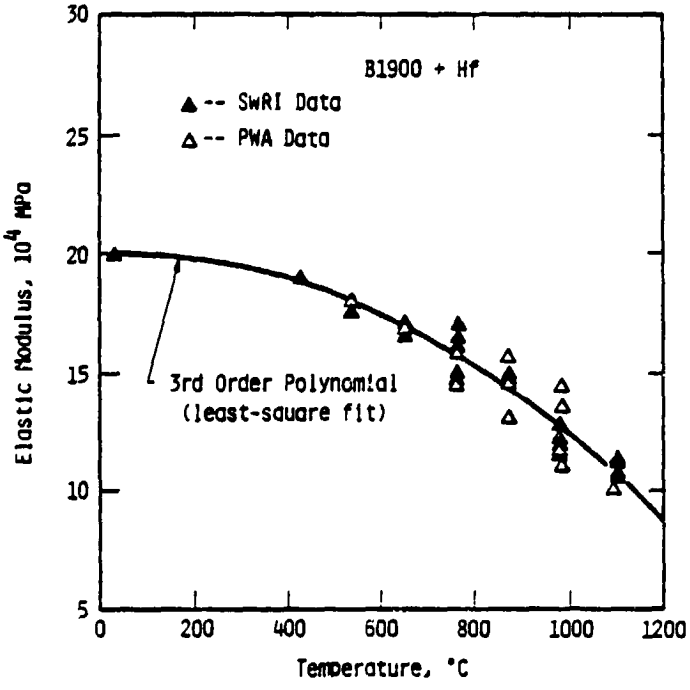

(a)

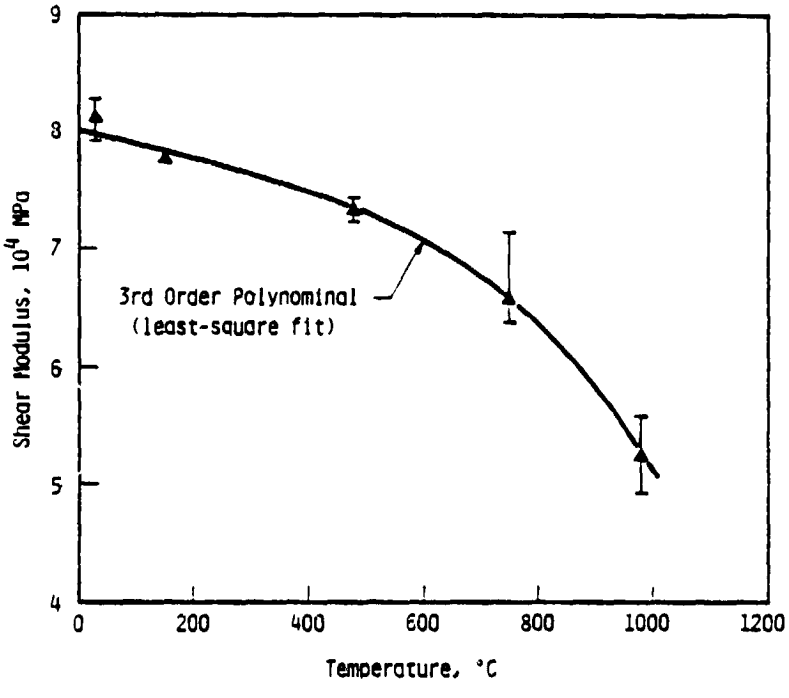

(b)

FIGURE 4.10. THE ELASTIC AND SHEAR MODULI OF B1900+Hf AS FUNCTION OF TEMPERATURE: (A) ELASTIC MODULUS, (B) SHEAR MODULUS.

$$Z_o = 2700 \text{ MPa}, \quad T \leq 838°K \tag{4.17}$$

and $$Z_o = -4950 + \frac{8.5\times10^6}{T} \text{ MPa}, \quad T > 863.4 \text{ K}$$

The empirical relationships relating n and temperature are:

$$n = 1.055 \quad \text{for} \quad T \leq 863.4°K \tag{4.18}$$

and $$n = -1.0524 + \frac{2394.74}{T} \quad \text{for } T > 863.4°K$$

The constant A in the thermal recovery term is best expressed as an exponential function of temperature. The choice of the functional form is suggested by Friedel's recovery model [10] and based on the consideration that thermal recovery is controlled by diffusion and should have a similar functional form. As shown in Figure 4.10, the constant A for B1900+Hf can be expressed as:

$$A = 1.319\times10^9 \exp\left(-\frac{30580}{T}\right) \text{sec}^{-1} \tag{4.19}$$

where T is in °K. It should be noted that at temperatures below 760°C, the value of A obtained from Equation (4.19) is negligibly small so that it is essentially zero and thermal recovery is unimportant. The elastic and the shear moduli obtained from the slope of the tensile and the shear strain-strain curves were also expressed as a function of temperature by fitting data to a third order polynominal equation. The expressions for the elastic and the shear moduli of B1900+Hf, shown in Table 4.3, are compared with the experimental data in Figure 4.10(a) and (b), respectively.

4.2.2 Modified Walker Model

Two strategies have been developed for determining constants in the Walker constitutive theory. The first approach requires simple tensile or

creep testing supplemented with limited cyclic data to establish, in a straightforward manner, the variation with temperature of the model constants. Test and analysis requirements are minimized but there is no guarantee, a priori, that the resultant model will reproduce material behavior under component relevant strain cycles. The second approach, which is described in [1], proceeds from the notion that the most appropriate test for determining constants is that which most closely represents the intended application. This approach necessarily involves considerable trial and error before test data and predictions match. The use of optimization techniques has been found to be of some value in this regard.

All the Walker model constants for B1900+Hf in this report have been determined using the first approach. An outline of the systematic procedure to establish the Walker model constants is presented in Figure 4.11. The data requirement at each temperature consists of a series of monotonic tensile tests at different strain rates and/or creep tests at different stress levels and fully reversed cyclic tests at one, but preferably two strain rates. The monotonic tensile stress-strain results at high strain rates allow η_{11}, η_9, and η_{10} to be estimated directly. η_{11} is seen to be approximately equal to the initial value of the strain hardening rate, $d\sigma/d\varepsilon_p$. The difference between the limit and the yield strength determines the ratio, η_{11}/η_9. $\eta_{10}\Omega_{21im1}$ is selected so that $\dot{\Omega}_2$ (and therefore Ω_{21im}) is small except for the strain rates at which linear hardening is noted. Iterative analysis is required to establish the remaining constants. A plot of the limiting or large strain value of the excess stress ($S_{ij} - \Omega_{11im} - \Omega_{21im}$) against the log of $\dot{\varepsilon}_p$ should be linear with a slope of K_1 and one cycle intercept beta, but Ω_{21im}, as we have seen, and Ω_{11im} are typically functions of strain rate.

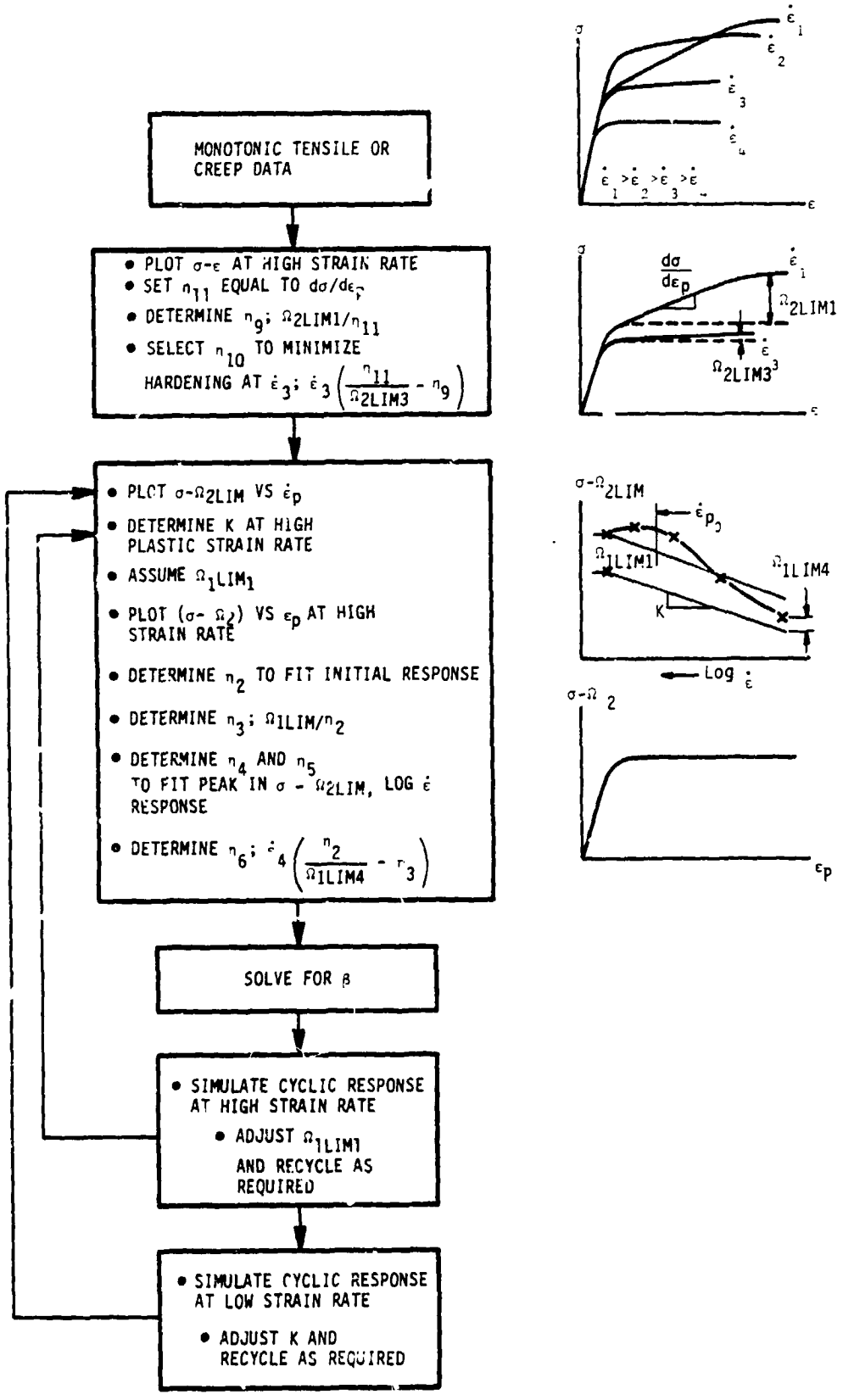

FIGURE 4.11. A SCHEMATIC PROCEDURE FOR EVALUATION OF THE MATERIAL CONSTANTS IN THE EXPONENTIAL FORM OF THE WALKER THEORY.

Determination of the constants η_2 through η_6 begins by plotting the quantity $(\sigma_{1lim}-\Omega_{2lim}(\dot{\varepsilon}_p))$ versus the log of $\dot{\varepsilon}_p$. A straight line indicates that strain aging (η_4 and η_5) and thermal recovery (η_6) effects are small and Ω_{1lim} is a constant, independent of the plastic strain rate. A sigmoidal curve indicates that thermal recovery (η_6) is present and a local peak in the $\sigma_{1lim} - \Omega_{2lim}$ (ε_p) versus log of $\dot{\varepsilon}_p$ plot at a strain rate of $\dot{\varepsilon}_{po}$ indicates that strain aging effects must also be modelled. At limit conditions, $\dot{\Omega}_1 = 0$, and

$$\Omega_{1lim}(\dot{\varepsilon}_p) = \frac{1}{\eta_3/\eta_2 + \eta_4/\eta_2 e^{-\eta_5|\log \dot{\varepsilon}_p/\dot{\varepsilon}_{po}|} + \eta_6/\eta_2\dot{\varepsilon}_p}$$

At high strain rates, significantly removed from $\dot{\varepsilon}_{po}$, the second and third terms in the denominator can be ignored and the ratio η_2/η_3 can be set equal to a provisional value of Ω_{1lim1}. K_1 can be determined as the slope of $(\sigma_{1lim} - \Omega_{1lim1} - \Omega_{2lim1})$ versus log of $\dot{\varepsilon}_p$ in this region of the curve. At very low strain rates, the third term in the denominator dominates and the ratio η_6/η_2 can be determined from the relationship

$$\eta_6/\eta_2 = \frac{\dot{\varepsilon}_{p4}}{\Omega_{1lim4}}$$

where Ω_{1lim4} is the saturated back stress at a plastic strain rate $\dot{\varepsilon}_{p4}$ required to linearize the excess stress $(\sigma_{1lim} - \Omega_{2lim} - \Omega_{1lim})$ versus log of $\dot{\varepsilon}_p$ plot. Finally, η_5 and the ratio η_4/η_2 are selected to match the variation of Ω_{1lim} with $\dot{\varepsilon}_p$ due to strain aging effects in the vicinity of $\dot{\varepsilon}_{po}$. η_2 is now determined to provide an optimum fit of the monotonic tensile curve (variation of $\dot{\varepsilon}_p$ with $\sigma - \Omega_2(\varepsilon_p)$) at high strain rate. The constants η_3, η_4 and η_6 are,

TABLE 4.4

CONSTANTS FOR THE EXPONENTIAL FORM OF WALKER'S MODEL FOR B1900+Hf

Temp, °C	21	427	538	649	760	871	982	1093
E (Modulus), MPa	1.900 E+5	1.900 E+5	1.900 E+5	1.800 E+5	1.655 E+5	1.438 E+5	1.249 E+5	1.161 E+5
ν (Poisson's Ratio)	.322	.328	.331	.334	.33?	.324	.351	.351
K_1, MPa	12.4	12.4	12.4	12.4	13.8	16.6	13.8	9.0
K_2, MPa	0	0	0	0	0	0	0	0
K_3, MPa	0	0	0	0	0	0	0	0
β, MPa	1.73 E11	1.73 E11	1.73 E11	3.862 E10	2.55 E10	5.50 E12	4.20 E10	5.57 E9
η_2, MPa	2.41 E6	2.41 E6	2.41 E6	8.27 E5	8.27 E5	2.36 E6	9.65 E4	2.36 E4
η_3	4794.	4794.	4794.	1714.	1880.	621.2	400.0	278.7
η_4	0	0	0	0	-585	0	0	0
η_5	.3117	.3117	.3117	.3117	.3117	.3117	.3117	.3117
η_6	0	0	0	0	0	8.73 E-4	4.29 E-4	4.83 E-2
η_7	0	0	0	0	0	0	0	0
η_8	0	0	0	0	0	0	0	0
η_9	11.87	11.87	11.87	16.64	19.83	59.33	136.0	136.0
η_{10}	0	0	0	0	2.44 E-3	2.44 E-3	2.44 E-3	2.44 E-3
η_{11}, MPa	4.70 E3	4.70 E3	4.70 E3	4.70 E3	4.70 E3	9.65 E2	0	0
$\dot{\Omega}$, MPa	0	0	0	0	0	0	0	0

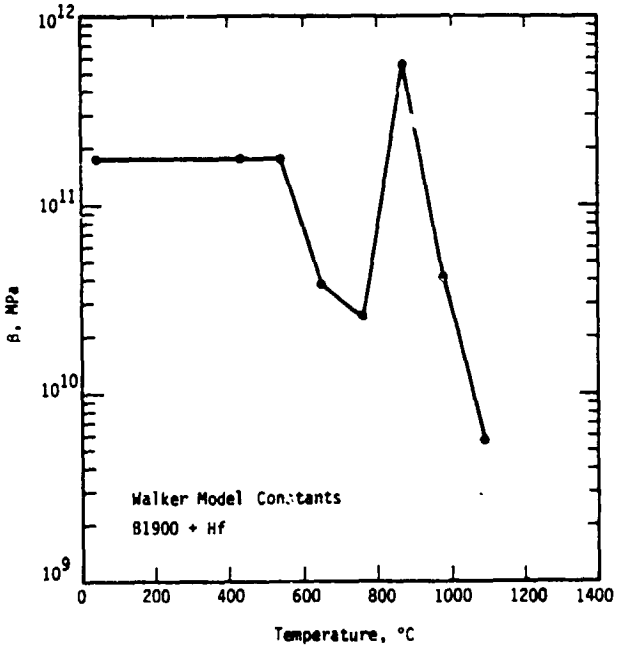

(a)

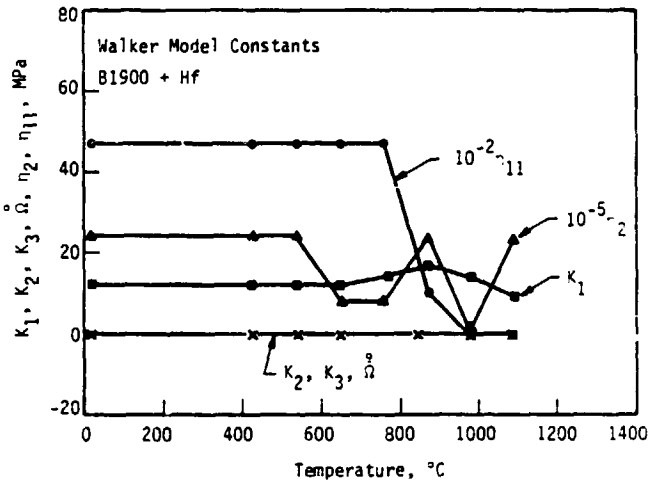

(b)

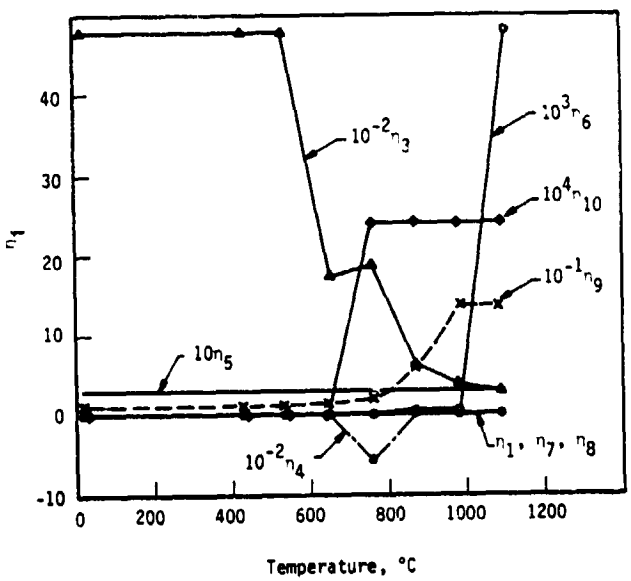

(c)

FIGURE 4.12. WALKER MODEL CONSTANTS FOR B1900+Hf AS FUNCTION OF TEMPERATURE.

therefore, determined for the provisional value of $\Omega_{1\text{liml}}$. B can be solved directly, completing the trial determination of the constants.

The material constants for the modified Walker model for B1900+Hf are presented in Table 4.4 as well as in Figure 4.12 as a function of temperature. Isothermal tensile and a limited number of one way cyclic test results were used to determine these values. Creep, dwell fatigue, and TMF data were not considered in the selection of the model constants.

4.3 Correlation of Theoretical and Experimental Results

4.3.1 Uniaxial Tensile Behavior

Figure 4.13 shows the monotonic tensile results and corresponding model predictions at three temperatures and a fixed strain rate of 8.3×10^{-5} sec^{-1}. Both models provide a good fit of the data. The effect of strain rate on the 0.2% ε^p yield stress at 760, 871, 982, and 1093°C is shown in Figure 4.14. The Bodner-Partom model predicts an increase of yield stress with strain rate at all temperatures. The thermal recovery term is absent in the 760°C calculations but is dominant at 1093°C. The change in the slopes of the Bodner-Partom model calculations at 871 and 982°C represents a transition from a thermal recovery dominated regime at slow strain rates ($\dot{\varepsilon} \leq 1x10^{-5}$ sec^{-1}) to a hardening dominated regime with relatively little thermal recovery at high strain rates ($\dot{\varepsilon} \geq 1x10^{-3}sec^{-1}$). By including a strain-aging term in the equilibrium stress, the Walker model is able to correlate the decrease in yield strength with strain rate that is observed at 760°C at $\dot{\varepsilon} \geq 1x10^{-3}sec^{-1}$.

The temperature dependence of the .2% ε^p yield stress at various strain rates is shown in Figure 4.15. The Bodner-Partom model reproduces the

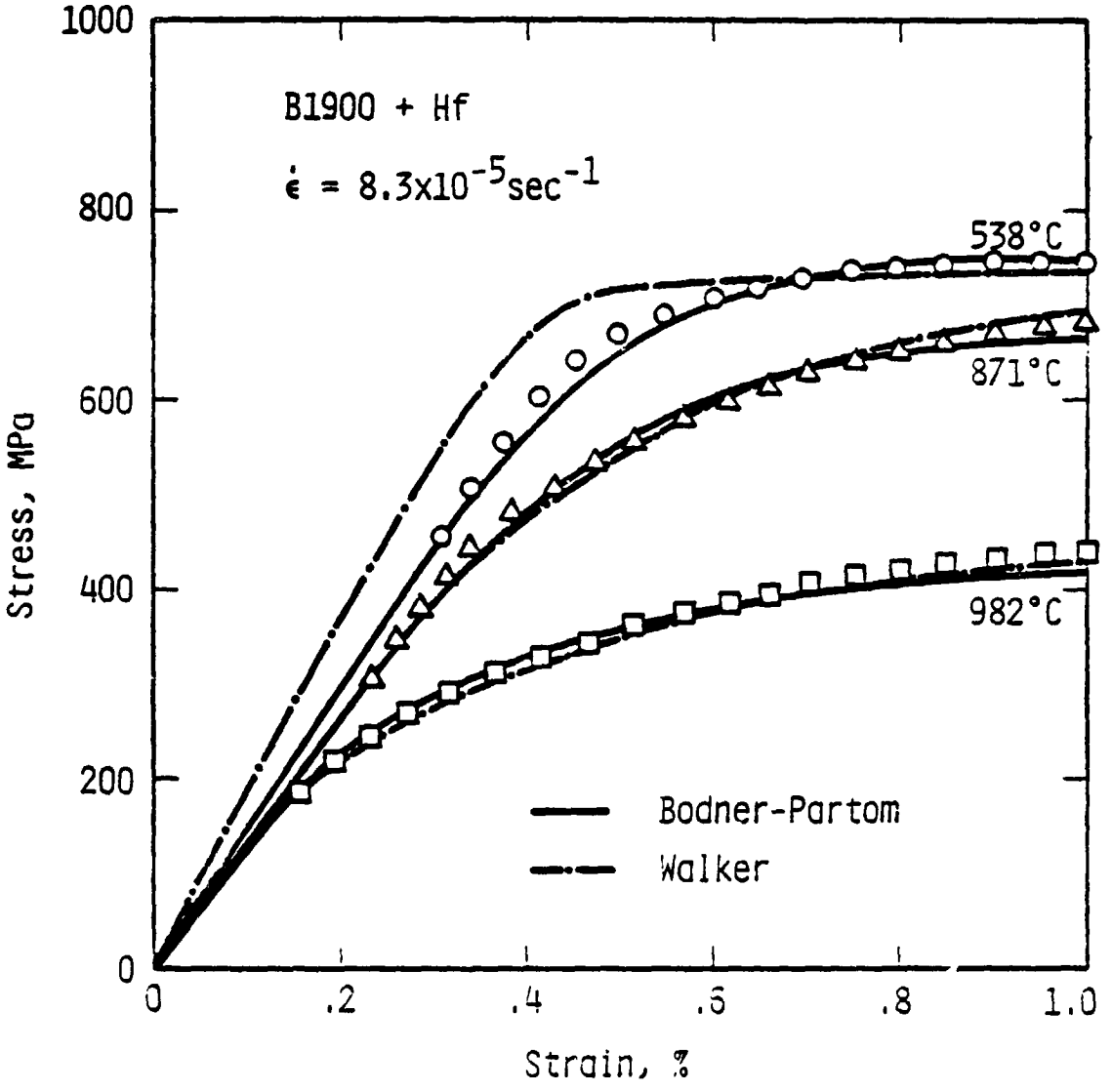

FIGURE 4.13. COMPARISON OF EXPERIMENTAL AND CALCULATED STRESS-STRAIN CURVES OF B1900+Hf AT THREE TEMPERATURES.

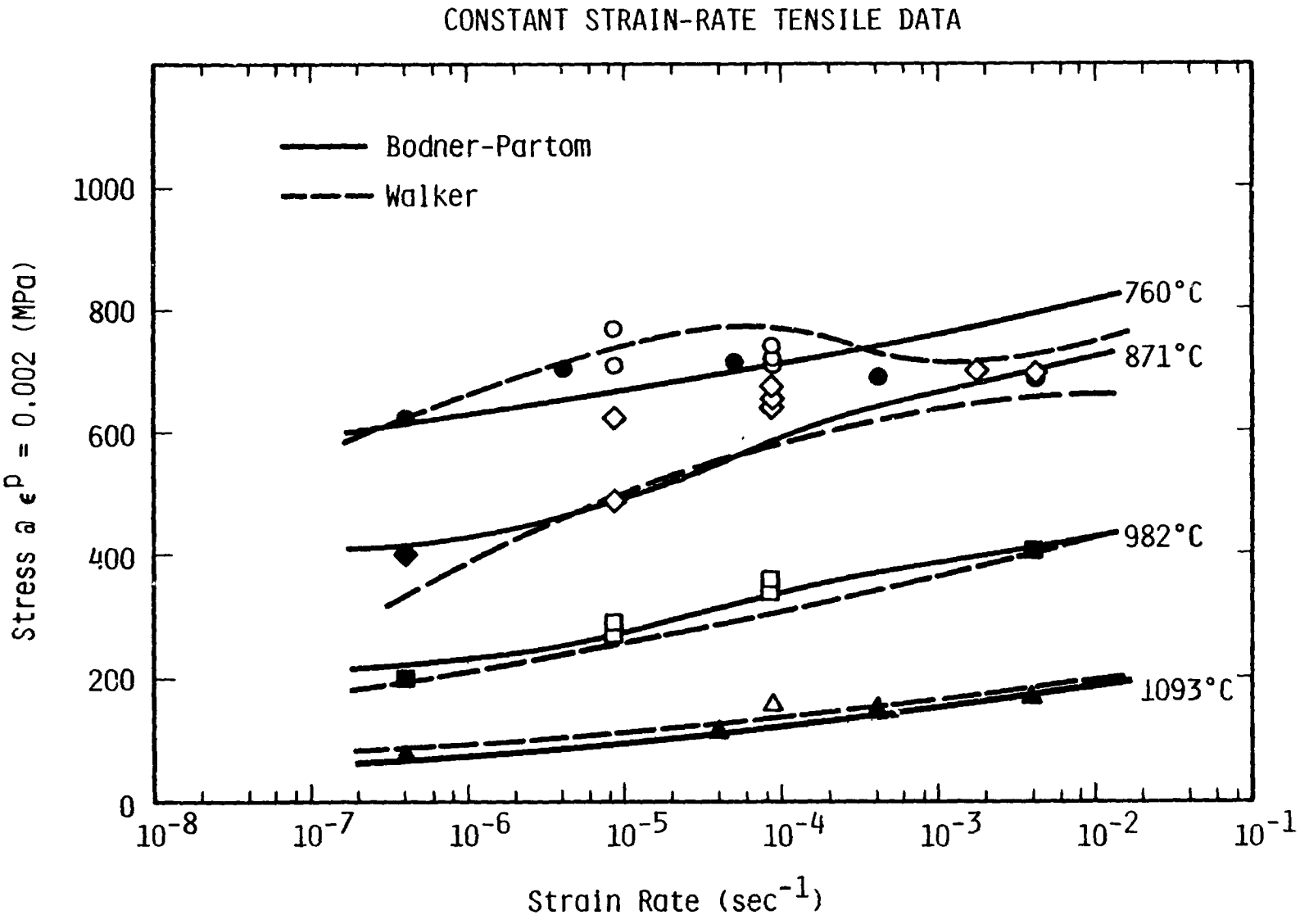

FIGURE 4.14. THE EXPERIMENTAL AND CALCULATED .2% ϵ^p YIELD STRESS OF B1900+Hf AT VARIOUS TEMPERATURES AS FUNCTION OF STRAIN RATE.

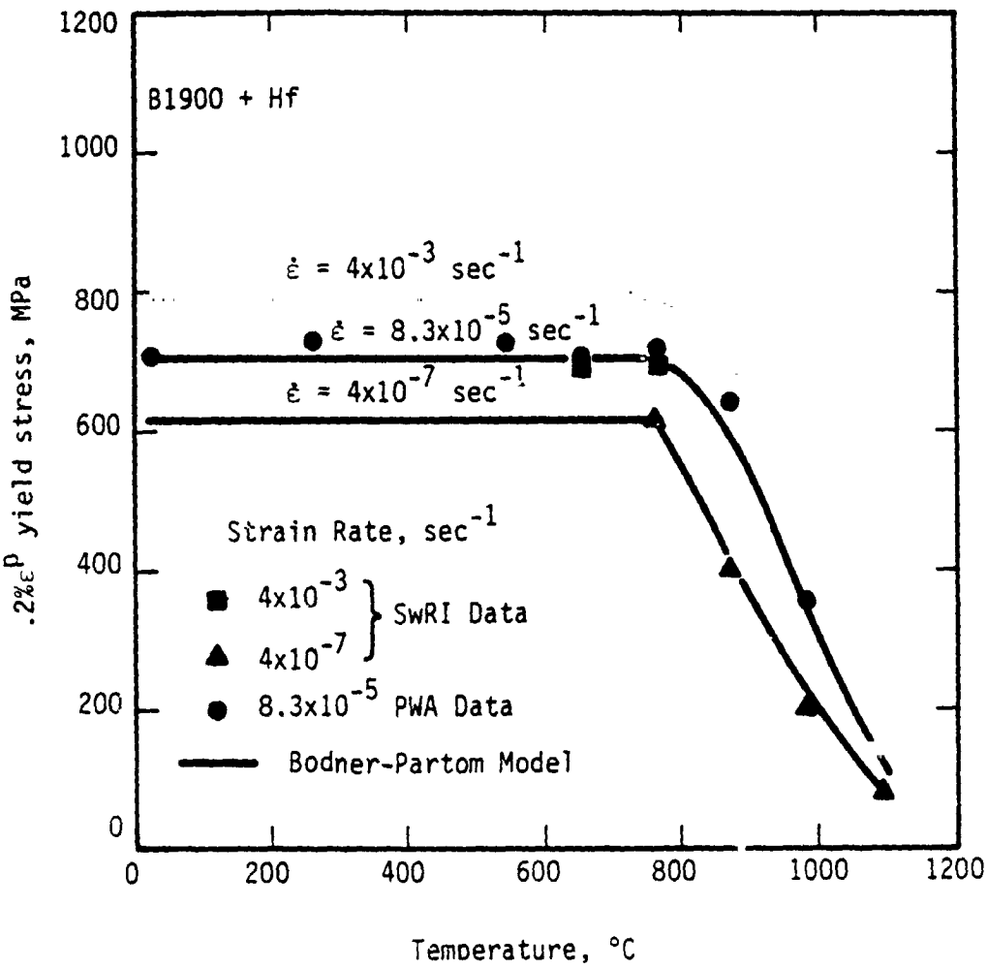

FIGURE 4.15. THE CALCULATED AND EXPERIMENTAL .2% ε^p YIELD STRESS AT THREE STRAIN RATES AS FUNCTION OF TEMPERATURE.

experimental data rather well. The experimental and calculated yield stresses are seen to be relatively constant and independent of temperature at $T \leq 760°C$ but decrease rapidly with temperature at $T > 760°C$.

4.3.2 Creep Behavior

The variation of the steady-state creep rate with test temperature and stress level is presented in Figure 4.16. Note that predictions obtained using the Bodner-Partom model give somewhat better agreement with the experimental data than the Walker model at 760°C and at low strain rates at 871°C. This finding is somewhat surprising considering the good fit of the tensile data at these temperatures obtained using the Walker model.

Figure 4.17 shows creep strain vs time at various stress levels at 871°C and 1093°C. The unified models in the present form predict primary and steady state creep regions but not a tertiary region. Comparison of model calculations and experimental data indicates that the creep strain at a given time is predicted fairly accurately by the Bodner-Partom model. It should be noted that the creep curves generally show substantial scatter so that evaluation of model accuracy on the creep response should take this into account.

4.3.3 Uniaxial Cyclic Constitutive Behavior

Representative predicted and experimentally observed saturated hysteresis loops for fully reversed strain cycling at 538°C, 871°C, and 1093°C are shown in Figure 4.18, 4.19, and 4.20, respectively. The shape of the hysteresis loops are predicted fairly well by both models at 538 and 871°C. At 1093°C, both models predict hysteresis loops which tend to be more square than the experimental ones. Furthermore, the Walker model predicted hysteresis loop also shows bi-linear regions.

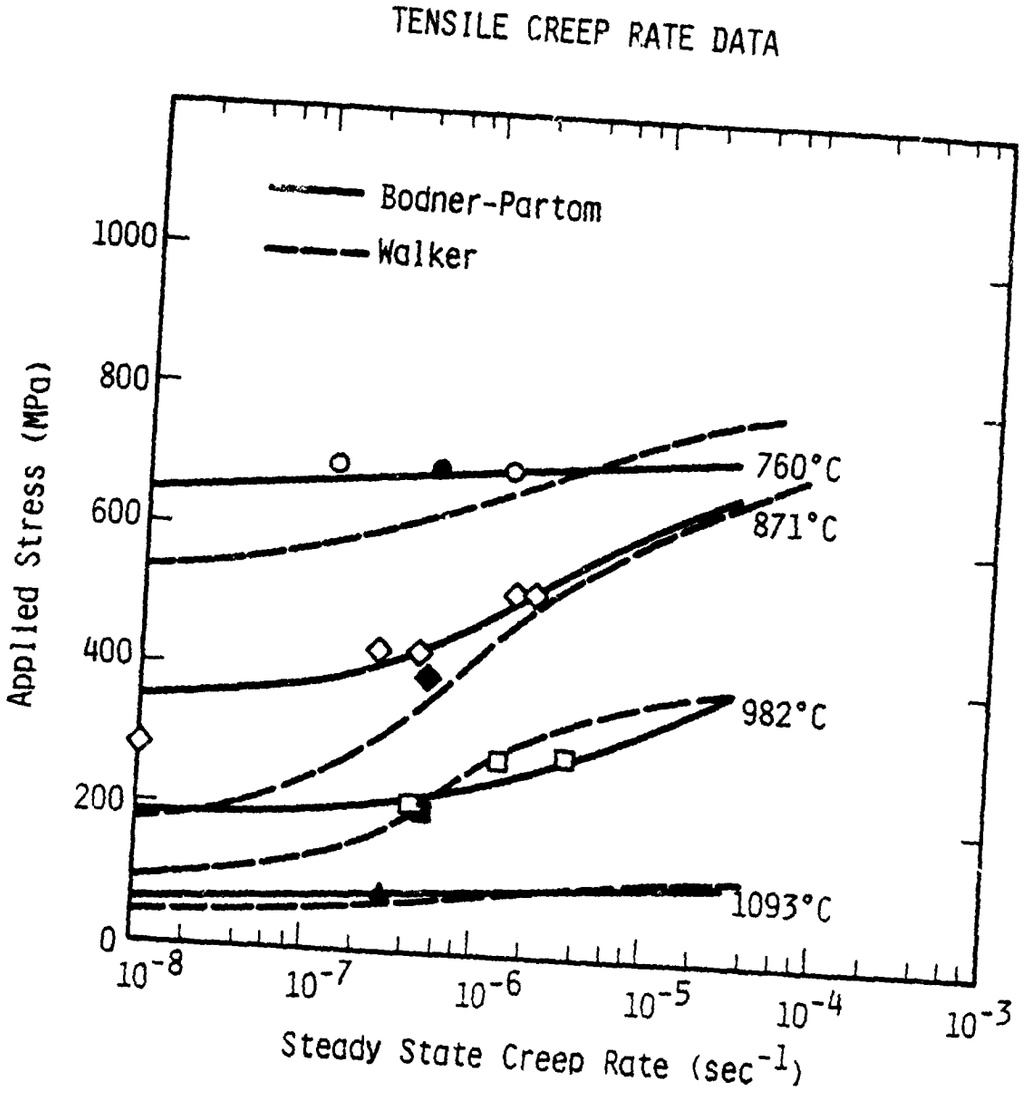

FIGURE 4.16. THE CALCULATED AND EXPERIMENTAL RESULTS OF CONSTANT LOAD CREEP TESTS.

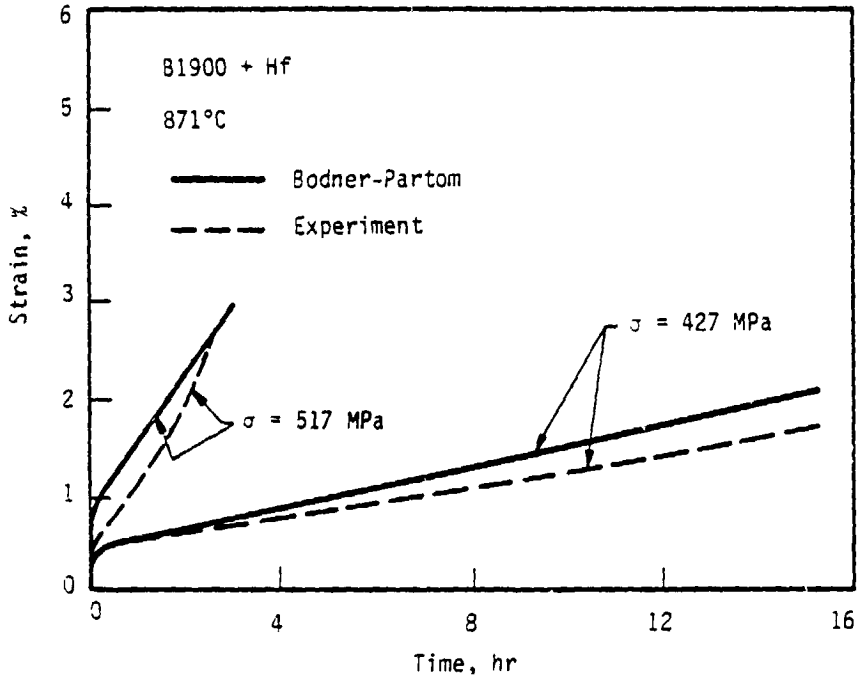

(a)

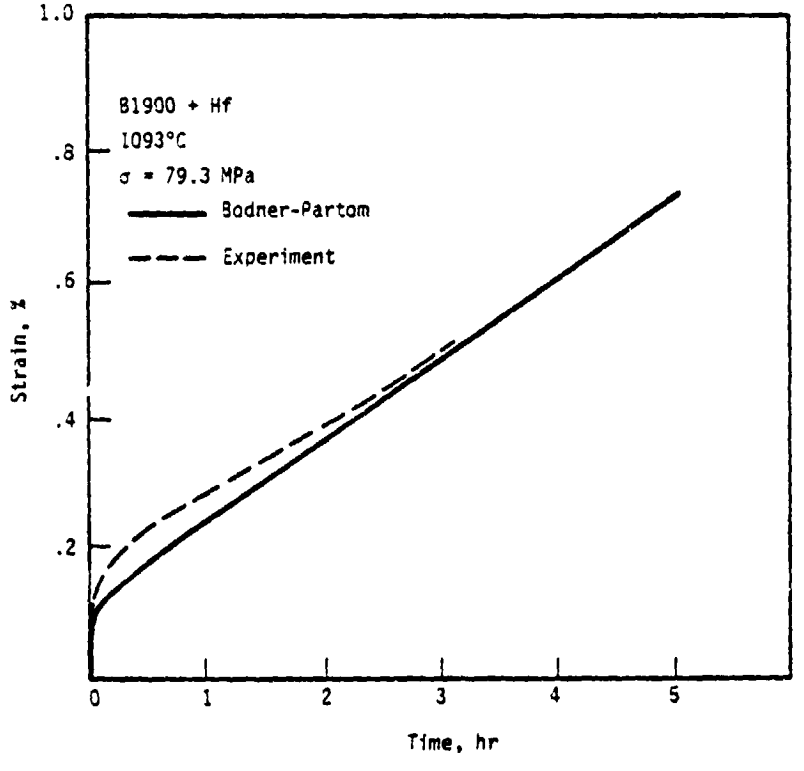

(b)

FIGURE 4.17. THE CALCULATED AND EXPERIMENTAL CREEP CURVES OF B1900+Hf (a) AT 871°C AT TWO STRESS LEVELS, AND (b) AT 1093°C UNDER A STRESS OF 79.3 MPa.

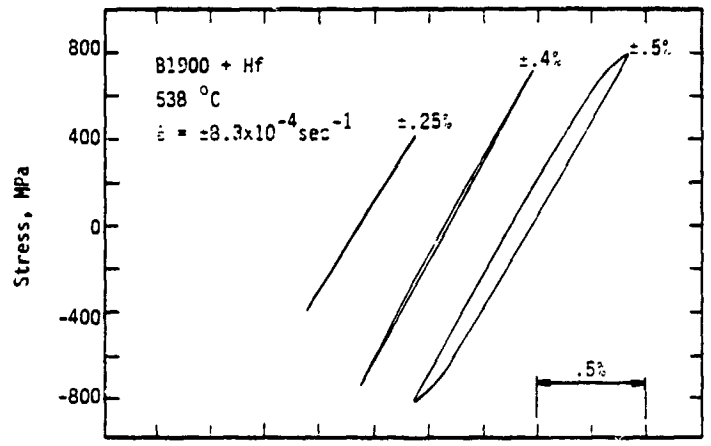

(a) Experiment

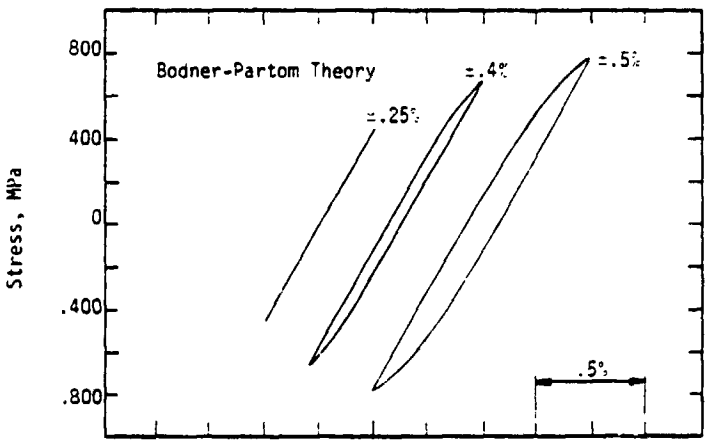

(b) Bodner-Partom Theory

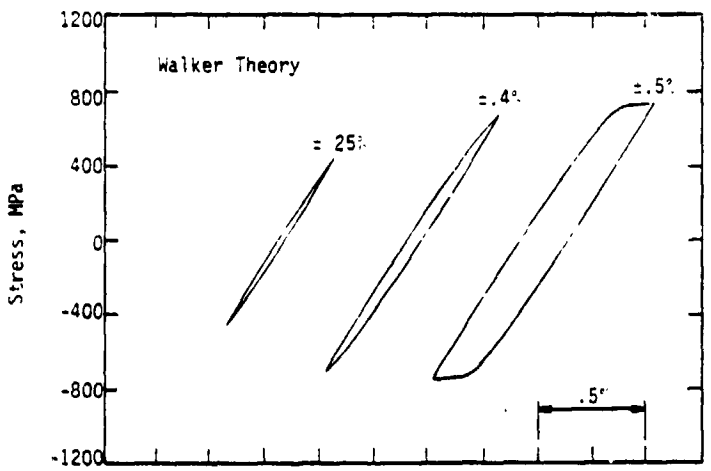

(c) Walker Theory

FIGURE 4.18. COMPARISON OF THE EXPERIMENTAL AND CALCULATED STABLE HYSTERESIS LOOPS OF B1900+Hf AT 538°C.

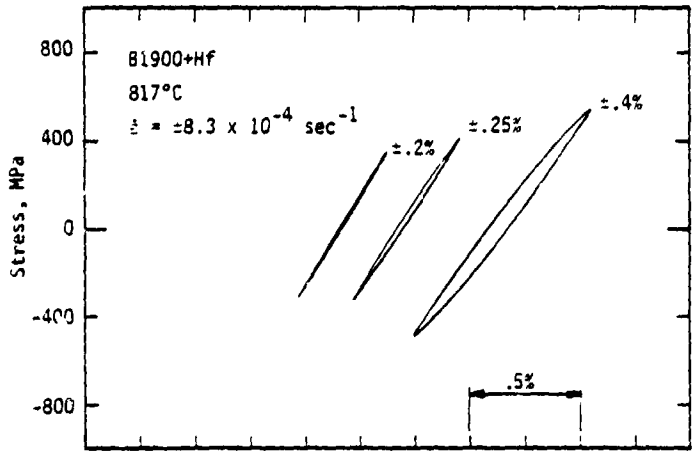

(a) Experiment

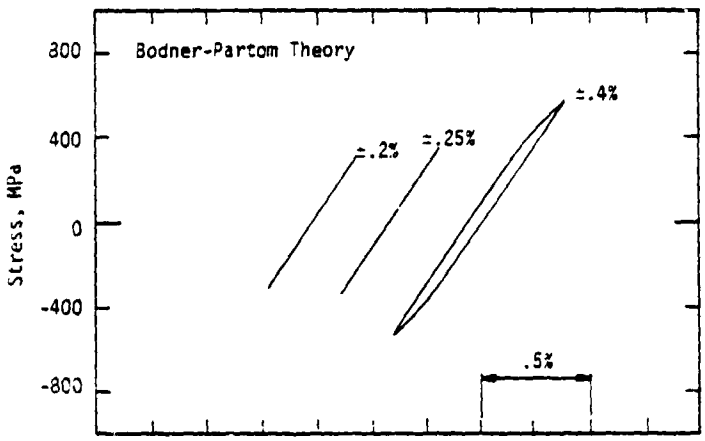

(b) Bodner-Partom Theory

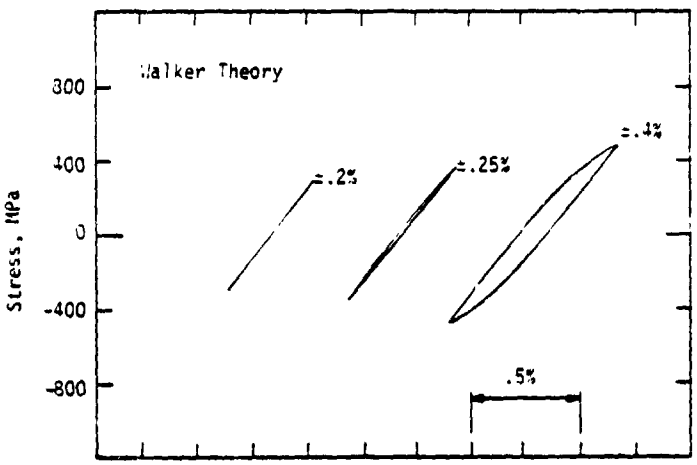

(c) Walker Theory

FIGURE 4.19. COMPARISON OF THE EXPERIMENTAL AND CALCULATED STABLE HYSTERESIS LOOPS OF B1900+Hf AT 871°C.

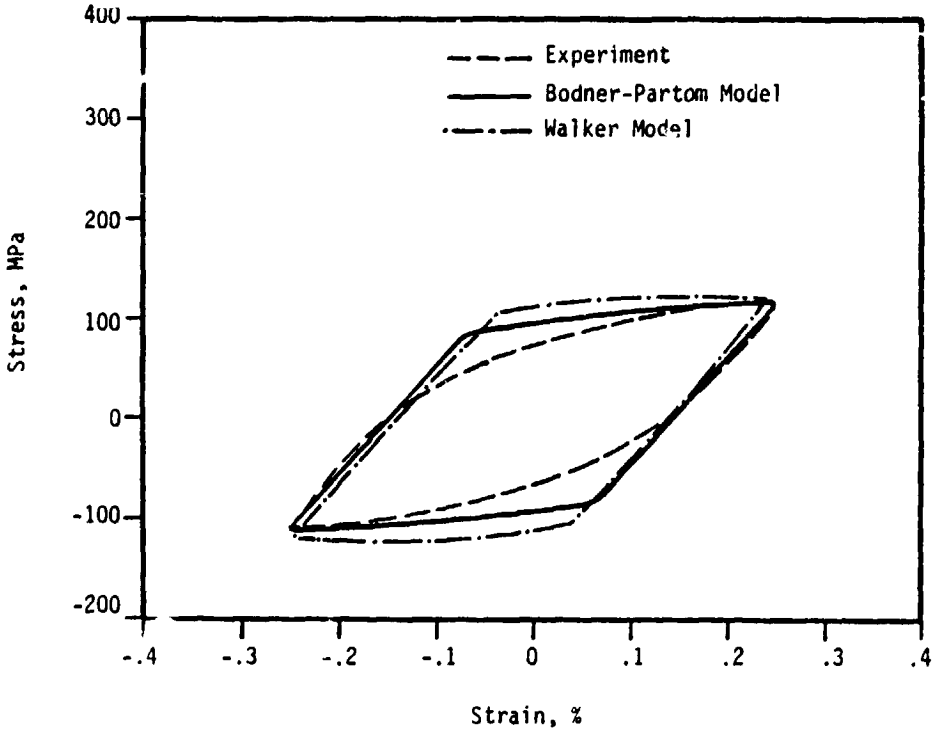

(a)

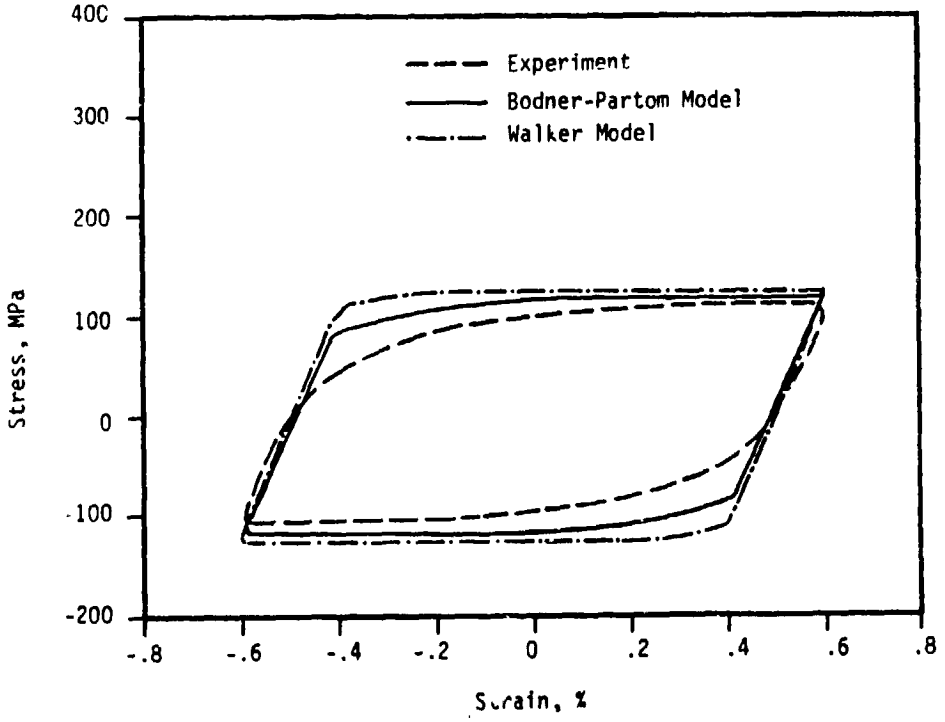

(b)

FIGURE 4.20. COMPARISON OF THE EXPERIMENTAL AND CALCULATED STABLE HYSTERESIS LOOPS OF B1900+Hf AT 1093°C.

The cyclic stress-strain curves were constructed from both the experimental and theoretical results by plotting half of the stress ranges of the fully-reversed saturated hysteresis loop vs half of the imposed strain range. Comparisons of model predictions and experimental data for four different temperatures (760, 871, 982, and 1093°C) are summarized in Figure 4.21. Note that the Bodner-Partom model overpredicted the stress ranges at 871 and 982°C. However, it is worthy to note that none of the cyclic data were used for determining Bodner-Partom constants.

The effects of imposed compressive and tensile mean strains on the cyclic constitutive behavior of B1900+Hf are summarized in Figures 4.22, 4.23, 4.24, and 4.25 with corresponding predictions using both theories at 1093°C, 871°C, 760°C, and 538°C, respectively. For purposes of comparison the half stress range, half cyclic plastic strain range, and mean cyclic stress at both the first and sixth cycle are plotted versus the half strain range for R ratios of 0, -1, and $-\infty$. Two important observations in Figures 4.22-4.25 are: (1) the experimental and theoretical saturated cyclic stress-strain curves ($\Delta\sigma/2$ - $\Delta\varepsilon/2$ curves) appear to be unique at a particular strain rate and temperature and are independent of the R ratios, and (2) both unified models predict a drift in the mean cyclic stress which is not always observed in the experimental data.

At 1093°C, Figure 4.22, both models yield adequate fits of the stress range and cyclic plastic strain range, but the Bodner-Partom model predicts the stress amplitude more accurately in the lower strain range. Both constitutive models match the sixth cycle response of B1900+Hf at 871°C quite well in all three aspects (Figure 4.23). The predicted first cycle mean stress for

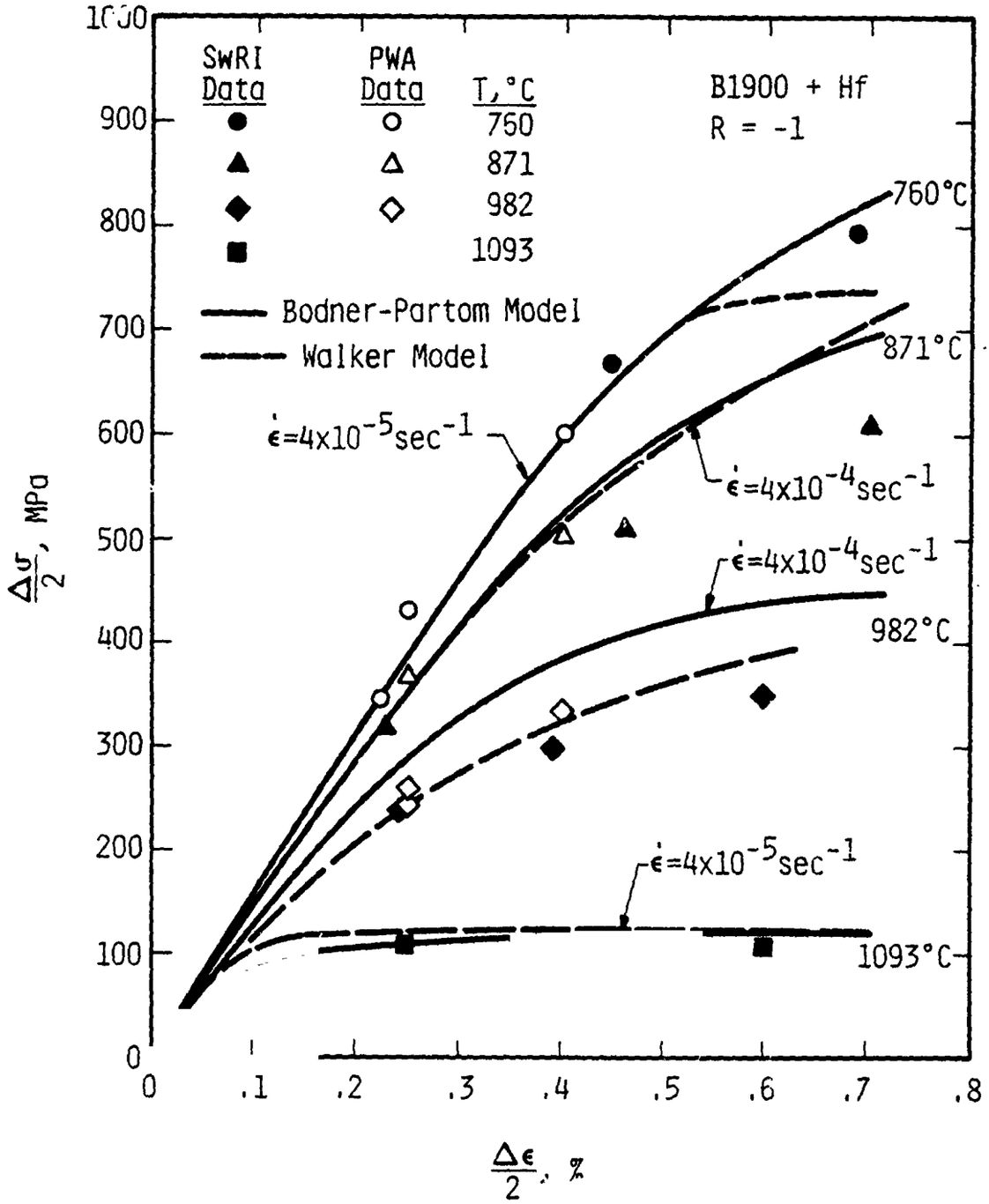

FIGURE 4.21. COMPARISON OF EXPERIMENTAL AND PREDICTED CYCLIC STRESS-STRAIN DATA OF B1900+Hf OBTAINED BY PLOTTING HALF OF THE STRESS RANGE VS. HALF OF THE STRAIN RANGE OF THE STABLE HYSTERESIS LOOP.

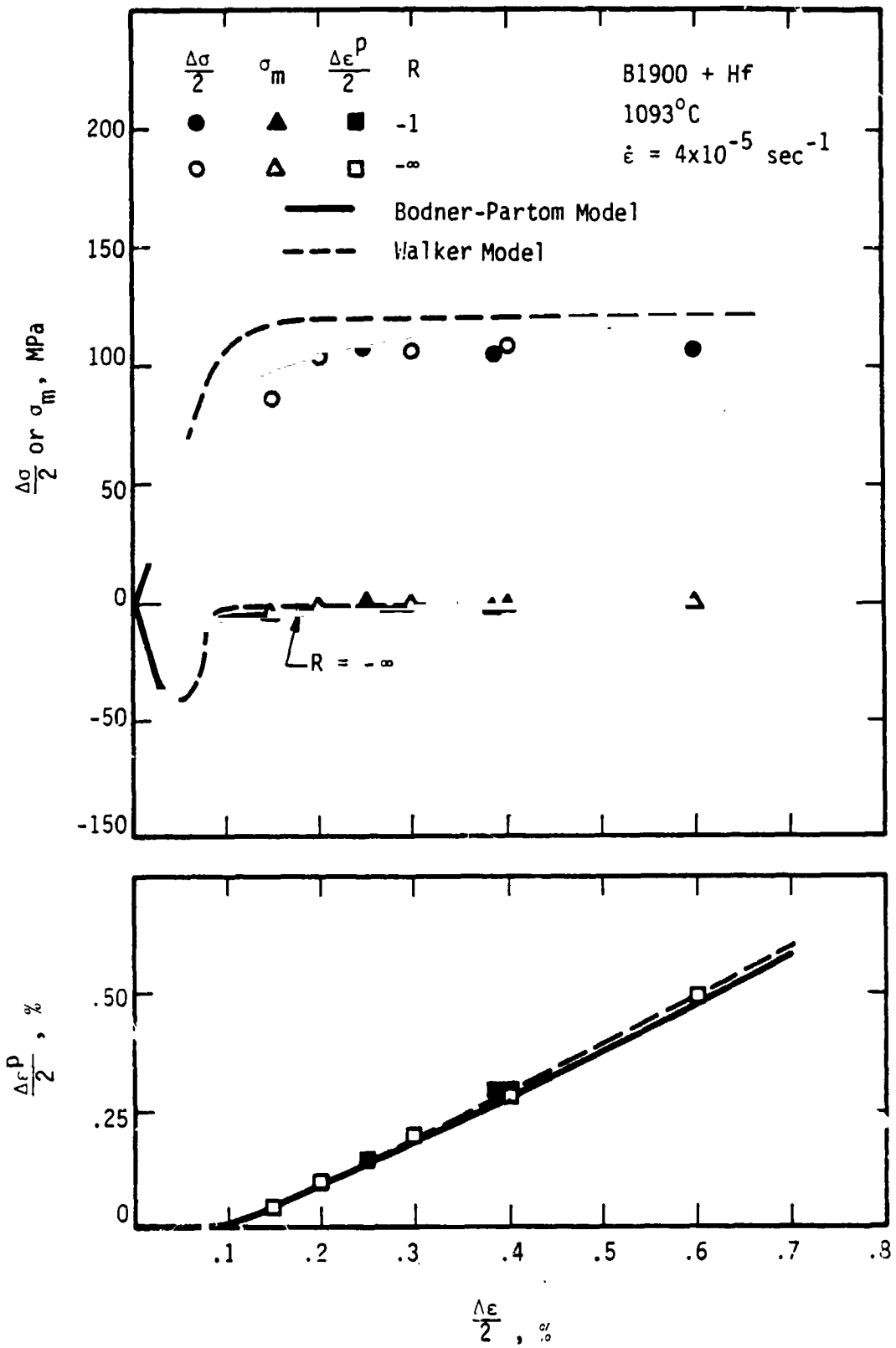

FIGURE 4.22. PREDICTED AND EXPERIMENTAL CYCLIC STRESS-STRAIN DATA, MEAN STRESS, AND PLASTIC STRAIN RANGE OF B1900+Hf UNDER NO MEAN STRAIN OR A COMPRESSIVE MEAN STRAIN AT 1093°C.

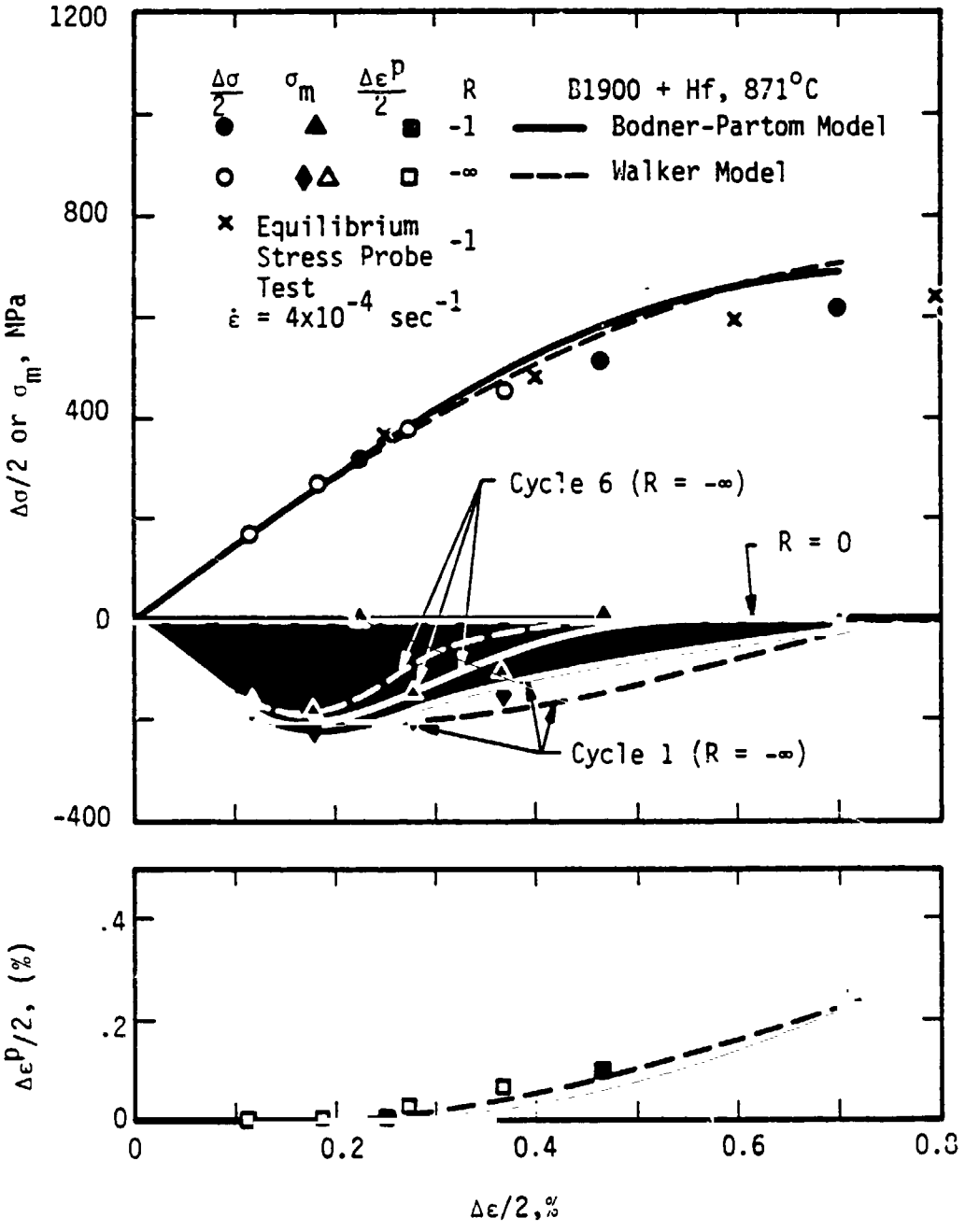

FIGURE 4.23. PREDICTED AND EXPERIMENTAL CYCLIC STRESS-STRAIN DATA, MEAN STRESS, AND PLASTIC STRAIN RANGE OF B1900+Hf UNDER TWO MEAN STRAIN LEVELS AT 871°C.

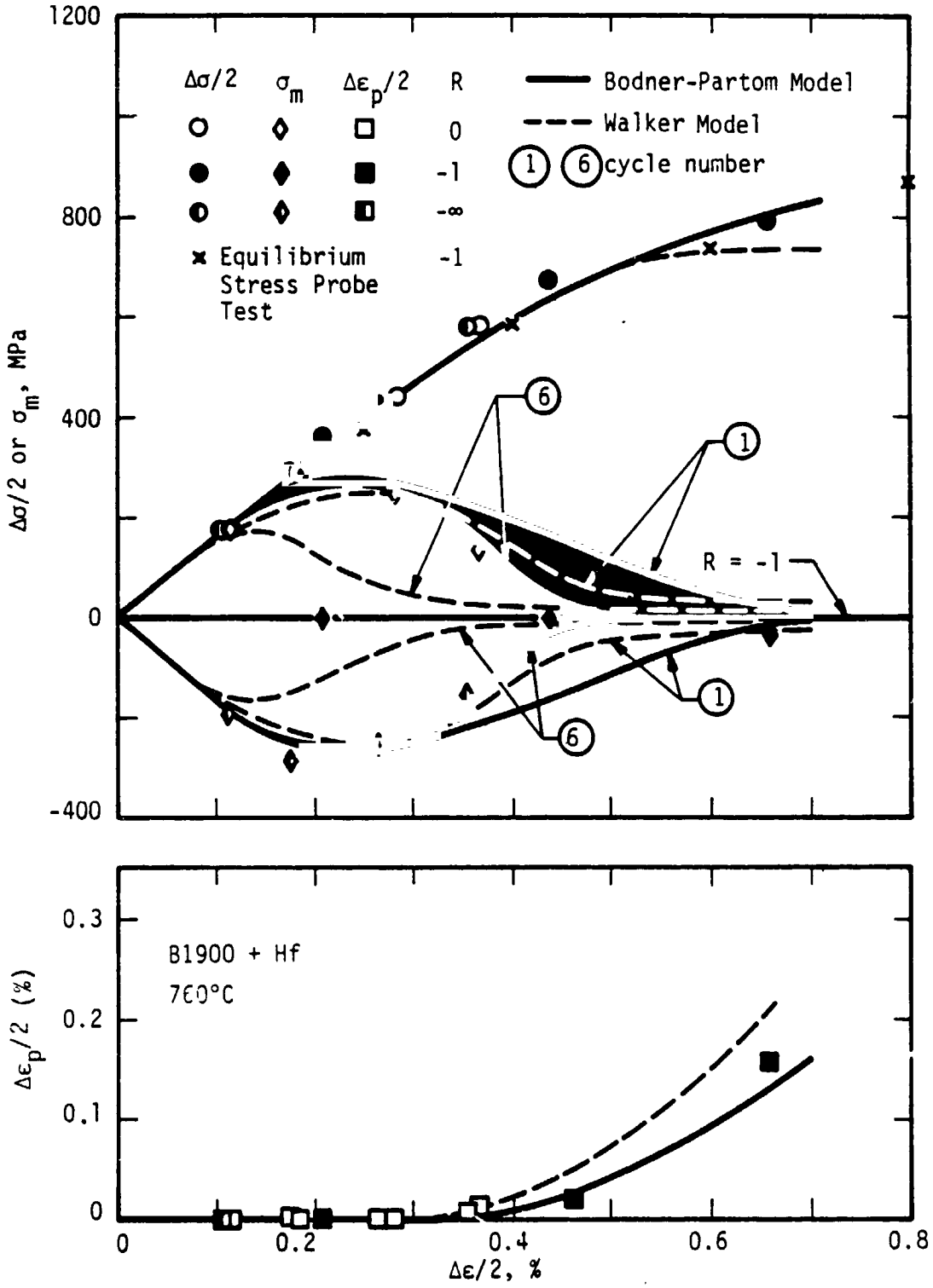

FIGURE 4.24. PREDICTED AND MEASURED CYCLIC STRESS-STRAIN DATA, MEAN STRESS, AND PLASTIC STRAIN RANGE OF B1900+Hf UNDER NO, TENSILE, AND A COMPRESSIVE MEAN STRAIN AT 760°C.

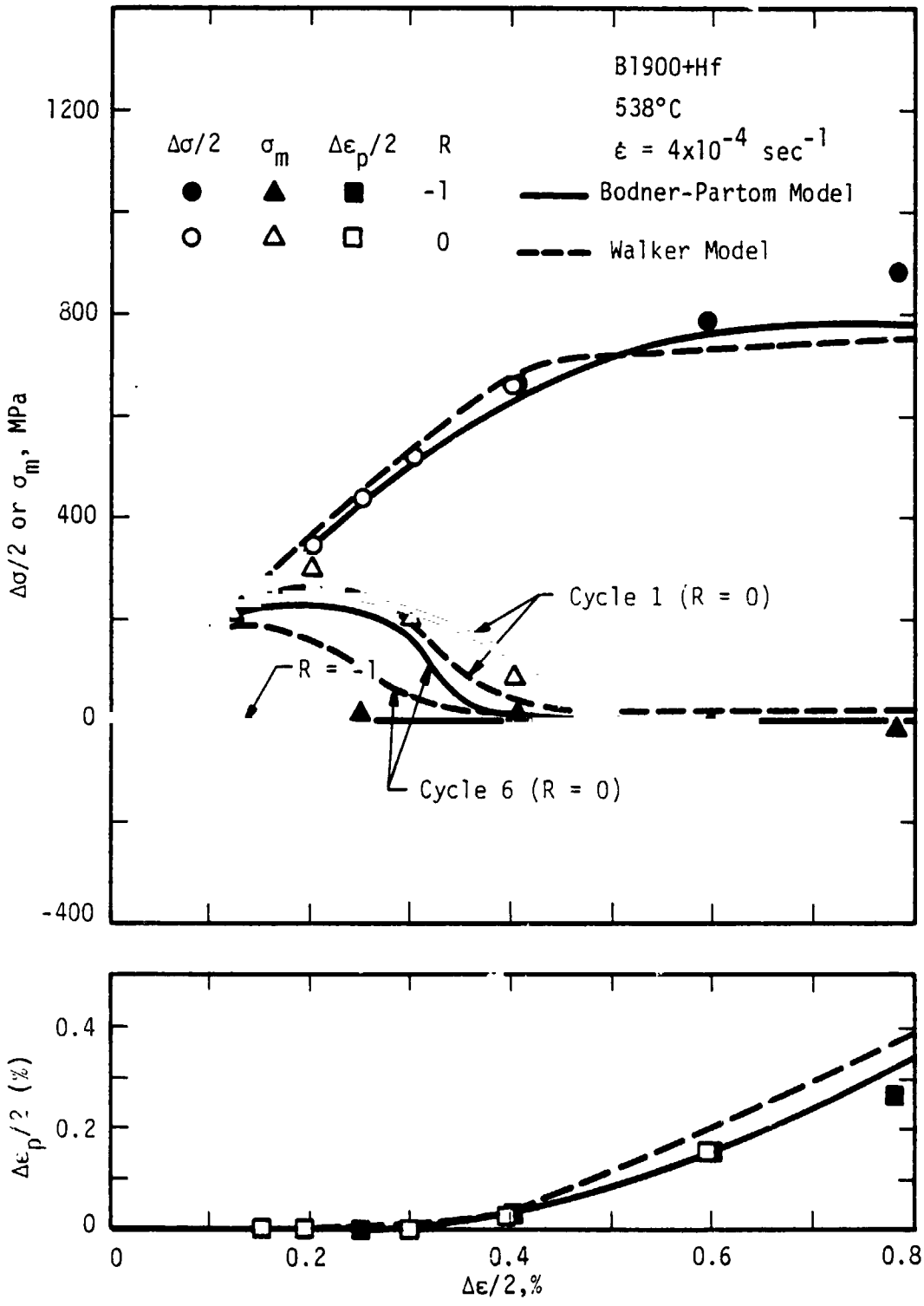

FIGURE 4.25. PREDICTED AND MEASURED CYCLIC STRESS-STRAIN DATA, MEAN STRESS, AND PLASTIC STRAIN RANGE OF B1900+Hf AT NO OR A COMPRESSIVE MEAN STRAIN AT 538°C.

compression cycling is overpredicted using the Walker model, however. At 760°C the Bodner-Partom model prediction agrees with the data experimental quite well in all respects (Figure 4.24). Walker model predicts essentially the same stress range but slightly greater cyclic plasticity than the Bodner-Partom model and a pronounced drift in the cyclic mean stress that was not observed in the data. First cycle test data at 538°C, Figure 4.25, is in good agreement with the predictions obtained using the Walker model but, as noted above, the mean cyclic stress for eccentric strain cycles is predicted to drift appreciably.

Figure 4.22-4.25 also indicates that the Bodner-Partom model shows relatively small mean stress drift when the plastic strain range is small, but becomes increasingly large when the plastic strain range becomes relatively large. The mean stress drift as a function of cycle number of both the Bodner-Partom and Walker model is compared with experimental data at relatively large plastic strains in Figure 4.26. The results indicate that both models predict mean stress relaxation in less than ten cycles, whereas the mean stresses are maintained in the experiment during the whole test period. It should be noted, however, that the mean cyclic stress in these strain cycles is small compared to the yield stress under the test conditions.

4.3.4 Stress Relaxation at Strain Hold

Strain holds were performed at various strain levels of hysteresis loops for 2 minutes to probe for the equilibrium stresses associated with cyclic deformation of B1900+Hf. Figure 4.27, which presents typical results of the equilibrium stress probe test at 760°C, indicates that stress relaxation occurs during strain hold but subsequent rapid hardening increases the stress

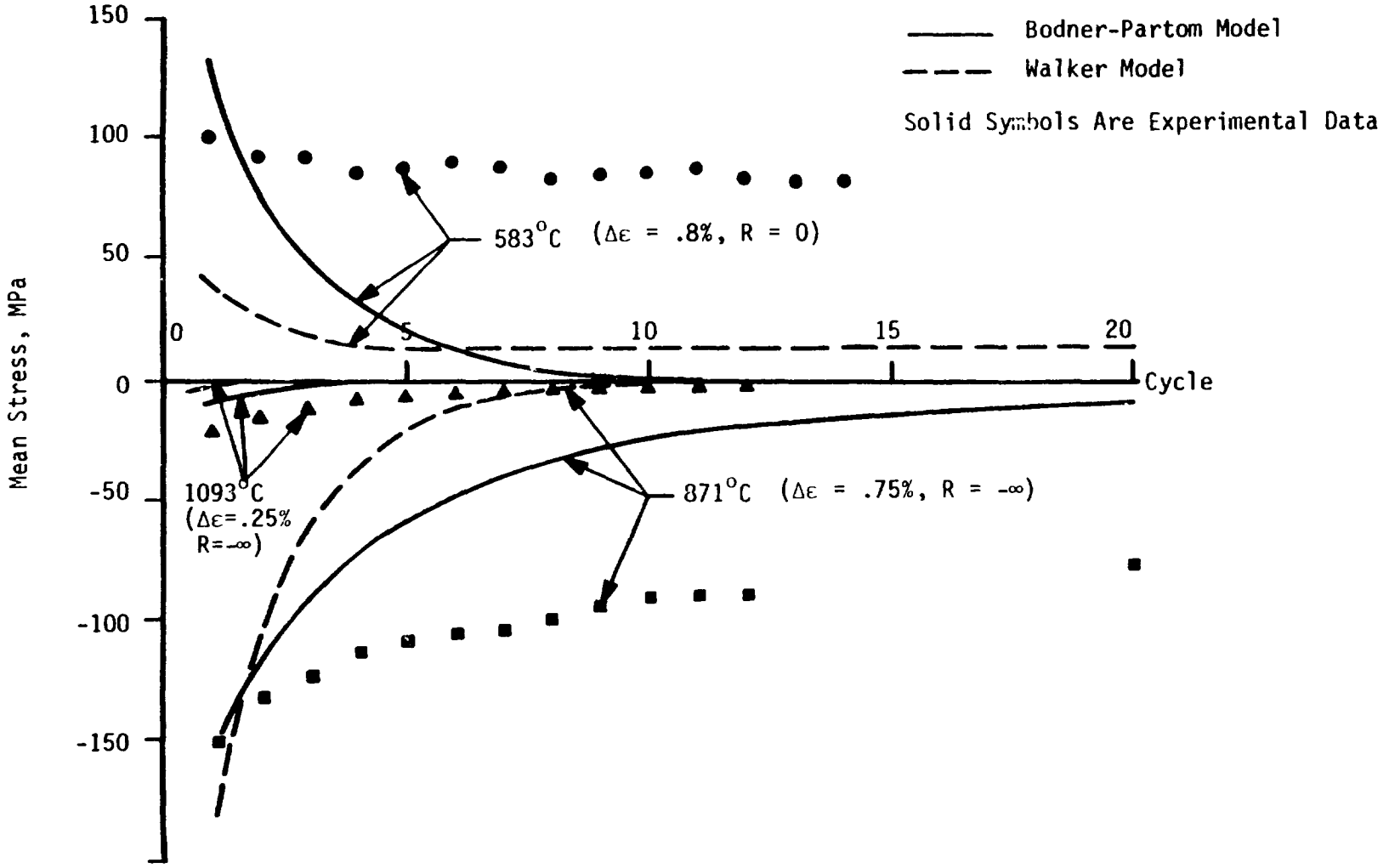

FIGURE 4.26. DRIFT OF MEAN STRESS AS FUNCTION OF CYCLE NUMBER.

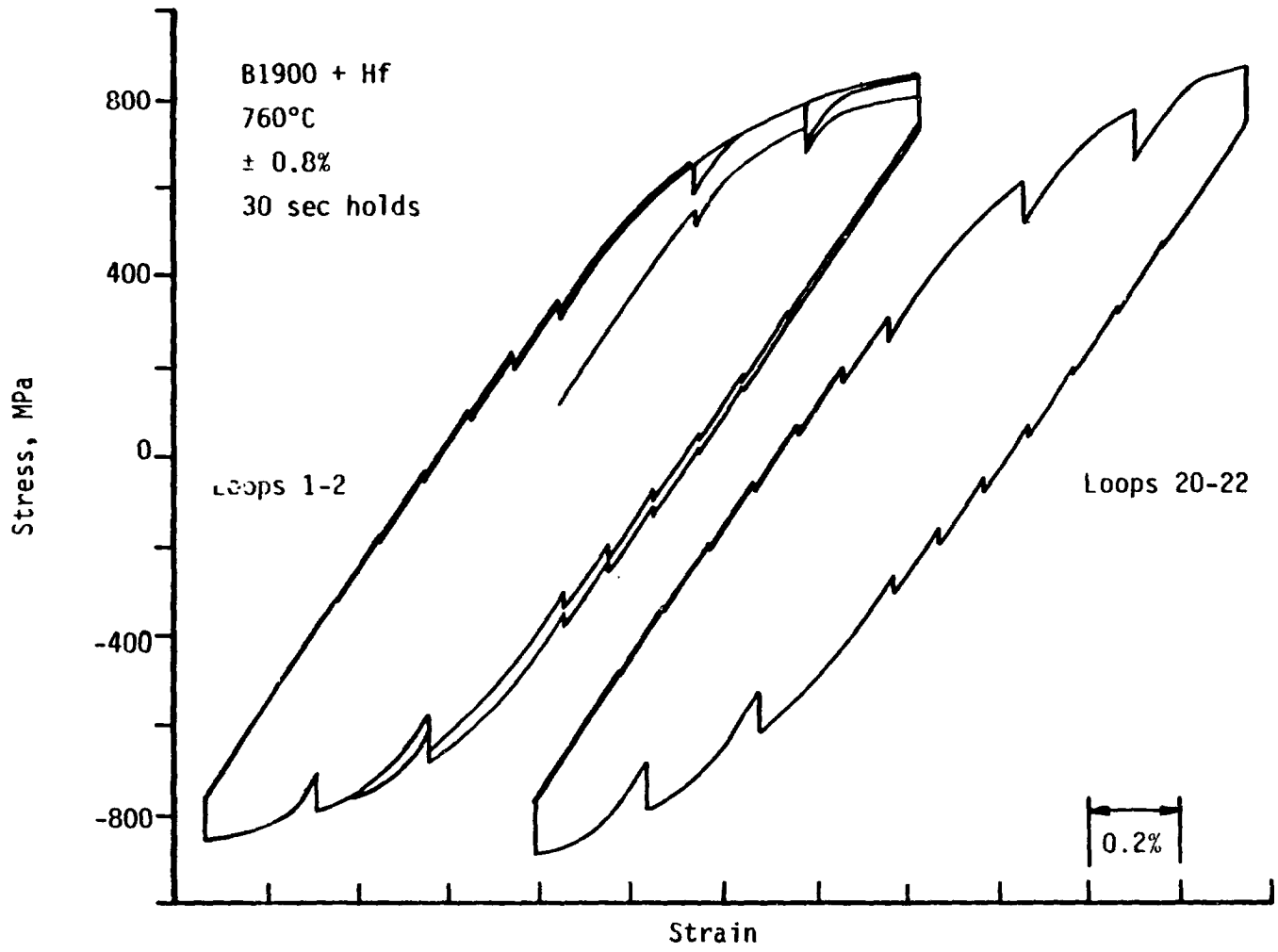

FIGURE 4.27. STRESS RELAXATION DURING STRAIN HOLD IN THE EQUILIBRIUM-STRESS PROBE TEST.

back to the previous value. Cyclic hardening is evidenced since the stress range of the first loop is less than that of the saturated loop which is the 22nd in this case. The stress ranges of the saturated loops with strain hold are compared with loops without strain hold in Figures 4.23 and 4.24. The comparison reveals no significant difference, indicating the stress ranges of the saturated loops with strain hold are not affected by the prior deformation history.

Stress relaxation data associated with holding at the peak strain of various saturated hysteresis loops are shown in Figures 4.28-4.29, together with the Bodner-Partom model predictions. In general, the agreement between theory and experiment is good for the three test temperatures which include 871, 982, and 1093°C. In some cases, the Bodner-Partom model overpredicts the peak stress of the saturated loop, but the overall trend of the stress relaxation behavior is predicted well.

Figure 4.30 compares the model prediction and experimental results of stress relaxation during strain hold on the unloading portion of the saturated hysteresis loop of B1900+Hf at 1093°C. The Bodner-Partom calculations agree well with the experimental data for strain holds at .6% and .55%. At .5%, the experimental result indicates reverse stress relaxation as the stress is slightly increased during hold period while the Bodner-Partom model predicts a constant stress with essentially no stress relaxation. In principle, the reverse stress relaxation process is capable of prediction by the equilibrium stress approach. However, no stress relaxation calculations are currently available for the Walker model.

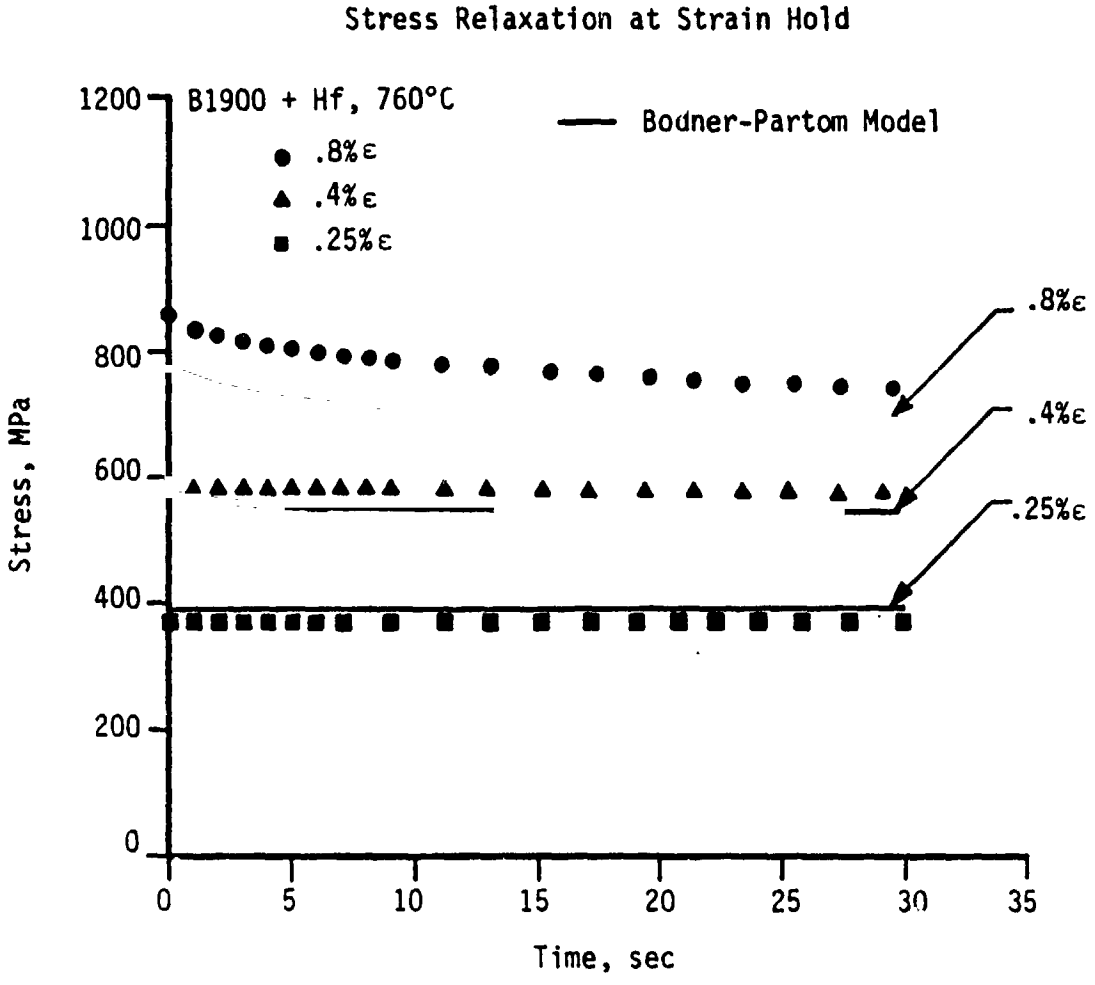

FIGURE 4.28. STRESS RELAXATION DATA COMPARED WITH BODNER-PARTOM MODEL PREDICTION AT 760°C.

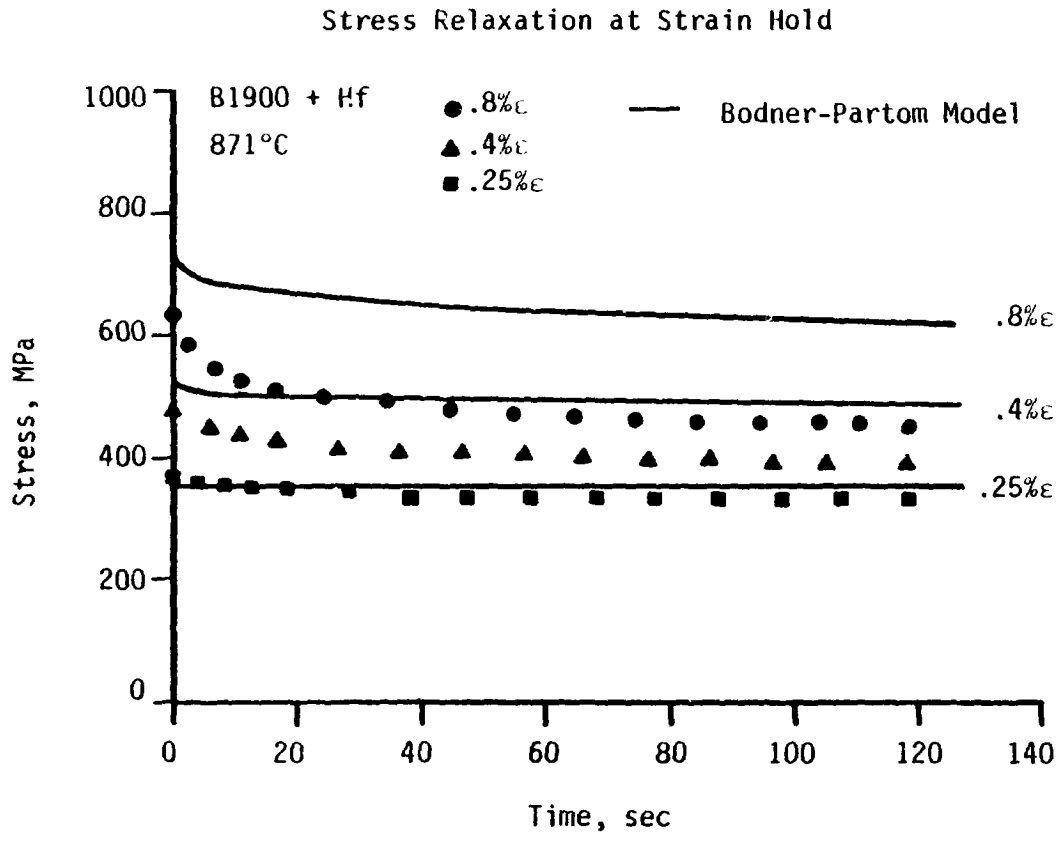

FIGURE 4.29. STRESS RELAXATION DATA COMPARED WITH BODNER-PARTOM MODEL PREDICTION AT 871°C.

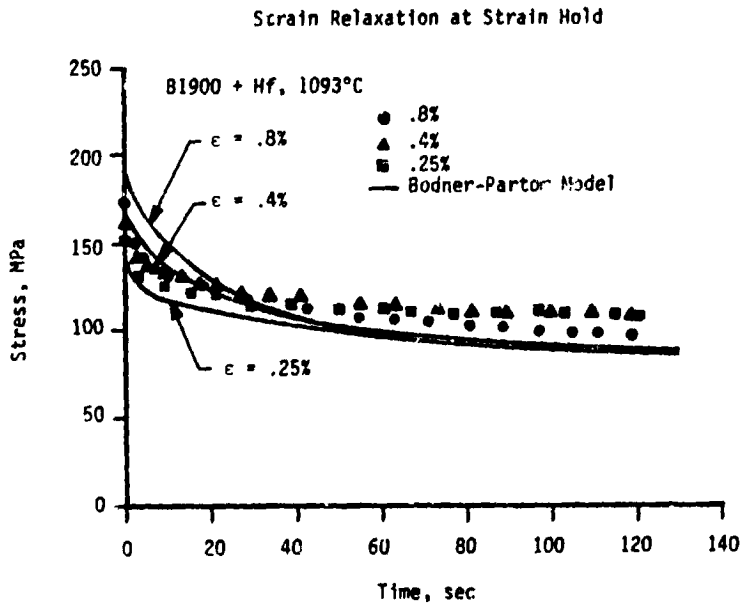

(a)

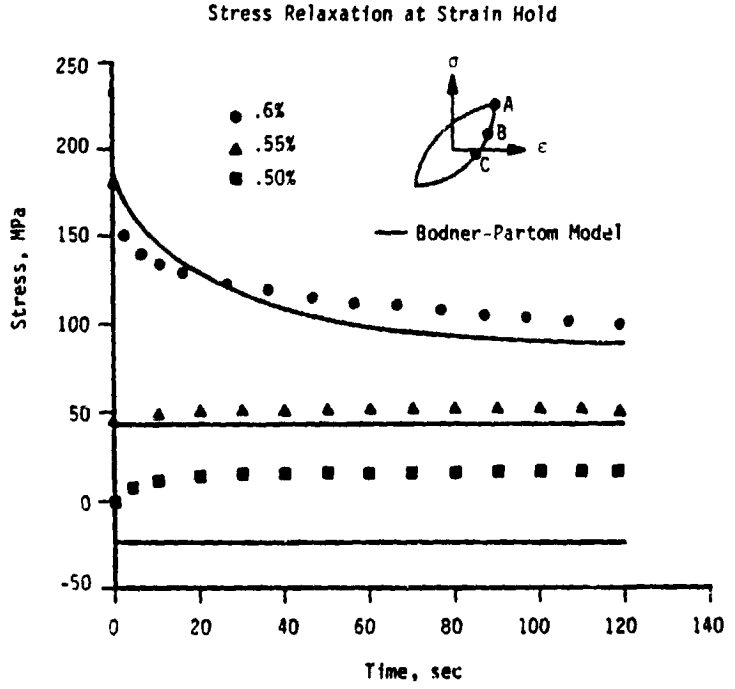

(b)

FIGURE 4.30. (A) STRESS RELAXATION DATA COMPARED WITH BODNER-PARTOM MODEL PREDICTIONS AT 1093°C AND (B) STRESS RELAXATION DATA AT THE UNLOADING BRANCH OF A HYSTERESIS LOOP COMPARED WITH BODNER-PARTOM MODEL PREDICTION AT 1093°C.

4.3.5 Dwell Fatigue Cyclic Behavior

Comparisons of dwell fatigue data with predicted behaviors are presented in Figures 4.31 to 4.33. A two minute hold at both the tension and compression load limits at 871°C produces significantly more deformation than is predicted by either theory, Figures 4.31. Walker's model tends to produce a better fit of the results, although neither can be judged to be adequate, particularly at the highest load level, +500 MPa. At 760°C, a two minute hold in tension at 350 MPa, Figure 4.32, results in a slight amount of cyclic plasticity. Walker's model overpredicts and the Bodner-Partom model underpredicts this quantity. At 550 MPa, both models overpredict the cyclic hysteresis loops. Neither the Walker nor the Bodner-Partom model is able to reproduce the cyclic response with a two minute hold in compression at 982°C, as shown in Figure 4.33.

4.3.6 Thermomechanical Fatigue (TMF) Cycling Constitutive Behavior

Comparisons of predicted and experimental TMF hysteresis loops are summarized in Figures 4.34-4.36. The three thermomechanical fatigue (TMF) loading cases were run with a sinusoidally varying mechanical strain and temperature with a cyclic period of sixty seconds. The strain for three of the tests varied from a nominal -0.4 percent to +0.4 percent, and the temperature varied sinusoidally from 538°C (1000°F) to 982°C (1800°F). For the first loading case (Cycle A) the temperature and strain varied in phase, i.e., the maximum temperature occurred at the same time as the maximum strain. For the second loading case (Cycle B) the temperature and strain loads were applied 180° out of phase, and in this case the maximum temperature coincided with the

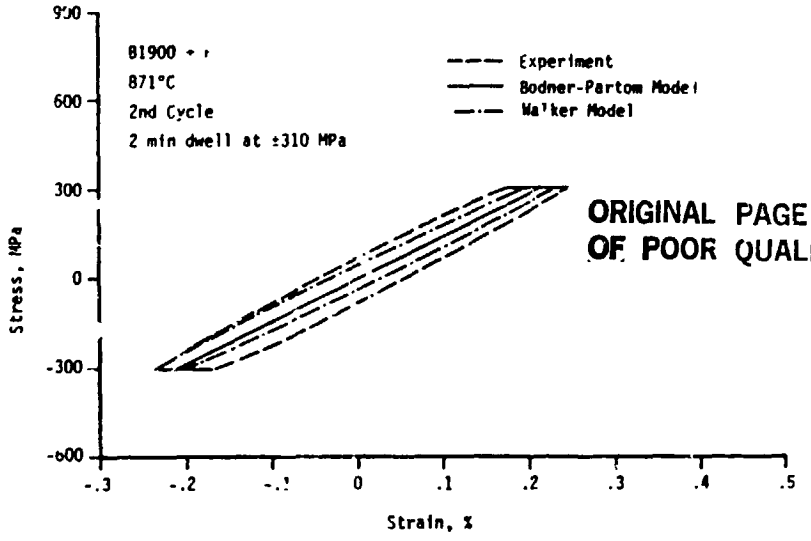

(a)

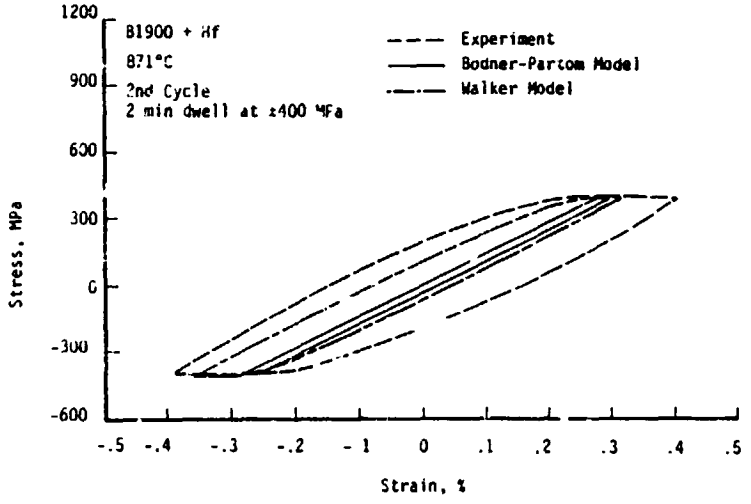

(b)

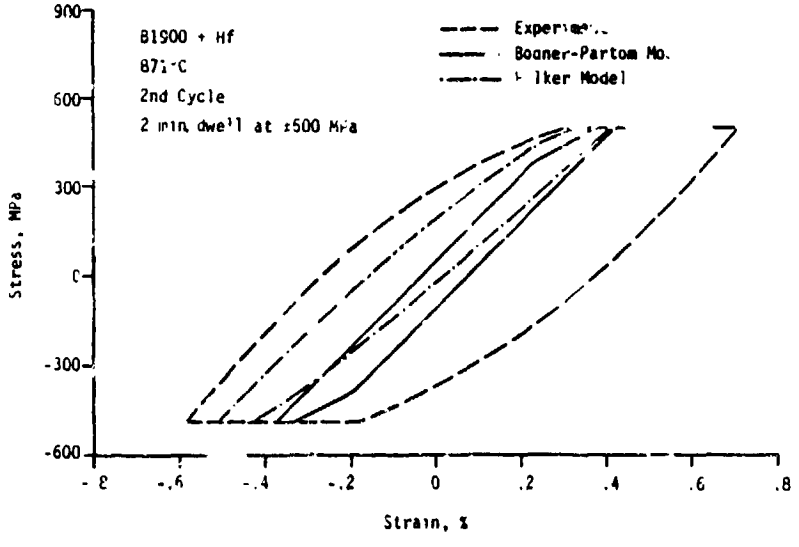

(c)

FIGURE 4.31. LOAD DWELL CYCLIC DATA COMPARED WITH THE WALKER AND THE BODNER-PARTOM MODEL PREDICTIONS AT 871°C.

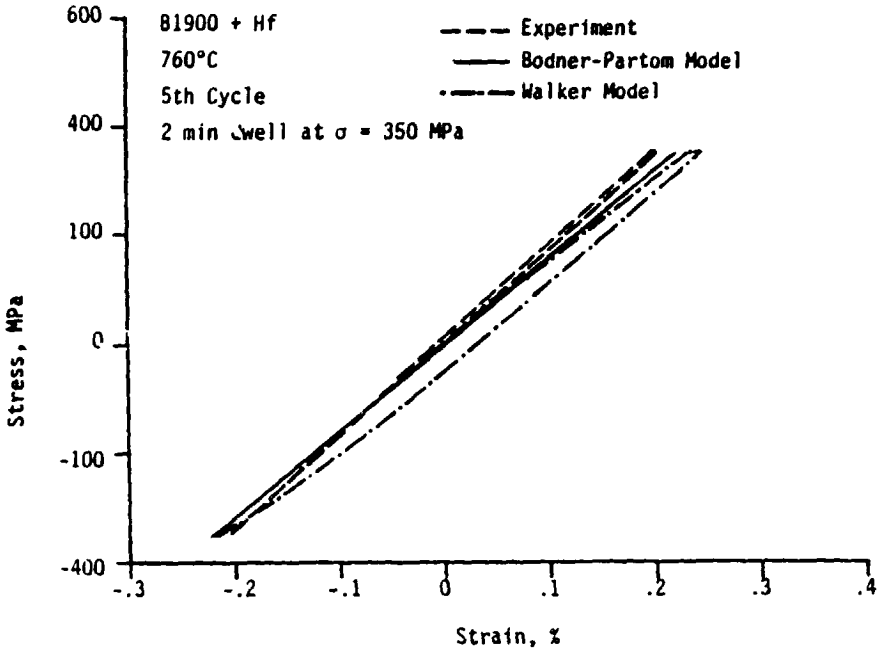

(a)

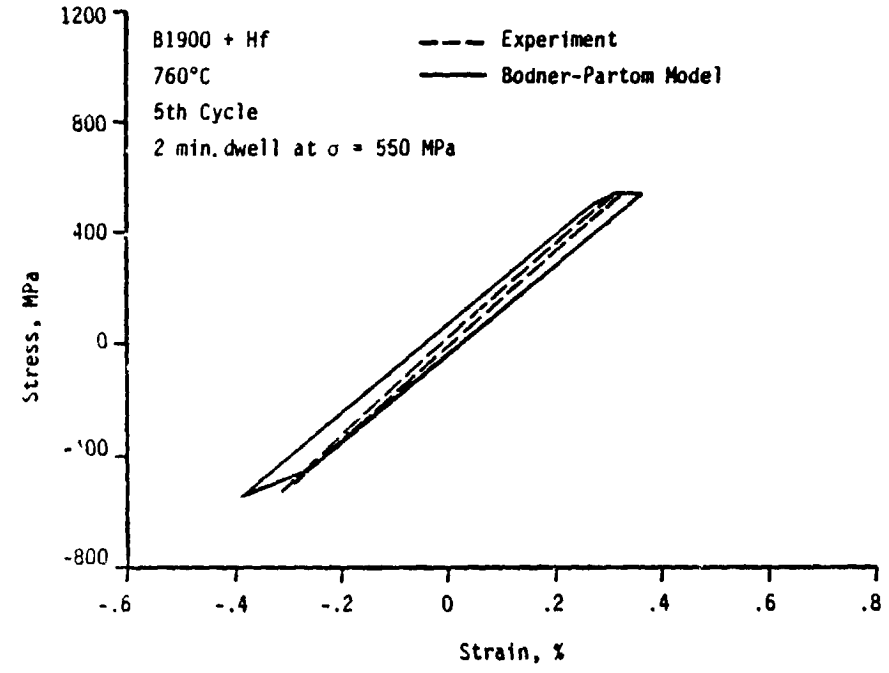

(b)

FIGURE 4.32. LOAD DWELL CYCLIC DATA COMPARED WITH THE WALKER AND THE BODNER-PARTOM MODEL PREDICTIONS AT 760°C.

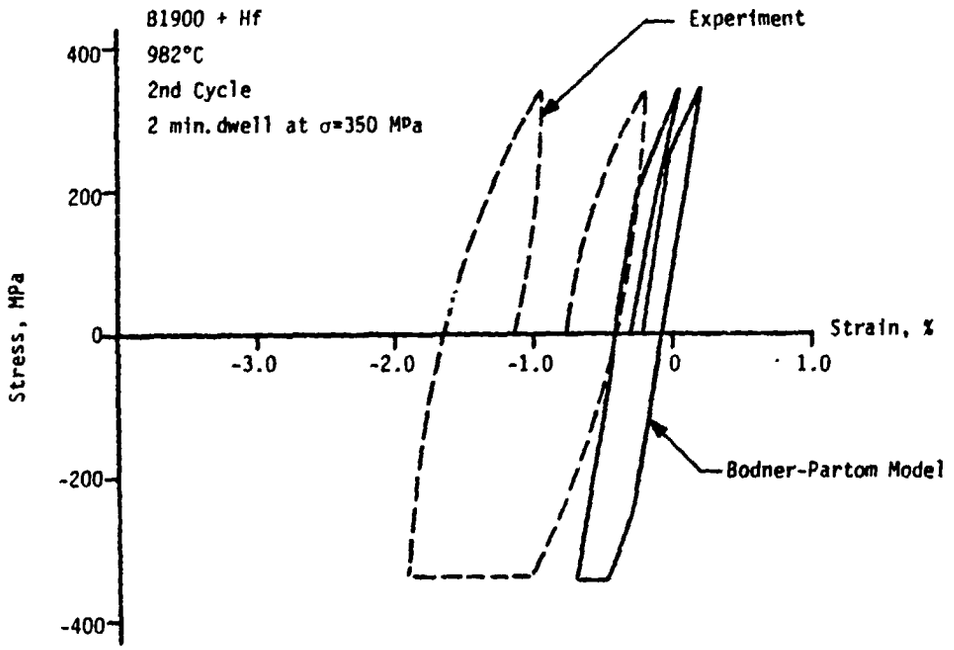

(a)

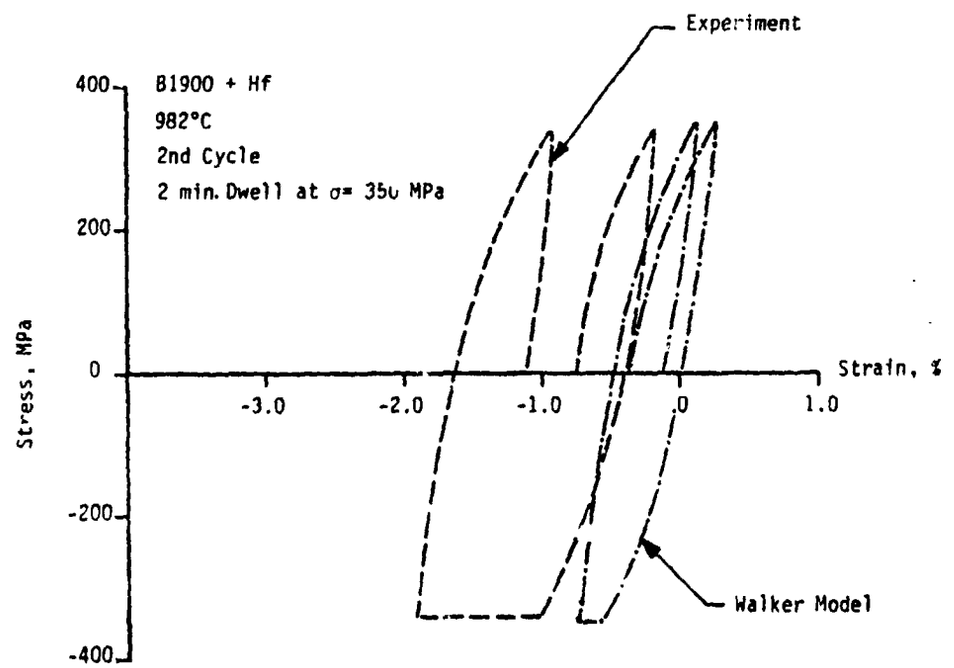

(b)

FIGURE 4.33. LOAD DWELL CYCLIC DATA COMPARED WITH THE WALKER AND THE BODNER-PARTOM MODEL PREDICTIONS AT 982°C (A) BODNER-PARTOM, (B) WALKER.

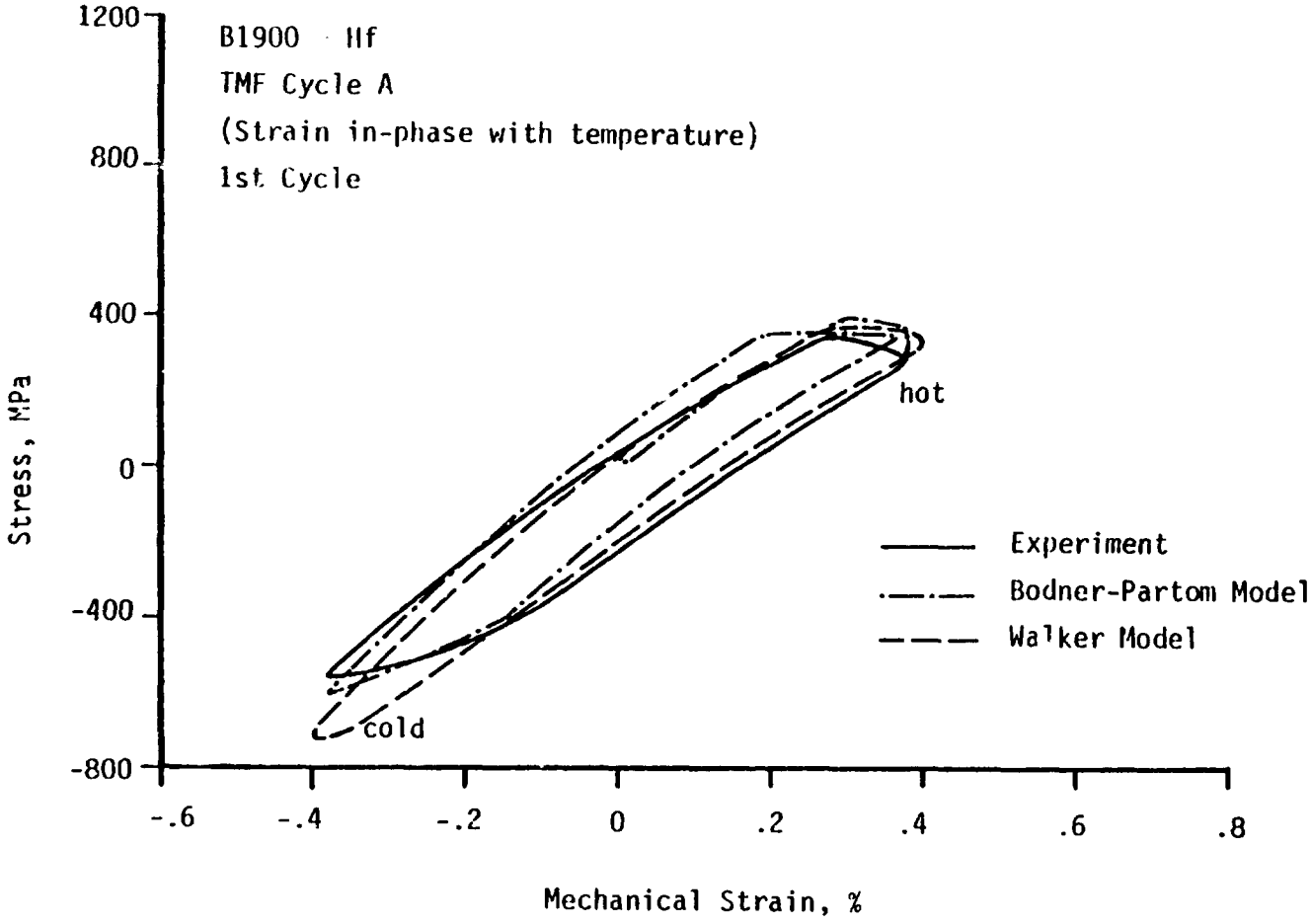

FIGURE 4.34. THERMOMECHANICAL CYCLIC DATA COMPARED WITH THE WALKER AND THE BODNER-PARTOM MODEL PREDICTIONS FOR THE IN-PHASE TMF CYCLE.

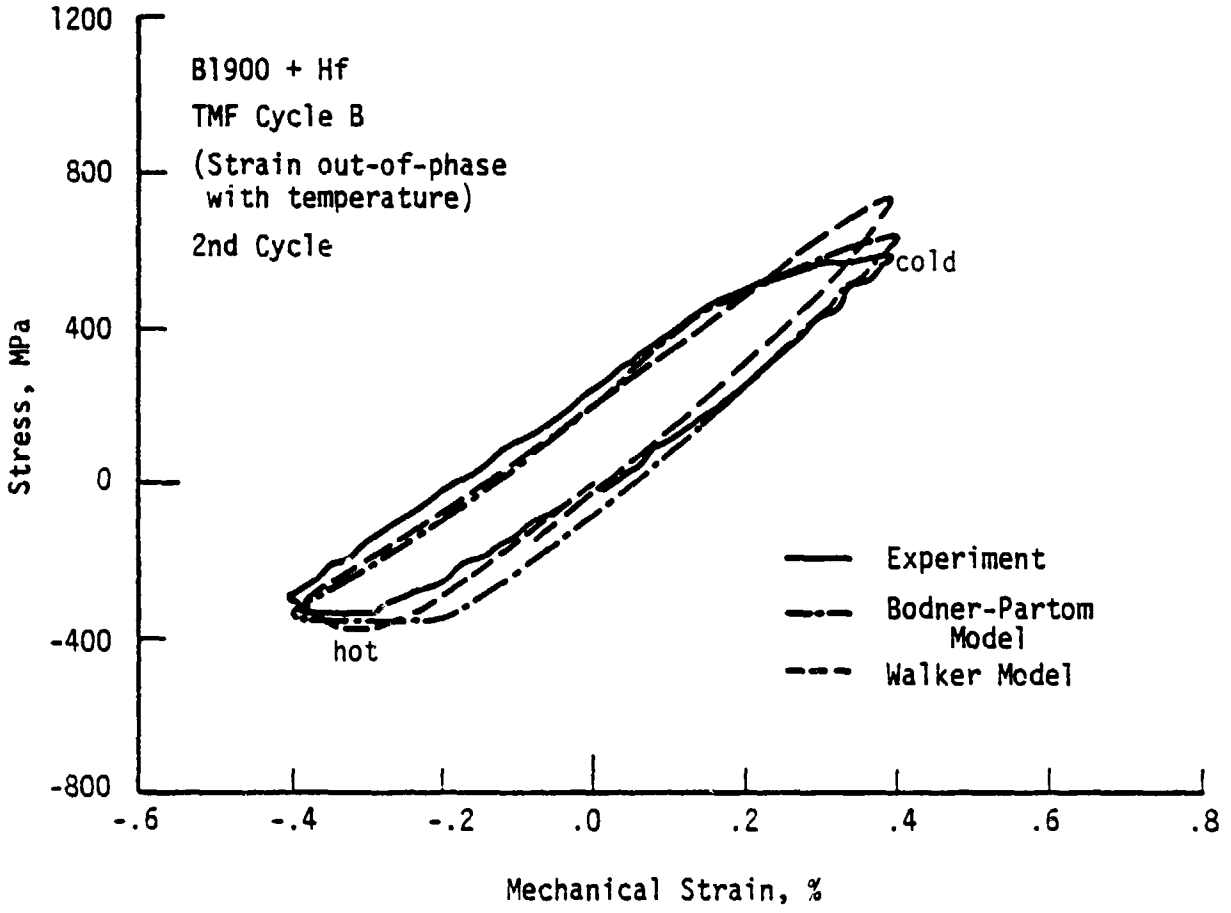

FIGURE 4.35. THERMOMECHANICAL CYCLIC DATA COMPARED WITH THE WALKER AND THE BODNER-PARTOM MODEL PREDICTION FOR THE OUT-OF-PHASE TMF CYCLE.

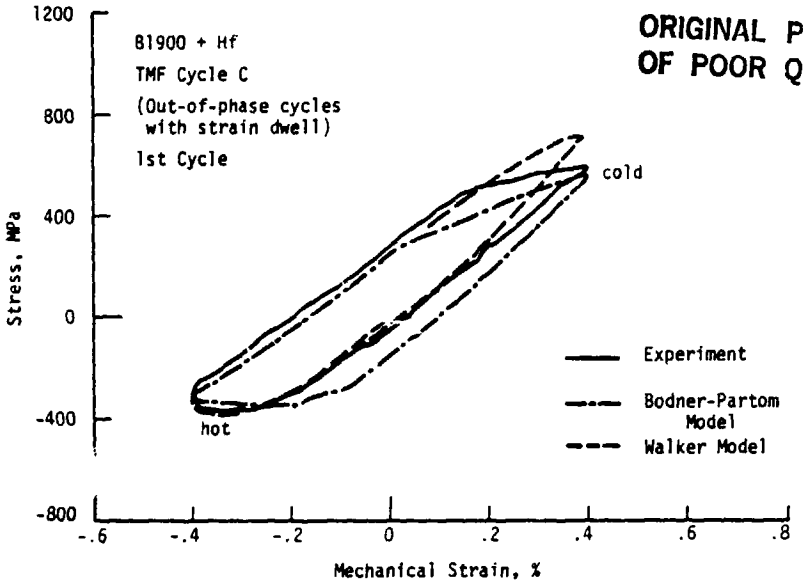

(a)

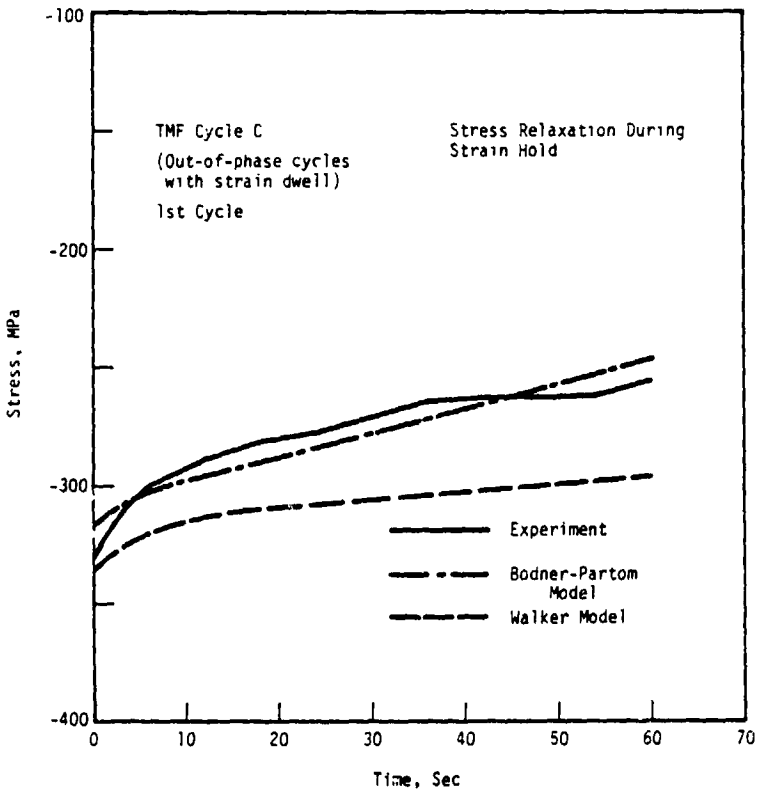

(b)

FIGURE 4.36. THERMOMECHANICAL DATA COMPARED WITH THE WALKER AND THE BODNER-PARTOM MODEL PREDICTIONS FOR THE OUT-OF-PHASE TMF CYCLE WITH STRAIN HOLD: (A) STRESS-STRAIN RESPONSE DURING OUT-OF-PHASE CYCLE, (B) STRESS RELAXATION RESPONSE DURING STRAIN HOLD.

minimum strain. The third loading case (Cycle C) was a repeat of the second, but with the addition of a sixty second constant strain hold at -0.4 percent strain.

The Walker model calculations were performed in conjunction with the MARC finite element deck. The structural model used was a four element axi-symmetric shell model using MARC element number 10, a four model quadrilateral ring element. The Walker model results show consistently good correlation at the hot temperature end of the load cycle for all three TMF missions analyzed. There is, however, a consistent stress overshoot at the cold (1000°F) end of the simulation. The Bodner-Partom model calculations, performed at SwRI, are in reasonably good agreement with experimental data in all aspects with the exception that the width of the TMF loop in Cycle C is larger than that observed experimentally. The stress relaxation which accompanied strain hold in cycle C is well predicted by the Bodner-Partom model as shown in Figure 4.36(b).

5.0 MULTIAXIAL EVALUATION OF CONSTITUTIVE MODELS

Combined tension and torsion tests were conducted to investigate the effects of principal stress ratio, temperature, and loading sequence on the inelastic elevated temperature multiaxial behavior of the base alloy, B1900+Hf. Both proportional and non-proportional loading paths were examined, some of which involved stress relaxation under strain hold. The various tension/torsion experiments were designed to examine: (1) the presence or absence of additional hardening under non-proportional (90° out-of-phase) loading paths, (2) the nature of this additional hardening, if present, (3) the non-axiality between the plastic strain rate and the deviatoric stress vectors, and (4) the direction of stress relaxation during strain hold.

A considerable amount of multiaxial data have been generated in this program which has not yet been completely analyzed. Correlation between theory and experiment in this report will be directed toward examining the influence of nonproportional loading path on the multiaxial hardening behavior of B1900+Hf. The results on the effects of loading path on the phase angle between the plastic strain and deviatoric stress vectors and the direction of stress relaxation will be reported at a later date.

5.1 Experimental Procedures

Multiaxial tension/torsion tests were performed on a servo-controlled, hydraulic biaxial machine with two independent feedback loops. Axial and torsional strains were independently controlled. The load capacities of the test facility are 44,000 N axial load and 425 N-M torque. A closeup view of the experimental setup is shown in Figure 5.1. Elevated temperature was provided

by induction heating. The biaxial test specimen is shown in Figure 4.3 together with the isothermal cyclic and the thermomechanical specimens. A schematic of the geometry of the biaxial test specimen can be found in Figure 4.2

Axial and torsional strains were measured using a high temperature, biaxial (tension/torsion) capacitance extensometer as shown in Figure 5.2. The extensometer was water cooled and mounted internally to the specimen and grip. The coaxial roto-stator configuration of the capacitance sensing plates avoids the need for flexural elements in the systems and eliminates cross-talk. The capacitance system is of high sensitivity (6×10^{-6} radian and 2 $\mu\varepsilon$) and moderate dynamic range ($\dot{\varepsilon} \leq .1$ sec^{-1}).

The various multiaxial tension/torsion constitutive tests are illustrated in Figure 5.3. These tests include: (1) uniaxial loading, (2) proportional combined loading, (3) nonproportional loading, and (4) nonproportional loading with strain hold.

Tests 1 through 4 involved incremental step strain tests in either torsion or tension at two temperatures, 649 and 982°F. These temperatures were selected to correspond to idle and takeoff temperature conditions in an air-cooled turbine vane.

Tests 7 through 10 involved incremental cyclic step strain tests in combined tension/torsion for at least two shear to extensional strain ratios at each temperature. The effective strain rates in these tests are approximately 4×10^{-4} sec^{-1}.

Tests 5, 6, 11 and 12 were combined tension/torsion tests conducted under 90° out-of-phase strain cycling. The frequencies were adjusted for each

FIGURE 5.1. BIAXIAL SPECIMEN UNDER TEST AT 982°C.

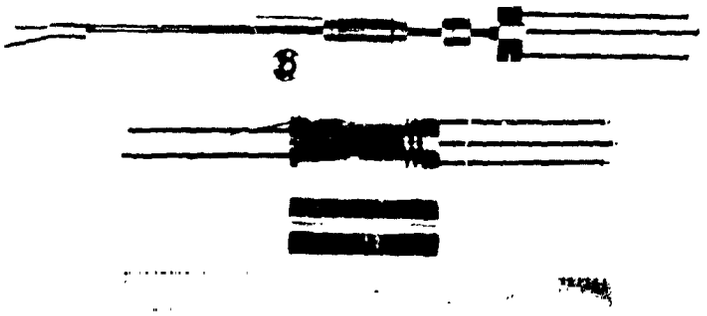

(a) Rotor (upper), stator (middle) and housing (lower).

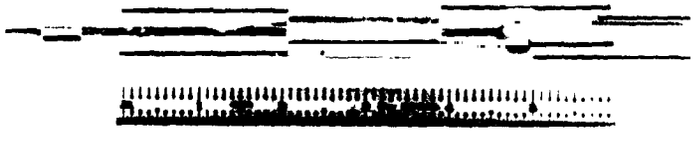

(b) Assembled transducer.

FIGURE 5.2. BIAXIAL TENSION/TORSION CAPACITANCE EXTENSOMETER.

Proportional Paths

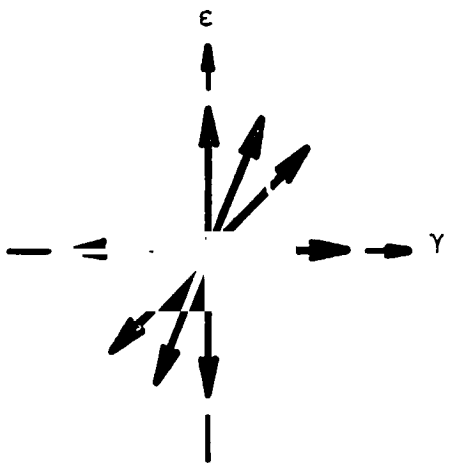

90° out-of-phase

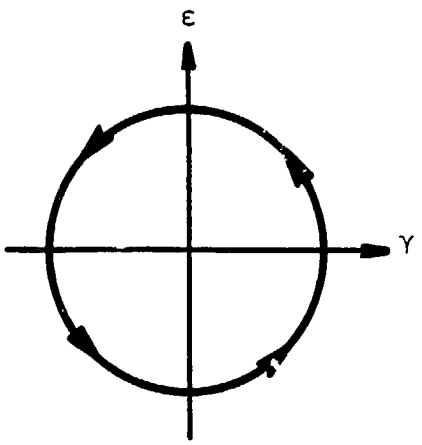

90° out-of-phase followed by proportional paths

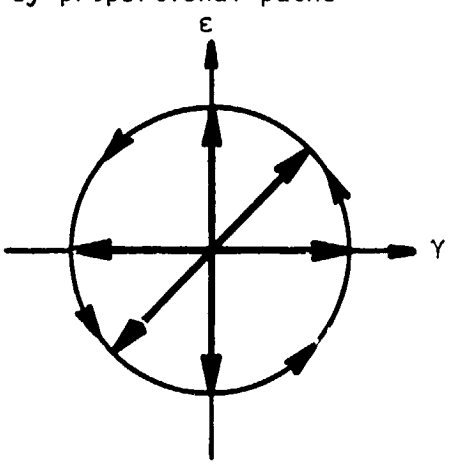

Double Frequency

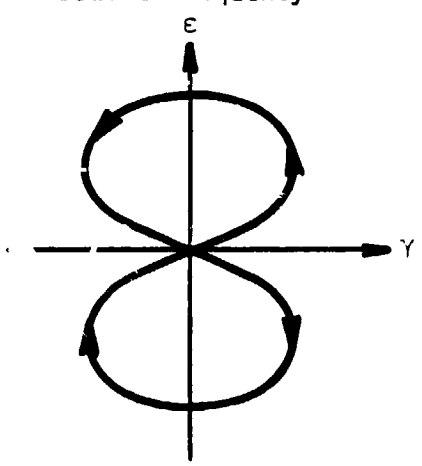

FIGURE 5.3 THE PROPORTIONAL AND NONPROPORTIONAL STRAIN PATHS UTILIZED IN THE BIAXIAL TESTS.

effective strain range so that effective strain rate was approximately constant. In tests 13 and 14 the shear strain frequency doubled the axial frequency. In tests 15 and 16, the specimens were cycled 90° out-of-phase until saturation. A two minute strain hold was then applied at each of the strain peaks. After strain hold, the specimens were strained under proportional loading and the strain hold cycle was repeated. Tests 17 and 18 were similar to tests 15 and 16, except strain hold cycling was not applied. All the above tests were conducted at either 649°C or 982°C. Test 19 was a 90° out-of-phase nonproportional loading experiment at 871°C in which the out-of-phase loading was followed by in-phase loading with various strain ratio.

5.2 Comparison of Theoretical and Experimental Results

5.2.1 Proportional Loading Paths

An effective stress range and an effective plastic range based on the van Mises criterion were used for correlating the multiaxial tension-torsion cyclic data. The effective stress range, $\Delta\sigma_{eff}$, and the effective plastic strain range are obtained as follow:

$$\frac{\Delta\sigma_{eff}}{2} = \left[\left(\frac{\Delta\sigma}{2}\right)^2 + 3\left(\frac{\Delta\tau}{2}\right)^2 \right]^{1/2} \qquad (5.1)$$

and

$$\frac{\Delta\varepsilon^p_{eff}}{2} = \left[\left(\frac{\Delta\varepsilon^p}{2}\right)^2 + \frac{1}{3}\left(\frac{\Delta\gamma^p}{2}\right)^2 \right]^{1/2} \qquad (5.2)$$

where $\Delta\sigma$ and $\Delta\tau$ are the axial stress and shear stress ranges, respectively. $\Delta\varepsilon^p$ and $\Delta\gamma^p$ are the corresponding plastic components of the axial and shear strain ranges. All the in-phase multiaxial cyclic data are summarized in Figure 5.4 by plotting half of the effective stress range against half of the

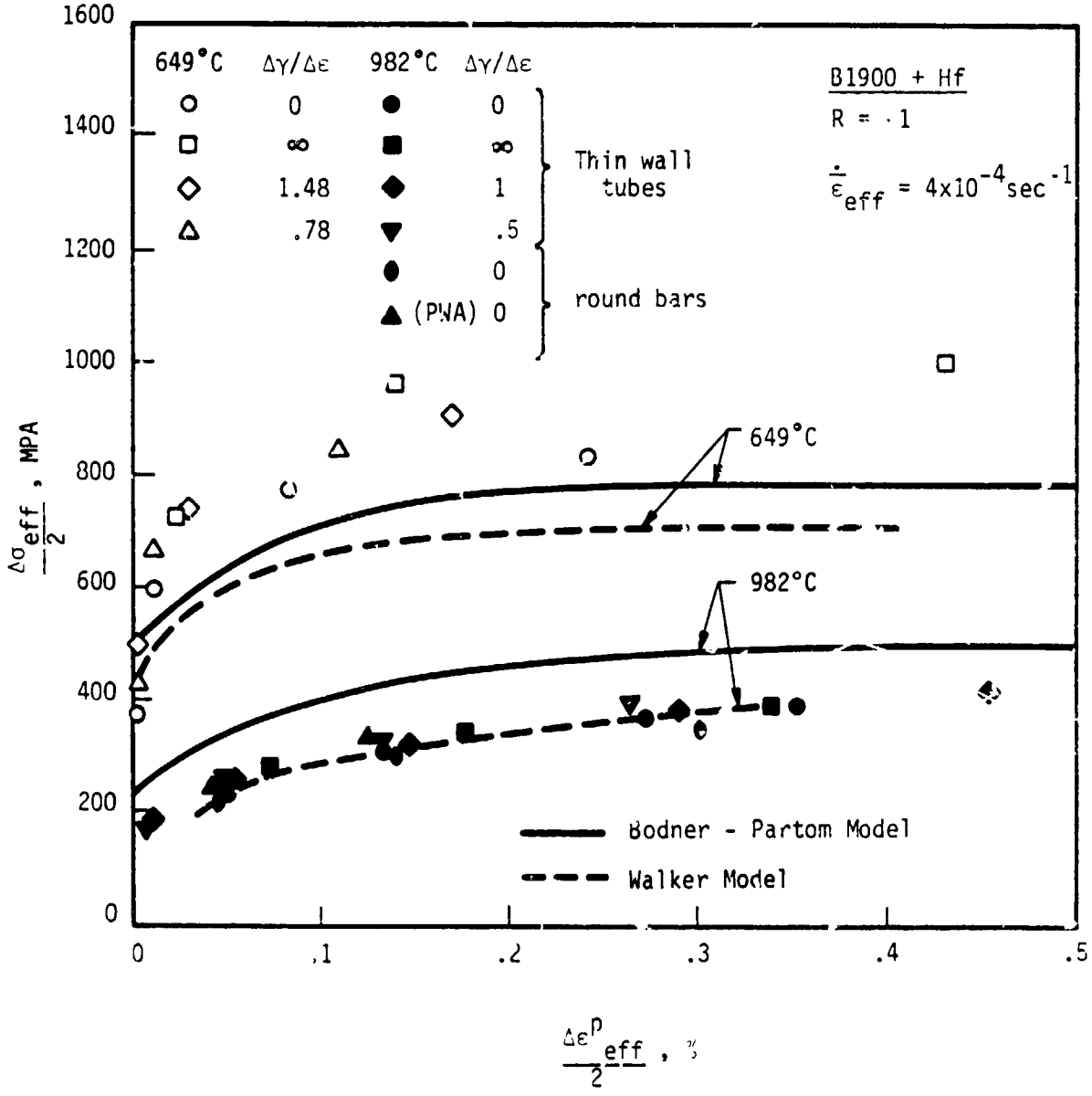

FIGURE 5.4. PROPORTIONAL MULTIAXIAL DATA COMPARED WITH MODEL PREDICTIONS.

effective plastic strain range. Note that all the multiaxial data obtained at 982°C form one small scatter band. On the other hand, the J_2-based effective stress and plastic strain ranges are not able to correlate the 649°C data. Specifically, the shear stress range is higher than the axial stress range at an equivalent effective plastic stress range. The implication is that J_2 might not be the appropriate criterion for B1900+Hf at 649°C.

Both the Bodner-Partom and Walker models are J_2-based theories and, therefore, predict the same effective stress range-effective plastic strain range curve, regardless of the applied $\Delta\gamma/\Delta\varepsilon$ ratios. Correlations of Bodner-Partom model calculations and experiment, however, reveal that the overall agreement with the proportional biaxial data is only fair. At 982°C, the Bodner-Partom model overpredicts the effective stress range at a given effective plastic strain range. The overprediction is consistent with the uniaxial cyclic calculations shown in Figure 4.21. The Bodner-Partom model is in fair agreement with the axial data at 649°C, but is rather poor with the torsional data. The Walker model overpredicts the plastic strain range and underpredicts the stress range so that the predicted cyclic stress strain curve falls below and to the right of the data at 649°C (1200°F). The agreement between Walker's model prediction and data at 982°C (1800°F) is excellent. The poor agreement between prediction and test at 649°C (1200 F) can be attributed in large part to limited test data at 649°C from which model constants were derived (a single tensile test) and differences in material properties between the round bar specimens and the tube specimens used for the biaxial testing.

C-2

5.2.2 Non-Proportional Loading Paths

Comparison of the multiaxial data obtained from 90° out-of-phase loading paths with those from in-phase loadings reveals no additional hardening under non-proportional loading paths (Figures 5.5 - 5.7). In Figure 5.5, the solid line represents the stress locus of the B1900+Hf specimen tested at $\varepsilon_{eff} = \pm .4\%$ under 90° out-of-phase until cyclic saturation. The experimental stress locus is seen to coincide with data points which corresponds to the stress ranges obtained from in-phase loadings at various strain paths at an equivalent effective strain rate and effective strain range. This finding of no additional hardening under nonproportional loading paths was confirmed by the combined nonproportional/proportional test in which the specimen was cycled 90° out-of-phase until saturation and then was cycled in-phase, the resulting peak stresses; σ and τ, lie on the same σ-τ locus obtained under the 90° out-of-phase condition, as shown in Figure 5.5. The absence of nonproportional hardening is also observed in B1900+Hf specimen cycled at $\varepsilon_{eff} = \pm .6\%$ at 649°C (Figure 5.6) and in specimen cycled at $\varepsilon_{eff} = \pm .4\%$ at 982°C (Figure 5.7), and in specimen tested at 871°C.

The Bodner-Partom model without the nonproportional hardening term, i.e., setting $\alpha_1 = 0$ so that $\dot{\alpha} \equiv 0$, was used to correlate all the 90° out-of-phase multiaxial data. Similarly, the Walker model without the nonproportional hardening term K_3 was used for this data correlation. As in the case of correlation with the in-phase data, the Bodner-Partom calculations in general are in good agreement with experimental data at 649°C when cycling at low effective strain levels ($\varepsilon_{eff} = \pm .4\%$ or less), but underpredict the shear stress when cycling at $\varepsilon_{eff} = \pm .6\%$. On the other hand, the Bodner-Partom model tends to overpredict the stresses at 982°C. The Walker model shows good

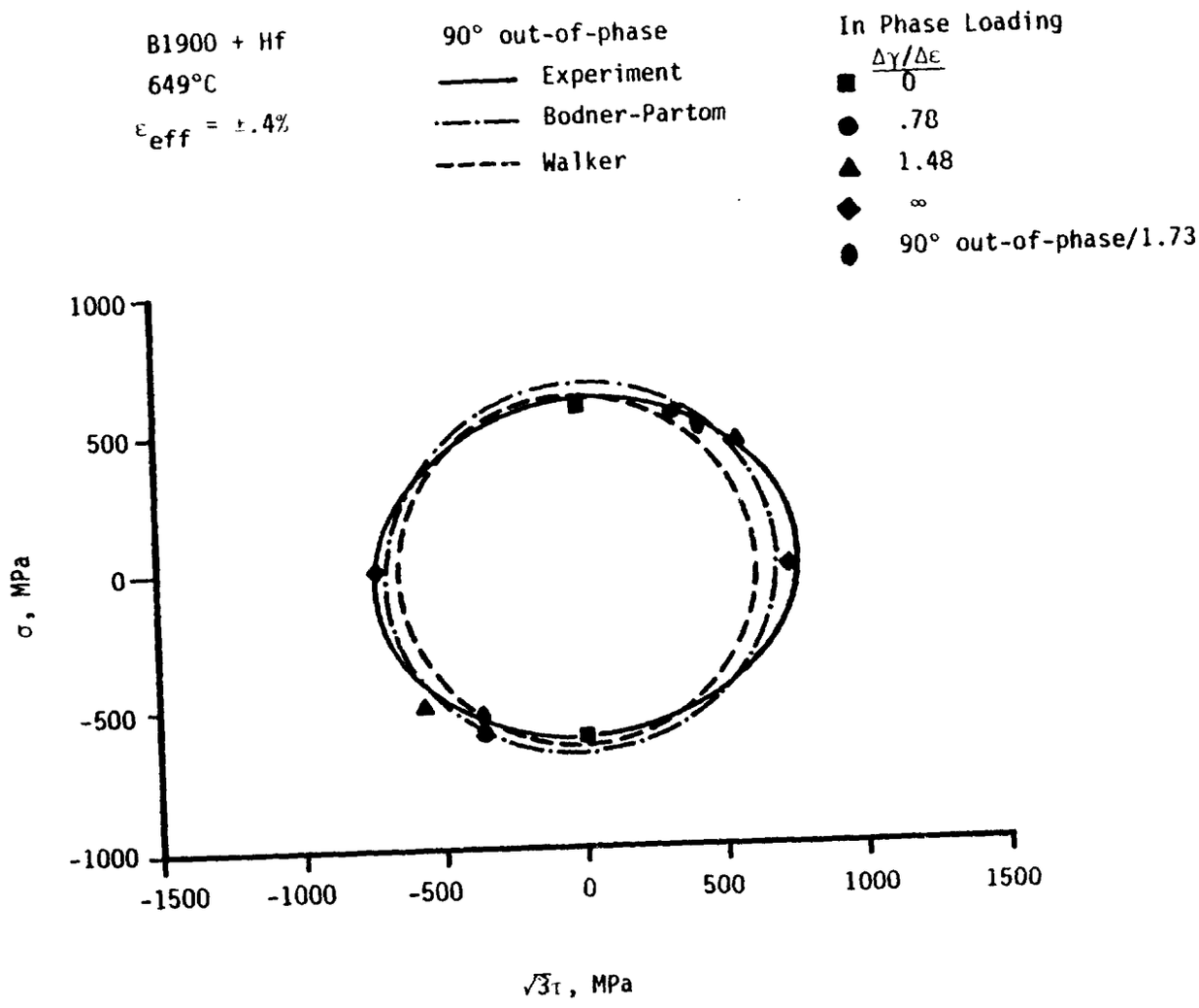

FIGURE 5.5. COMPARISON OF PROPORTIONAL AND 90° OUT-OF-PHASE MULTIAXIAL DATA WITH MODEL PREDICTIONS FOR ε_{eff} = ± .4% AT 649°C.

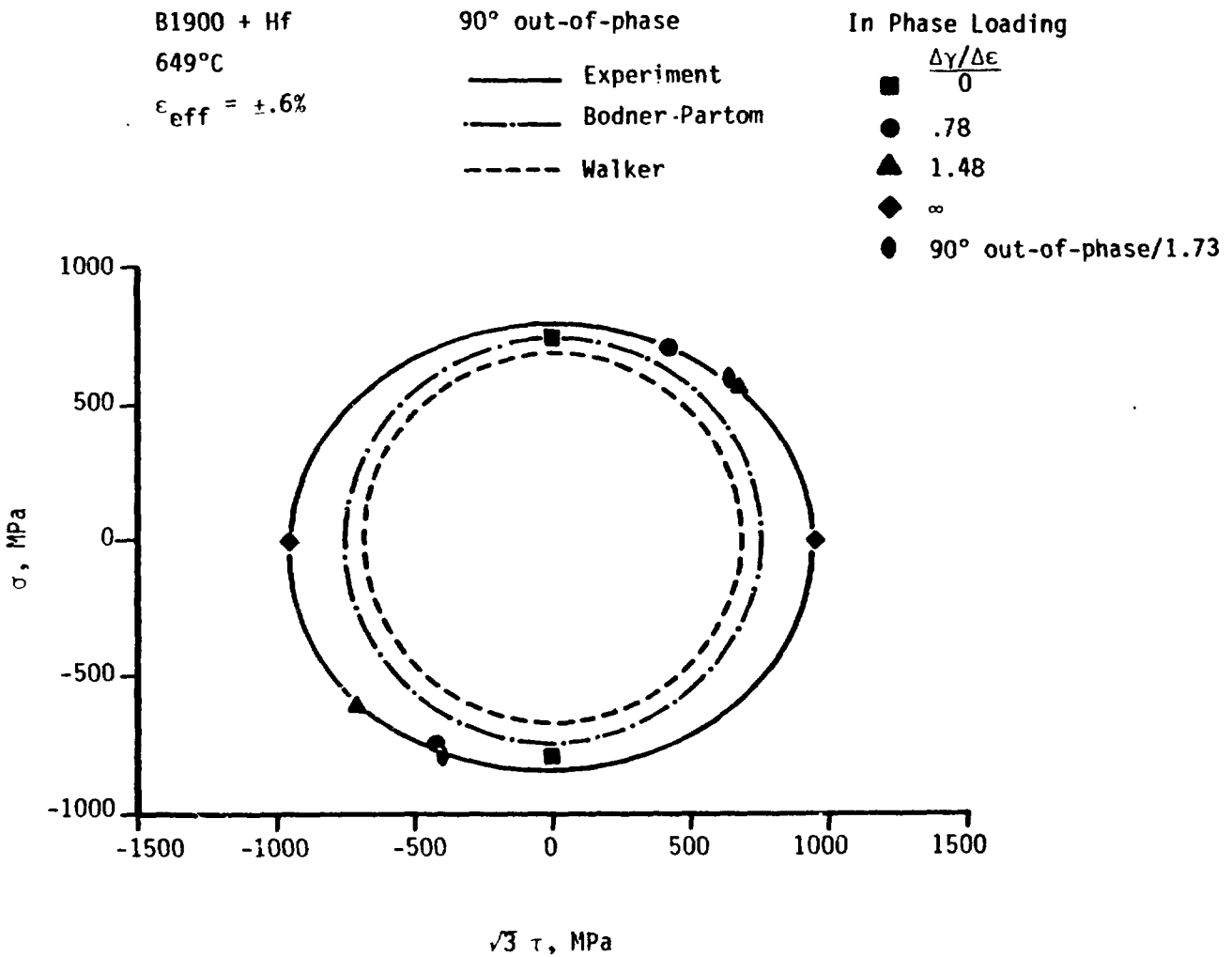

FIGURE 5.6. COMPARISON OF THE PROPORTIONAL AND 90° OUT-OF-PHASE MULTIAXIAL DATA WITH MODEL PREDICTIONS AT ε_{eff} = ± 0.6% AT 649°C.

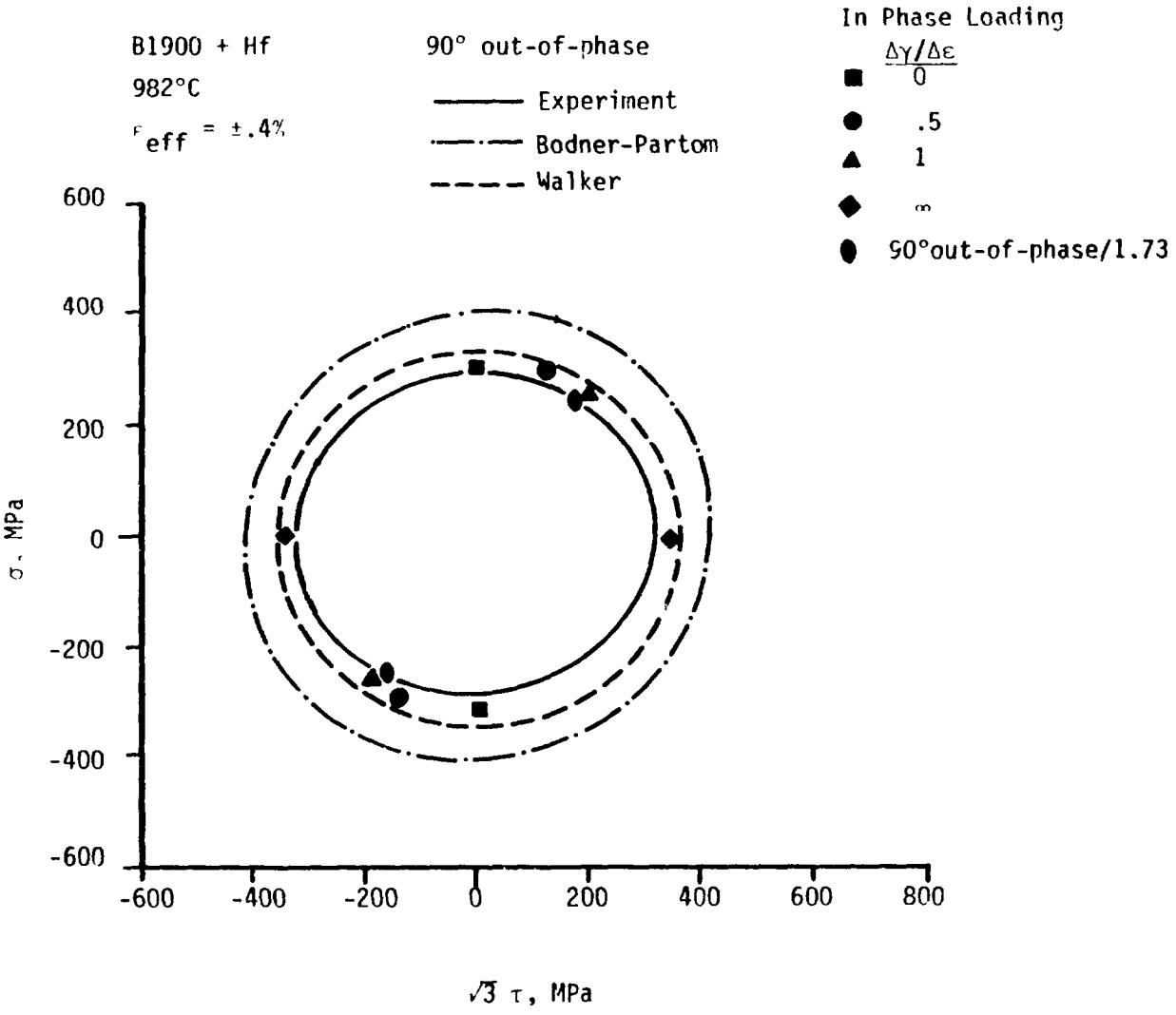

FIGURE 5.7. COMPARISON OF THE PROPORTIONAL AND 90°C OUT-OF-PHASE MULTIAXIAL DATA WITH MODEL PREDICTIONS AT ε_{eff} = ± .4% AT 982°C.

agreement with the axial stress at low effective strain levels (Figure 5.5), but underpredicts the shear stresses at 649°C (1200°F) as shown in Figures 5.5 and 5.6. The agreement between prediction and experiment at 982°C (1800°F) is quite good for Walker's model. Comparisons of the calculated and experimental saturated hysteresis loops of various strain ranges at 649 and 982°C are shown in Figures 5.8 and 5.9, respectively. The predicted hysteresis loops are generally somewhat larger than those observed experimentally. In Figures 5.8 and 5.9, the Walker model predictions for the saturated hystersis loops are larger than experiment at 649°C (1200°F), but show good agreement with experiment at 982°C (1800°F).

The Bodner-Partom model predicts the frequency effect on the multiaxial cyclic data of B1900+Hf under 90° out-of-phase straining rather well, as demonstrated in Figure 5.10 and Figure 5.11. The Walker model predicts the frequency effect well at 982°C but somewhat overpredicts at 649°C. For nonproportional loading involving shear strain frequency double that for axial strain, the Bodner-Partom and Walker calculations also compare favorably with the experimental data. Figure 5.12 shows that the stresses of the calculated hysteresis loops for $\varepsilon_{eff} = \pm .4\%$ at 649°C are in fair agreement with the experimental loops, but the width of the loops tend to be larger than observed.

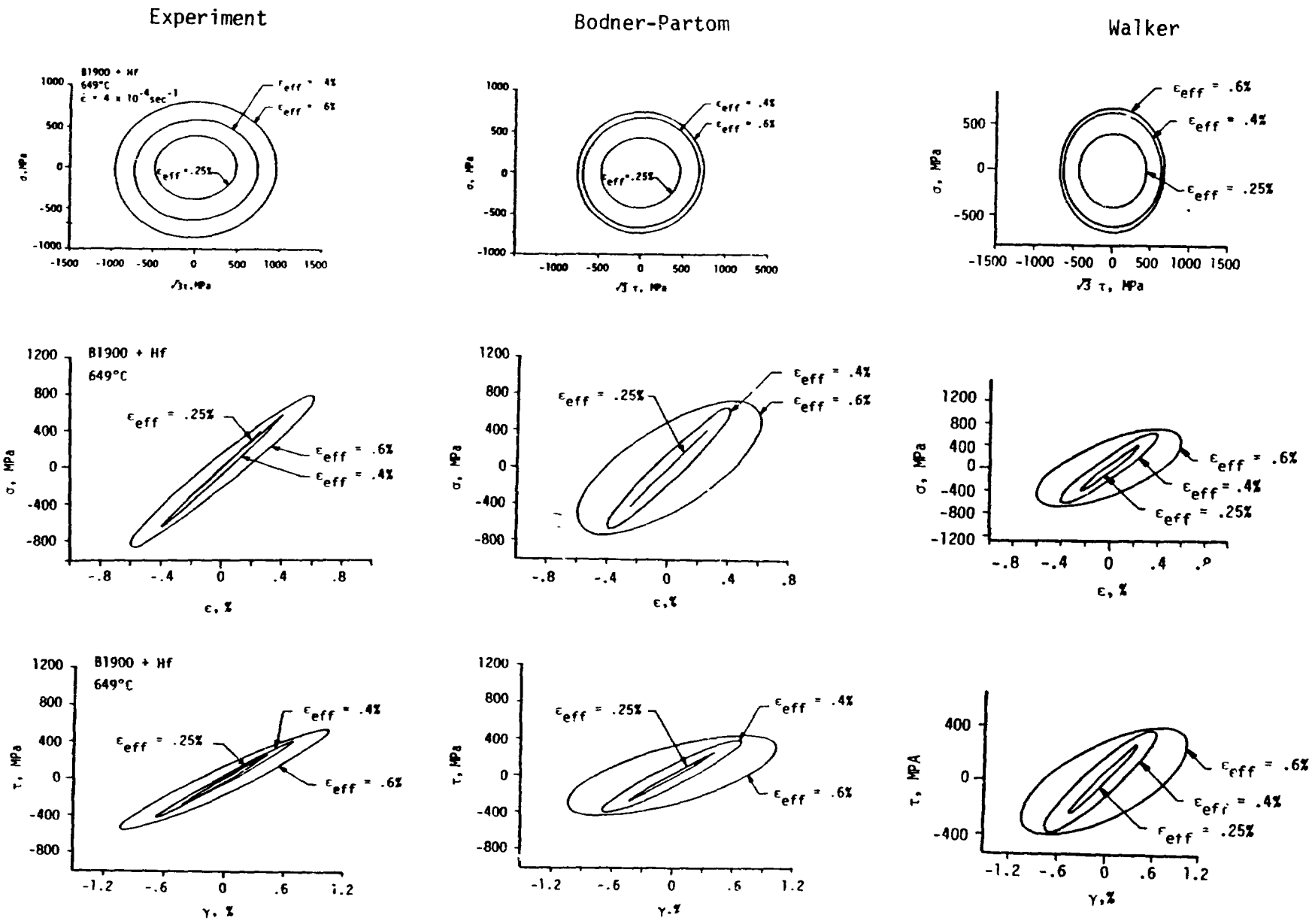

FIGURE 5.8. COMPARISON OF EXPERIMENTAL DATA AND MODEL CALCULATIONS OF B1900+Hf SUBJECTED TO 90° OUT-OF-PHASE LOADING AT THREE EFFECTIVE STRAIN LEVELS AT 649°C.

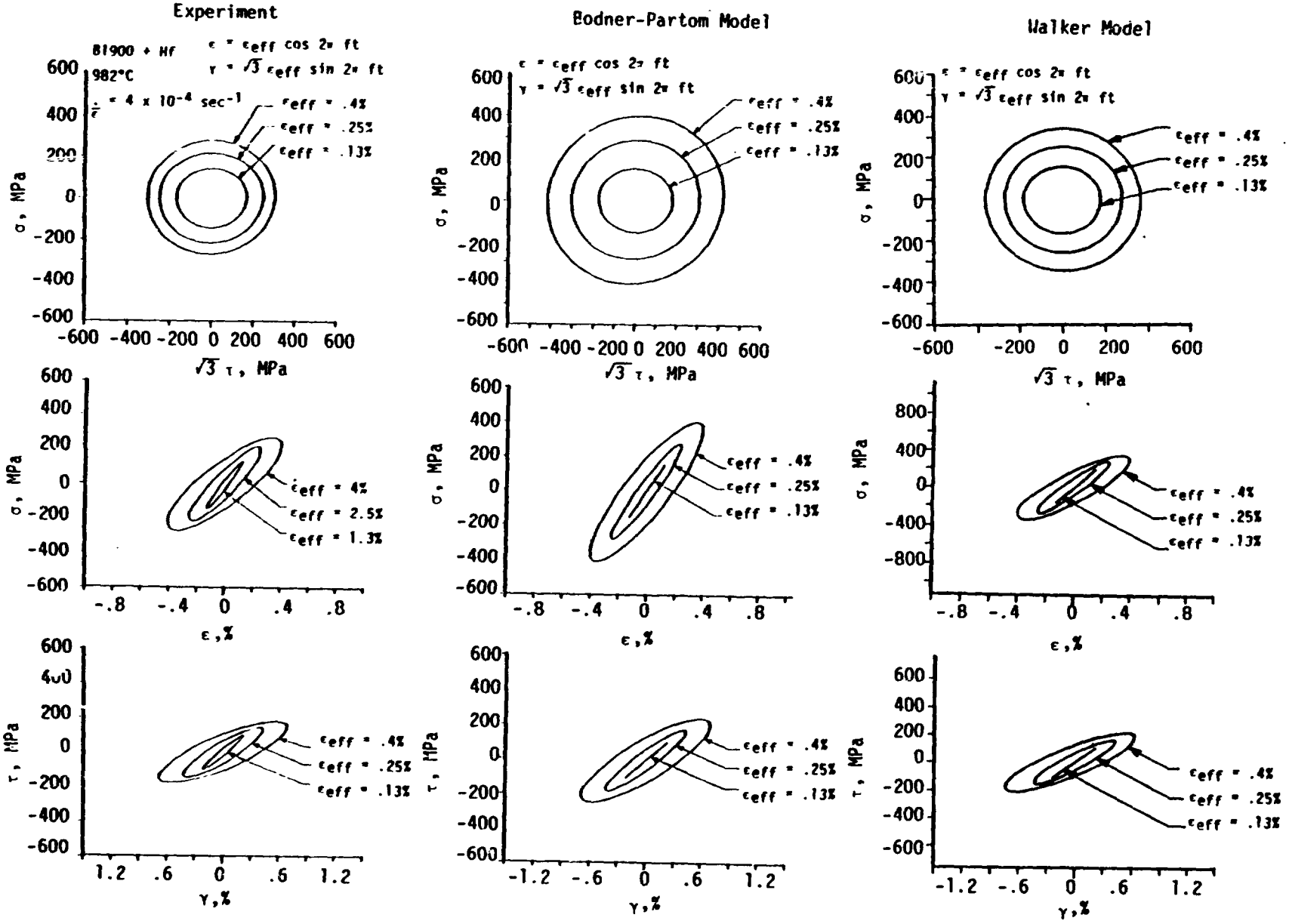

FIGURE 5.9. COMPARISON OF EXPERIMENTAL DATA AND MODEL CALCULATIONS OF B1900+Hf SUBJECTED TO 90° OUT-OF-PHASE LOADING AT THREE EFFECTIVE STRAIN LEVELS AT 982°C.

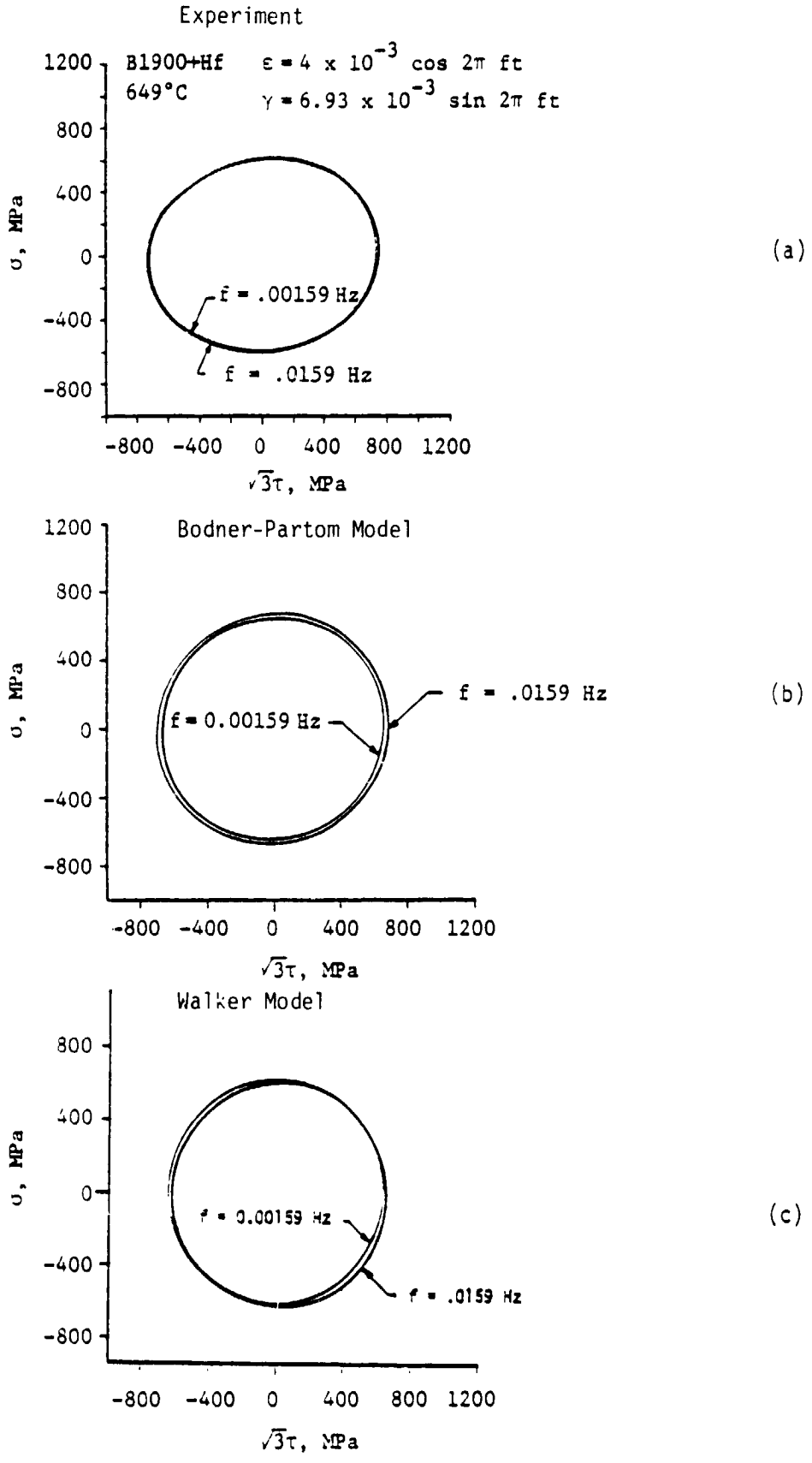

FIGURE 5.10. 90° OUT-OF-PHASE MULTIAXIAL DATA AT TWO FREQUENCIES AT 649°C: (a) EXPERIMENT, (b) BODNER-PARTOM MODEL PREDICTIONS, AND (c) WALKER MODEL.

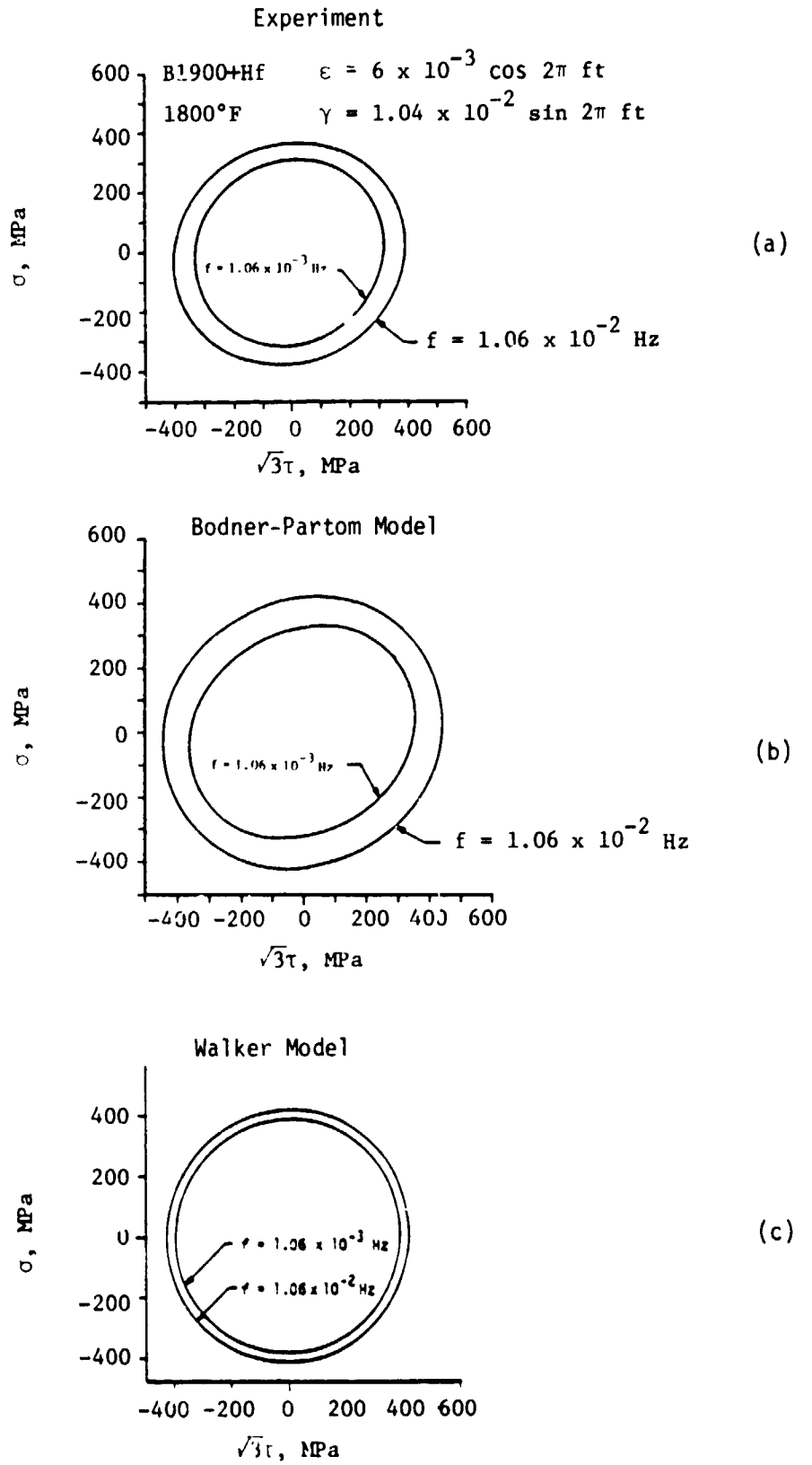

FIGURE 5.11. 90° OUT-OF-PHASE MULTIAXIAL DATA AT TWO FREQUENCIES AT 982°C: (a) EXPERIMENT, (b) BODNER-PARTOM MODEL, AND (c) WALKER MODEL.

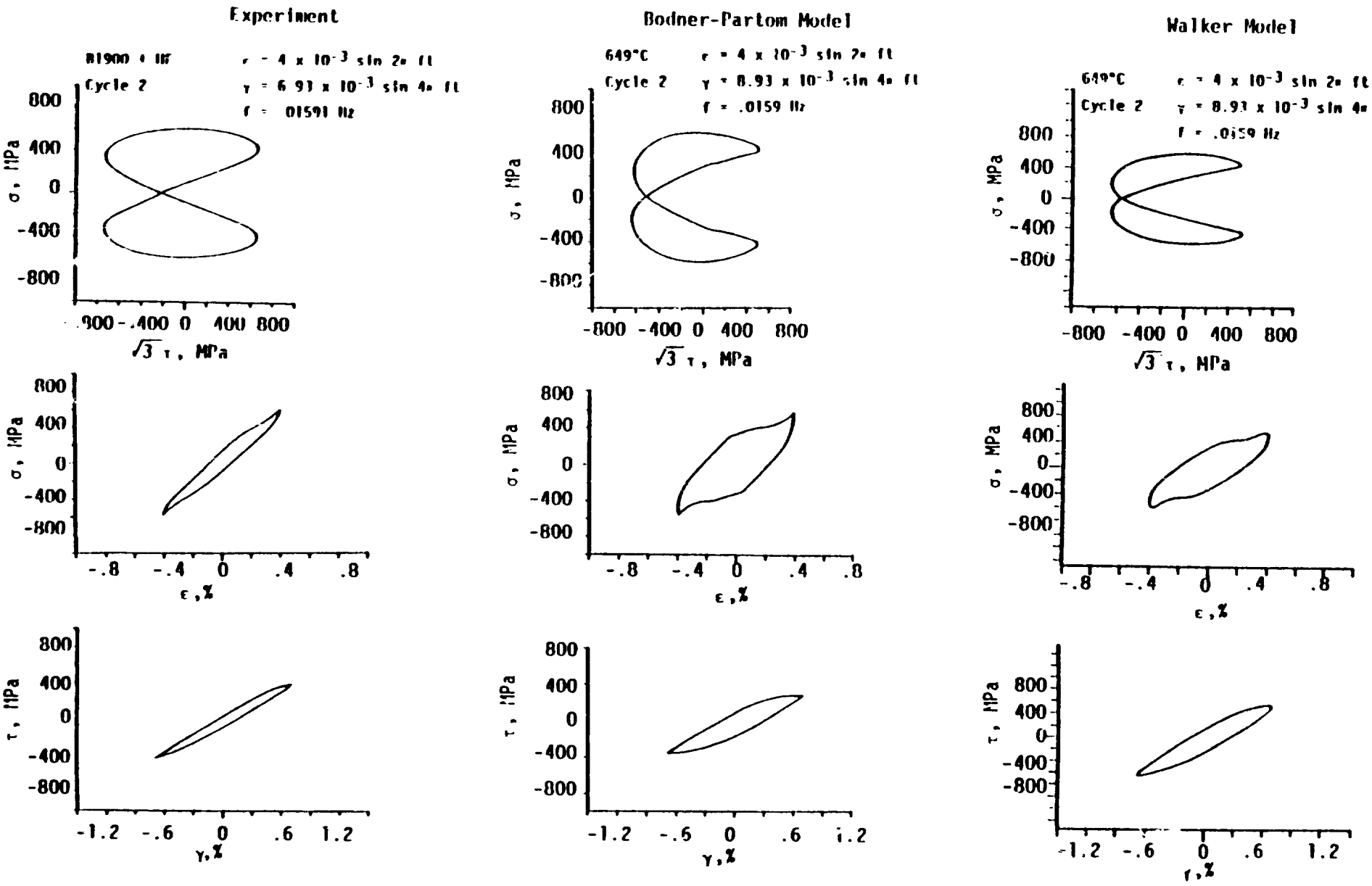

FIGURE 5.12. MODEL CALCULATIONS AND NONPROPORTIONAL MULTIAXIAL DATA WITH DOUBLE FREQUENCIES.

6.0 IMPLEMENTATION IN FINITE ELEMENT COMPUTER CODE

The MARC nonlinear finite element computer program was the vehicle for incorporating the viscoplastic models in this and two previous contract efforts [3,11]. The following section will be divided into four parts: (1) a brief discussion of the MARC code and the procedure for implementing a viscoplastic model, (2) a review of various integrating methods for viscoplastic theories in conjunction with the MARC code, (3) a summary of the conclusions, and (4) demonstration analysis.

6.1 Description of the MARC Program

In References 3 and 11, the viscoplastic constitutive theories were incorporated into the MARC program by means of an initial stress technique. All of the material nonlinearity in the constitutive equations is incorporated into an initial load vector and treated as a pseudo body force in the finite element equilibrium equations. Because the viscoplastic constitutive theories form a "stiff" system of differential equations, it is necessary to form the incremental constitutive equation appropriate to the finite element load increment by means of a subincrement technique.

In the subincrement technique the finite element load increment is split into a number of equal subincrements and the viscoplastic constitutive theories are integrated over the small subincrements to form an accurate representation of the incremental constitutive equation over the finite element load increment. Integration over each subincrement is accomplished by a number of techniques. Provided the subincrements are sufficiently small so that the stability level of the integration method is not exceeded, the technique

has been found to work efficiently and accurately, even for large finite element load increments. However, it is difficult for the user to pick efficient subincremental steps. Thus, there is a considerable incentive for the development of an non-iterative integration scheme which can allow large time step without increasing the instability generally associated with intergrating the differential equations comprising the constitutive theory.

The MARC code allows the user to implement very general constitutive relationships into the program by means of the user subroutine HYPELA. Within this subroutine the user must specify the values of the elasticity matrix D_{ij} and the inelastic stress increment vector $\Delta\xi_i$ in the incremental vector constitutive relationship.

$$\Delta\sigma_i = D_{ij}(\Delta\epsilon_j - \delta_j\alpha\Delta\theta) - \Delta\xi_i \tag{6.1}$$

The inelastic stress increment vector $\Delta\xi_i$ is computed in HYPELA from the viscoplastic constitutive relationships.

In Equation (6.1) α denotes the coefficient of thermal expansion and δ_j is the vector Kronecker delta symbol.

$$\delta_j = \begin{cases} 1 \text{ if } 1 \leq j \leq 3 \\ 0 \text{ if } 3 < j \leq 6 \end{cases} \tag{6.2}$$

For the class of nonlinear viscoplastic constitutive relationships under consideration in this contract, the incremental inelastic stress vector $\Delta\xi_i$ depends in a highly nonlinear manner on the incremental strain vector $\Delta\epsilon_i$.

The solution of the incremental equilibrium is accomplished within the MARC code by the following algorithm. At the start of the increment the user subroutine HYPELA is entered to determine the elasticity matrix D_{ij} and the incremental inelastic stress vector $\Delta\xi_i$. On entry to the subroutine the input consists of the strain increment vector $\Delta\varepsilon_i$, the temperature increment ΔT, the time increment Δt over which the incremental external load vector ΔP_i is applied to the structure, and the values of the stress, strain, temperature and viscoplastic state variables at the beginning of the increment. Since the incremental strain vector, $\Delta\varepsilon_i = B_{ij}\,\Delta u_j$, can only be accurately determined after the solution to the incremental equilibrium relationship has yielded the correct incremental solution Δu_j, the strain increment vector $\Delta\varepsilon_i$ initially used to generate $\Delta\xi_i$ is assumed to be the value obtained for $\Delta\varepsilon_i$ in the preceding increment. On exit from subroutine HYPELA the elasticity matrix D_{ij} and the estimated inelastic stress increment vector $\Delta\xi_j$ are obtained for each integration point in the structure. The incremental equilibrium relationship is then assembled and solved for the incremental node displacement vector Δu_i. The incremental strain vector, $\Delta\varepsilon_i = B_{ij}\,\Delta u_j$, is computed and compared with the initial guess for $\Delta\varepsilon_i$ used to generate the inelastic incremental stress vector $\Delta\xi_j$. If this incremental strain vector is equal, within a user specified tolerance, to the incremental strain vector used to compute $\Delta\xi_j$ in the assembly phase, the solution is assumed to have converged. Otherwise, the updated strain increment vector, obtained from the solution of the equilibrium relations is passed into subroutine HYPELA, a new vector, $\Delta\xi_j$, is computed, and the equilibrium equations resolved to yield an improved value of Δu_j and $\Delta\varepsilon_j$. The process is repeated until the value of the vector $\Delta\varepsilon_i$ on the assembly phase is equal, within a user specified tolerance, to the value of the

vector $\Delta\varepsilon_i$ on the solution phase. After convergence is achieved, the temperature, stress vector, strain vector and viscoplastic state variables are updated by adding the incremental values generated during the current increment to the values of these variables at the beginning of the increment. The program then passes on to the next load increment where the process is repeated.

6.2 Integration Methods for Viscoplastic Theories in the MARC Code

The values of D_{ij} and $\Delta\xi_i$ in the incremental constitutive relation,

$$\Delta\sigma_i = D_{ij}(\Delta\varepsilon_j - \delta_j \alpha\Delta T) - \Delta\xi_i \tag{6.3}$$

are obtained by a subincrement method. Incremental values of the variables ΔT, Δt and ($\Delta\varepsilon_i$ and $\delta_j \alpha\Delta T$) for the current finite element load increment are split NSPLIT equal values, and the constitutive equations are integrated over the NSPLIT subincrements to provide accurate values of D_{ij} and $\Delta\xi_i$. Each load increment in a MARC analysis is divided into NSPLIT subincrements. The integration of the constitutive equations is currently performed by using explicit Euler forward differences with a step size determined by dividing the MARC load increment by NSPLIT.

Two methods for integrating the constitutive equations were examined: (1) an explicit Euler difference scheme with error estimates for revision the time step, and (2) integration by the NONSS (non-iterative self-adaptive solution) method of Miller and Tanaka [12]. The forward difference integration, similar to [13], is based on an error estimate, E, given by

$$E = \Delta R + \frac{\sqrt{3\Delta J_2}}{2\mu} \tag{6.4}$$

where

$$\Delta R = \sqrt{\frac{2}{3}\ \Delta\varepsilon^{p}_{ij}\ \Delta\varepsilon^{p}_{ij}}$$

ε^{p}_{ij} is the inelastic strain

S_{ij} is the deviatoric stress

Δ of a quantity is the change in the quantity over time step Δt. If the error estimate is too large

$$\varepsilon > \varepsilon_1 \tag{6.5}$$

then the time step is halved and the step is repeated. If the error estimate is too small.

$$\varepsilon < \varepsilon_2 \tag{6.6}$$

then the time step is doubled for the next integration step.

It was found to be more difficult to integrate Bodner-Partom's equations using an explicit Euler integration and as a result the NONSS method was applied to the integration of Bodner-Partom's constitutive equations in the calculations done at SwRI. The NONSS method can be illustrated by considering the following two differential equations in two unknowns,

$$\dot{x} = f\ (x,y) \tag{6.7}$$

$$\dot{y} = g(x,y) \tag{6.8}$$

where $\dot{(\ )} = \frac{d(\ )}{dt}$

Consider a time step Δt from time t_N to time t_{N+1} where

$$\Delta t = t_{N+1} - t_N$$

then the changes in each of the dependent variables are approximately

$$\Delta x = x_{N+1} - x_N = \Delta t\,[(1-n)\,\dot{x}_N + n\,\dot{x}_{N+1}] \tag{6.9}$$

$$\Delta y = y_{N+1} - y_N = \Delta t\,[(1-n)\,\dot{y}_N + n\dot{y}_{N+1}] \tag{6.10}$$

where $0 \leq n \leq 1$.

If n is equal to zero an explicit Euler integration results while if n is equal to one an implicit Euler integration results.

Equations (6.7) and (6.8) can be used for the derivatives at the new time steps. For example:

$$\dot{x}_{N+1} = f(x_{N+1}, y_{N+1}) = f(x_N + \Delta x, y_N = \Delta y) \tag{6.11}$$

A Taylor series can be used to expand the function. Then

$$\dot{x}_{N+1} = f\,(x_N, y_N) + \Delta x\, f_{,x}\,(x_N, y_N) + \Delta y\, f_{,y}\,(x_N, y_N) \qquad (6.12)$$

A similar equation holds for y_{N+1}

$$\dot{y}_{N+1} = g\,(x_N, y_N) + \Delta x g_{,x}\,(x_N, y_N) + \Delta y g_{,y}\,(x_N, y_N) \qquad (6.13)$$

$$[1 - n\Delta t\, f,_x(x_N, y_N)]\,\Delta x - n\Delta t f_{,y}\,\Delta y = \Delta t\,\{\dot{x}_N - n[\dot{x}_N - f(\dot{x}_N, \dot{y}_N)]\} \qquad (6.14)$$

$$-n\Delta t g_{,x}\,\Delta x + [1 - n\Delta t g_{,y}\,(x_N, y_N)]\Delta x = \Delta t\{\dot{y}_N - n[\dot{y}_N - g\,(\dot{x}_N, \dot{y}_N)]\} \qquad (6.15)$$

Equations (6.14) and (6.15) are two linear equations in the two unknown Δx and Δy. The error in the truncation of the Taylor series is included in the difference.

$$\dot{x}_N - f(x_N, y_N) \text{ and}$$

$$\dot{y}_N - g(x_N, y_N)$$

which is applied in the next increment.

Computer codes based on Euler integration have been completed and tested for both models. The computer code based on the NONSS method has not been completely implemented in the MARC Code. All the Bodner-Partom calculations performed at SwRI are based on the NONSS method.

6.3 Constitutive Model Demonstration - TMF Simulations

The successful implementation of the constitutive models into the MARC computer program was established by performing uniaxial analyses and comparing the predicted and observed experimental response for three thermomechanical loading cycles. The comparison was made with both constitutive models.

An illustrated comparison of the calculated results with the experimental data for the TMF Cycle A is shown in Figure 6.1 Comparison of Figure 6.1 and Figure 4.35 indicates that the TMF loop based on the Bodner-Partom model obtained at PWA using the Euler integration scheme (Figure 6.1) is identical to that obtained at SwRI using the NONSS method. The good agreement between the two calculations represents a check on the computer codes developed at PWA and SwRI.

6.4 Computational Efficiency

A study to compare the stability and computing efficiency of the Walker and the Bodner-Partom theories was conducted. This study was done using the MARC finite element deck and a four element model using element type 10, a first order quadrilateral ring element. The convergence criterion used internally in MARC was for the maximum residual force to be less than 0.10 times the maximum reaction force for the model. Using this criterion, the finite element model was executed with three different sets of increments for a single TMF cycle. The computation times were recorded and are shown in Table 6.1. Examples of the calculated stresses are shown in Figures 6.1 and

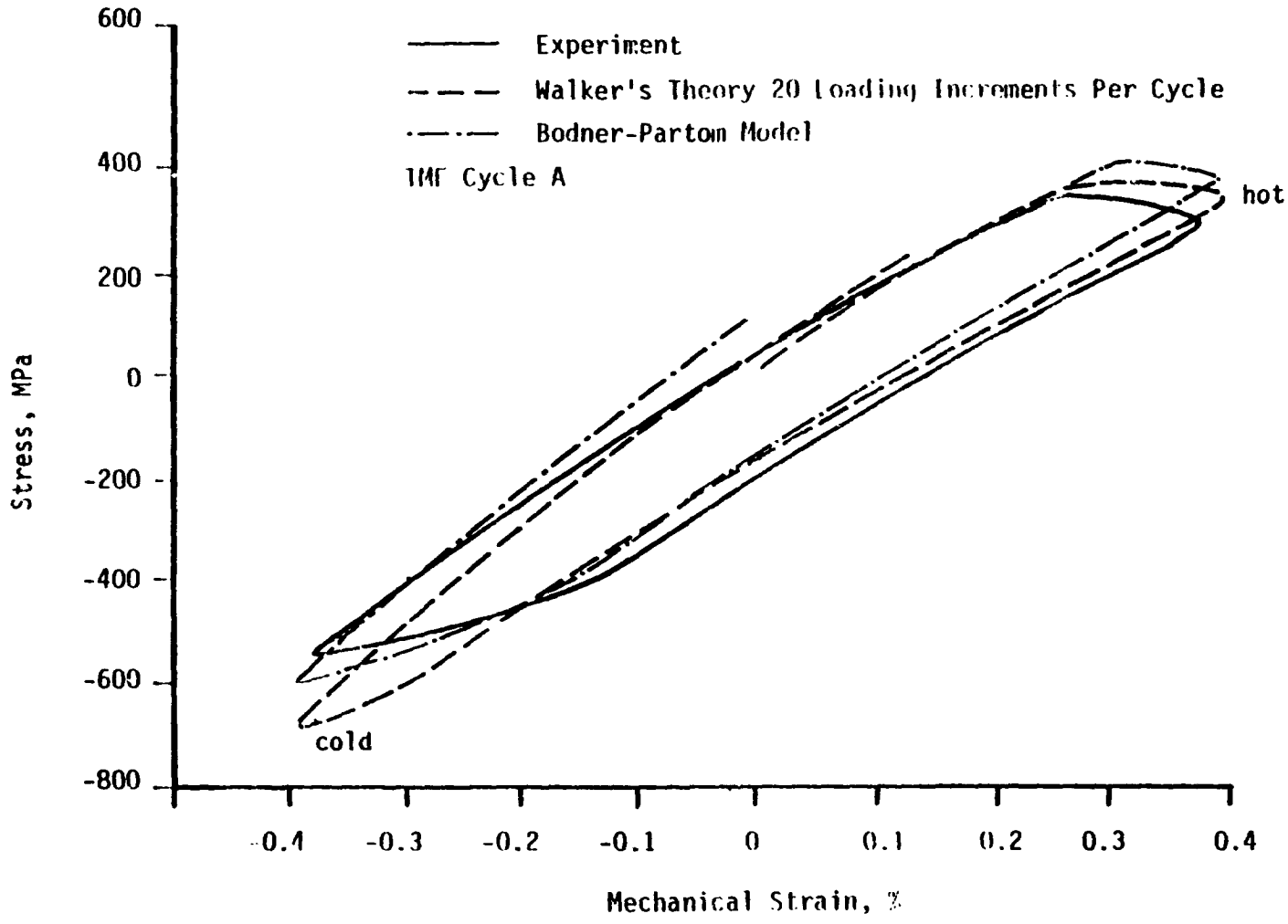

FIGURE 6.1. COMPARISON OF EXPERIMENTAL AND CALCULATED TMF LOOPS USING THE MARC CODE AND 20 LOADING INCREMENTS.

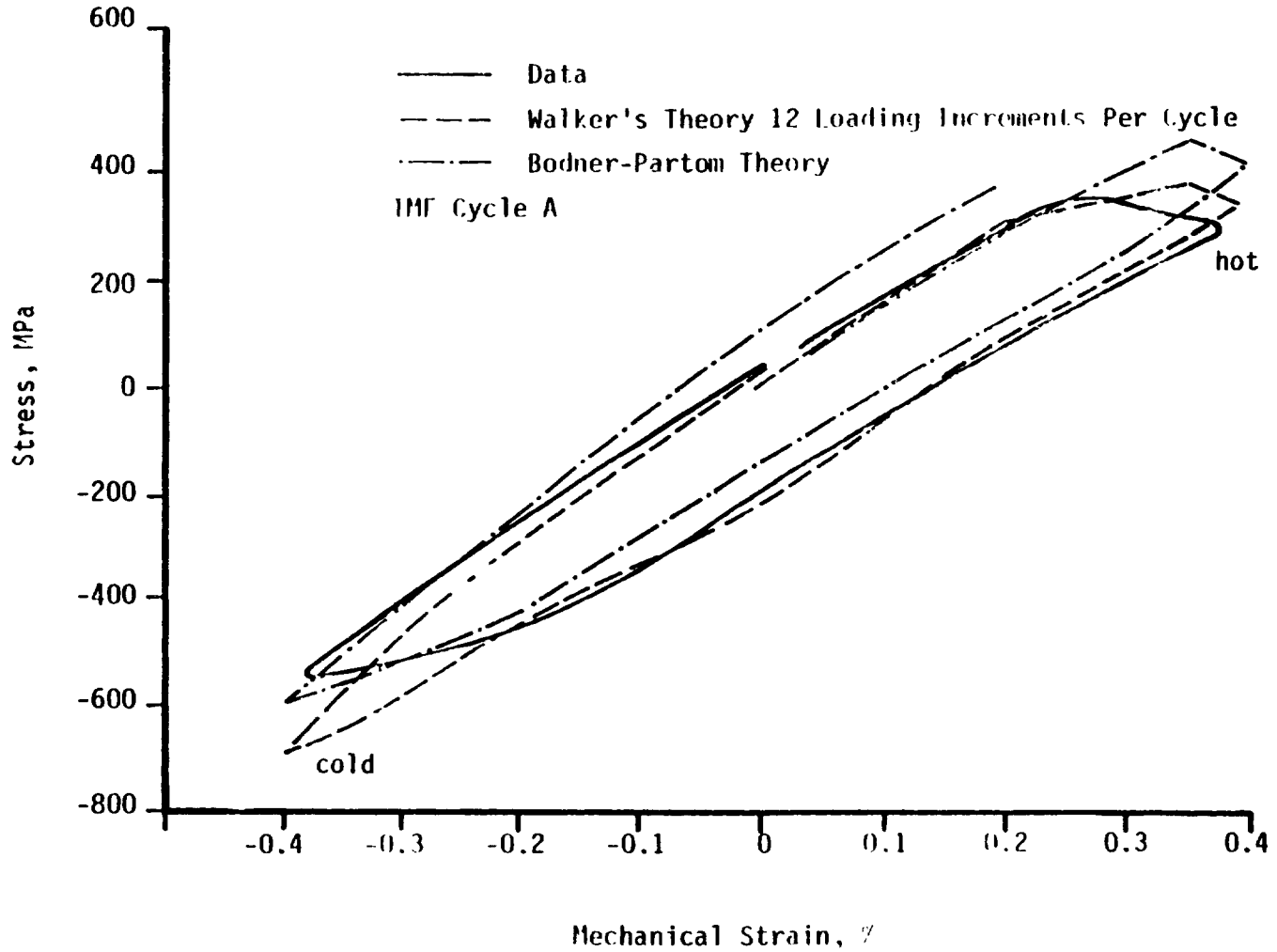

FIGURE 6.2. COMPARISON OF EXPERIMENTAL AND CALCULATED TMF LOOPS USING THE MARC CODE AND 12 LOADING INCREMENTS.

Table 6.1

Comparison of Execution Time and Convergence Accuracy
for Differing Increment Number per Cycle. Out of Phase TMF Cycle

Walker

Increments	Solution Time (sec)	Convergence Accuracy (%)*
40	11.19	0.51
20	7.01	1.49
12	7.41	2.12

Bodner-Partom

Increments	Solution Time (sec)	Convergence Accuracy (%)*
40	35.35	0.16
20	23.94	2.43
12	25.04	0.32

* Estimated as the magnitude of the residual stress divided by the maximum stress in the cycle.

6.2. The examples shown are tne runs using 20 increments per cycle for both the Walker and Bodner-Partom theories and the runs using 12 increments per cycle. The results from the 40 increments per cycle are not shown since they were found to be virtually identical to the cases with 20 increments per cycle. The results shown in Figures 6.1 and 6.2 are a comparison of the relative computational stability of the two theories as currently implemented in the MARC deck. The Bodner-Partom theory results begin to degrade at the hot end at 12 increments per cycle whereas the Walker theory continues to calculate acceptable results. Both calculations show difficulties in convergence when 12 increments are used in the loading cycle, as evidenced by the increase in computation time per increment. This latter effect can be seen from the computing times shown for the 20 and 12 increment cases shown in Table 6.1. An examination of these times shows that for both theories the total computing time increased slightly even though the number of loading increments decreased by 40 percent.

Another significant result of this study is indicated by the run times shown in Table 6.1. For the same convergence criterion and the same integration method the Bodner-Partom model required approximately 3 times as long as the Walker model to calculate stresses. The reason for the longer solution times relates to the larger number of subincrement integration steps required to satisfy limits on the error estimates in the HYPELA subroutine. Other independent studies have indicated roughly equivalent computing time for these and other unified models. Such comparisons will be dependent upon the particular problem and integration schemes utilized.

7.0 BENCHMARK NOTCH VERIFICATION EXPERIMENTS AND ANALYSES

Elevated temperature testing of instrumented notched round specimens was conducted to generate notch displacement data for verification of the analytical methodologies developed in this program. The unified constitutive theories of Walker and of Bodner-Partom were incorporated into the MARC finite element code for predicting structural response behavior. Calculations were performed based on the Walker model for the benchmark notched specimen subjected to a variety of histories and the results are discussed in this section. Correlation of model predictions and experimental data serves as an additional test of the accuracy and applicability of the constitutive models. The notched round specimen was selected for the following reasons: (1) to permit notch strains to be measured directly using conventional extensometry, (2) to facilitate finite element analysis by avoiding the need for 3D elements, and (3) to verify the ability of finite element analysis to predict material behavior under conditions of high constraint.

Testing was conducted for six load patterns at 871°C over load ranges sufficient to result in short time inelastic behavior and over load times sufficient to induce significant time-dependent inelastic notch strain. The specimen design and experimental procedures of the benchmark notch test are discussed in Section 7.1. The analytical efforts and correlation of theoretical calculation and experimental data are reported in Section 7.2

7.1 Specimen Design and Experimental Procedures

The benchmark notch specimen was designed based on the following considerations: (1) the tensile load capability of the test machine was limited to ± 36000 N, (2) local plastic strains needed to be measured indirectly, to

within ± 20% of their cyclic value, (3) a fatigue life of 100 cycles to initiation of a first crack was required, and (4) testing had to be performed at a temperature within the creep range.

Fully reversed strain controlled testing in the NASA Host Isotropic Fatigue Program (NAS3-23288) has established the total and cyclic plastic strain levels corresponding to a fatigue life of approximately 100 cycles to initiation of a first crack. At 760, 871, and 982°C the magnitude of the cyclic plastic strain at this life level is 0.03%, 0.15%, and 0.2%, respectively. A test temperature of 871°C was selected based on consideration that testing should be conduced at as high a temperature as possible to maximize the nonlinear effects but low enough to preclude net section plasticity.

A notched round specimen with an elastic stress concentration factor of 1.5 was selected and approved for the benchmark notch experiment (Figure 7.1). The configuration of the notched round specimen satisfied the two requirements; (1) limited net section plasticity, and (2) measurement of either cross notch or diametrical displacement should yield a fair measurement of local notch plastic strain. Cross notch and diametrical displacements were measured using axial and diametrical MTS extensometers. Figure 7.2 illustrates the experimental setup of the benchmark notch test.

In order to establish the required sensitivity of the measuring devices, a nonlinear FE analysis of the specimen configuration was performed. Cross notch displacement was not found to be as strong an "indication" of local notch plasticity as the diametrical contraction at the notch throat. A better measure of the notch plastic strain is the permanent radial displacement at the notch throat. For 0.15% cyclic plastic strain the extent of the nonlinear diametrical strain is only 70 $\mu\varepsilon$. To satisfy the requirement that

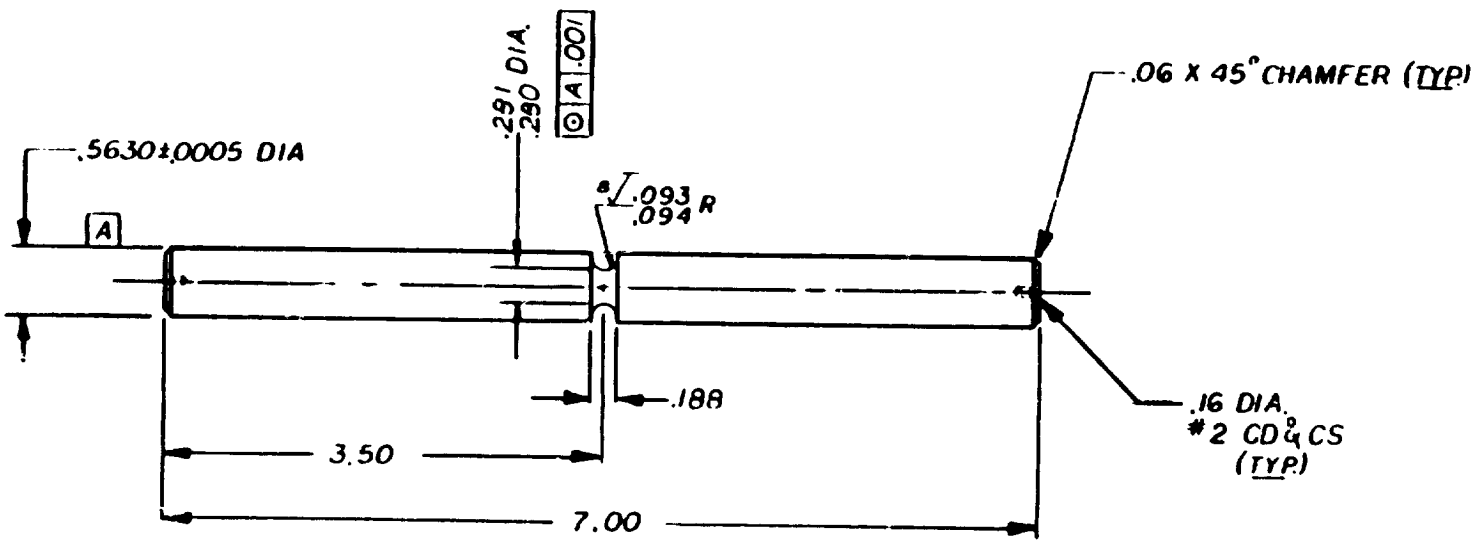

FIGURE 7.1 THE DESIGN OF THE BENCHMARK NOTCH ROUND SPECIMEN.
(All units are in inches.)

FIGURE 7.2 BENCHMARK NOTCH ROUND SPECIMEN UNDER TEST AT 871°C.

the constitutive model be able to correlate fatigue life to within a factor of two, the local notch strain must be measured to within ± 0.03%, which translates to a diametrial strain sensitivity of ± 14 με . This level of accuracy is within the capability of the capacitance extensometry utilized in the benchmark experiment, but all other sources of error must be minimized.

All the notched round cyclic tests were conducted at 871°C under fully reversed load-controlled conditions at 10 cpm. The specimens were cycled at ± 331, ±352, ± 365, ± 386, and ± 414 MPa for 10 cycles at each stress level. The load sequence was repeated twice for a total of 100 cycles. For cycling with dwell, the same load sequence was used with a minute hold applied at; (1) maximum tension, (2) maximum compression, and (3) maximum tension and compression. In addition to the cyclic tests, a notched round specimen was pulled monotonically almost to failure at a displacement rate of $5x10^{-4}$ mm/sec measured over a 25.4 mm gauge span. A monotonic tensile test with dwell was also conducted by step loading beginning at 379 MPa up to 517 MPa in 34.5 MPa increments. A 15 minute dwell time was applied at each load level. A summary of the benchmark notched round tests is shown in Table 7.1.

7.2 Finite Element Analyses

7.2.1 Finite Element Mesh Selection

The element type has been selected according to MARC recommendation. For the large strain plasticity problems as in monotonic loading of a D-notch round specimen, simple element types (e.g., axisymmetric element 10) and those elements containing a modified strain integration procedure (axisymmetric element 55) are preferable.

TABLE 7.1

A SUMMARY OF THE BENCHMARK NOTCHED ROUND TESTS

Specimen	Frequency, CPM	R, Ratio	Applied Stress, MPa	Dwell Period
B1	10	-1	BENCHMARK LOAD SPECTRUM	No dwell
B4	10	-1	BENCHMARK LOAD SPECTRUM	1 minute at maximum tension
B5	10	-1	BENCHMARK LOAD SPECTRUM	1 minute at maximum compression
B6	10	-1	BENCHMARK LOAD SPECTRUM	1 minute at maximum tension and compression
B3	--	Monotonic	Tension to Failure	---
B7	--	Stepped Load tension starting at 370 MPa (55 ksi) with 34.5 MPa (5 ksi) increments to a maximum stress of 517 MPa (75 ksi)		15 minute dwell at each load level

BENCHMARK LOAD SPECTRUM: Cycling at ± 331, ± 352, ± 365, ± 386, and ± 414 MPa (± 48, ± 50, ± 53, ± 56, ± 60 ksi) for 10 cycles at each stress level. The load spectrum was repeated twice at 871°C.

Figure 7.3 illustrates the four meshes of the test specimen considered in this phase of the study. The number of elements surrounding the notch varied from six in the coarse mesh to sixteen in the finest mesh. For purposes of mesh evaluation, a conventional time independent plasticity model was utilized. The assumed stress-strain material behavior reasonably approximated the observed tensile response of B1900+Hf at 871°C. Incremental displacements were applied to the model, care being taken to assure that the step size was not excessive. Results of the four analysis were presented in Tables 7.2 through 7.5.

The relative computational requirements, presented in Table 7.2 indicate a ten fold increase in CPU time when the mesh density was refined by a factor of about two. In Table 7.3 the limit load predictions are compared. A difference of only 2.7 percent exists between the limit load predictions for the coarsest and the finest mesh. The limit load is therefore not an adequate criterion for determining an optimum mesh. Table 7.4 presents the predicted load to produce a variation in the inelastic radial displacement at the notch root equal to 3.05×10^{-2} mm. As noted in the table, a difference of only 2.8 percent exists between the load required to produce an inelastic radial displacement of 3.05×10^{-2} mm (1.2×10^{-3} in) for the coarsest and finest mesh. This parameter, a measurable quantity, is also not adequate for selecting a mesh. A final comparison relates the axial stress at the notch root to the nominal gage length strain. As noted in Figure 7.4 and Table 7.5, the mesh selection has a somewhat larger effect on the predicted value of the local stress. The intermediate mesh would appear to achieve an acceptable precision without incurring unacceptable CPU charges and was selected for correlation of the test data.

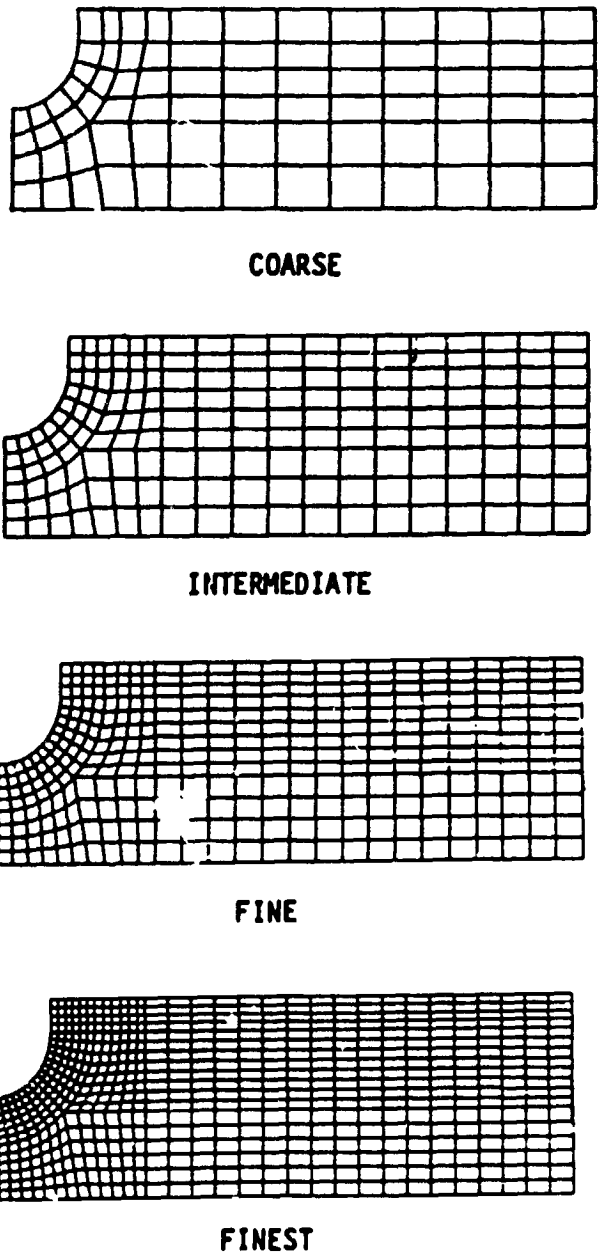

FIGURE 7.3. MODELS CONSIDERED IN MESH SENSITIVITY STUDY

TABLE 7.2

CPU REQUIREMENTS FOR VARIOUS D-NOTCH MODELS

MARC Element	Mesh	CPU/Increment (seconds)
10, 4 node linear quadrilateral	Coarse	4.0
	Intermediate	5.0
	Fine	14.5
	Finest	40.0
55, 8 node quadratic quadrilateral	Intermediate	23.0

TABLE 7.3

LIMIT LOAD COMPARISON FOR VARIOUS D-NOTCH MODELS

MARC Element	Mesh	Relative Limit Load
10, 4 node linear quadrilateral	Coarse	1.027
	Intermediate	1.0133
	Fine	1.004
	Finest	1.0
55, 8 node quadratic quadrilateral	Intermediate	0.995

TABLE 7.4

INELASTIC RADIAL DISPLACEMENT AT NOTCH ROOT COMPARISONS
FOR VARIOUS D-NOTCH MODELS

MARC Elemen	Mesh	Relative Load at $\Delta\delta r$ of 1.2×10^{-3}
10, 4 node linear quadrilateral	Coarse	1.028
	Intermediate	1.013
	Fine	1.003
	Finest	1.00
55, 8 node quadratic quadrilateral	Intermediate	0.995

TABLE 7.5

LOCAL NOTCH STRESS FOR VARIOUS D-NOTCH MODELS

MARC Element	Mesh	Local Relative Notch Stress at Limit Load
10, 4 node linear quadrilateral	Coarse	1.09
	Intermediate	1.05
	Fine	1.03
	Finest	1.0
55, 8 node quadratic quadrilateral	Intermediate	0.99

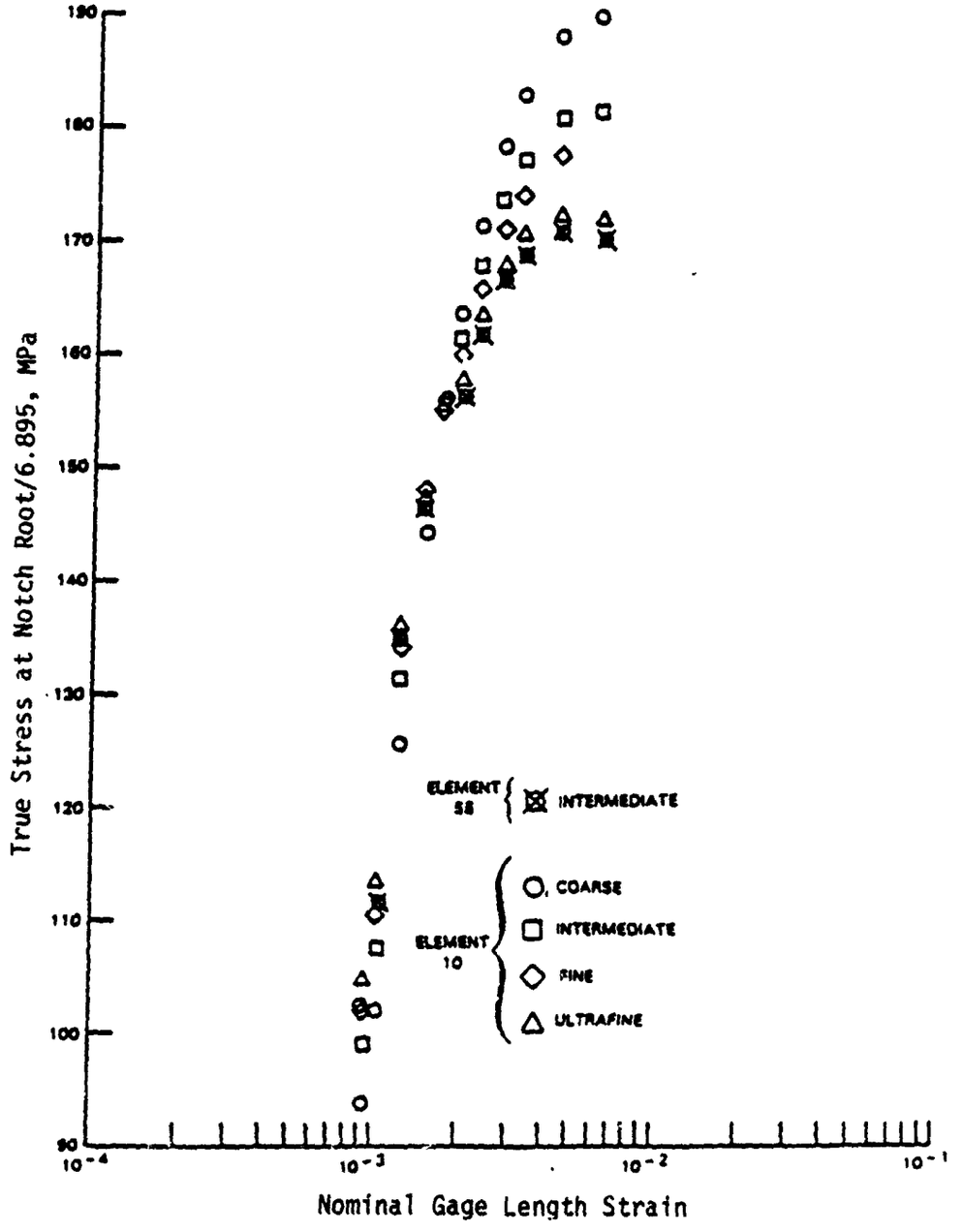

FIGURE 7.4. NOTCH STRESS VS. GAGE LENGTH STRAIN FOR VARIOUS U-NOTCH MODELS.

7.2.2 Experimental Results and Finite Element Predictions

Test results, in particular, the variation of the notch root diametrial displacement with load level, cycle number and loading wave form are described below. A comparison with the MARC finite element predictions using the Walker unified constitutive theory is also presented.

a) Fully Revised Cycling with No Hold (Specimen B1)

The specimen was cycled for ten cycles at each of five load levels beginning at a net section stress of ± 331 MPa. No hysteresis in the load versus notch diametrial displacement was observed at the three lowest load levels. At ± 386 MPa and ± 414 MPa, some cyclic inelastic behavior was noted. The magnitude of the peak to peak notch displacement and the cyclic notch inelastic displacement did not change appreciably with increasing cycles at any load level, Figure 7.5 (a) and Figure 7.5 (b). No accumulation in mean notch displacement with cycles was noted. Notch displacement versus load for the sixth cycle at ± 414 MPa are presented in Figure 7.6.

The MARC finite element code with the Walker model was used to simulate six cycles of loading at the ± 414 MPa load level. No hardening or softening with increased cycling was predicted. The peak-to-peak variation in notch displacement was correctly estimated; however, considerably more cyclic notch plasticity was predicted than observed in the test, as illustrated in Figure 7.6.

b) Fully Reversed Cycling with One Minute Hold in Tension (Specimen B4)

The specimen was cycled for ten cycles at each or five load levels beginning at ± 331 MPa. During the first and every subsequent hold in tension for one minute, a notch diametrical contraction which was partially recovered on load reversal was noted. Notch displacement versus load response

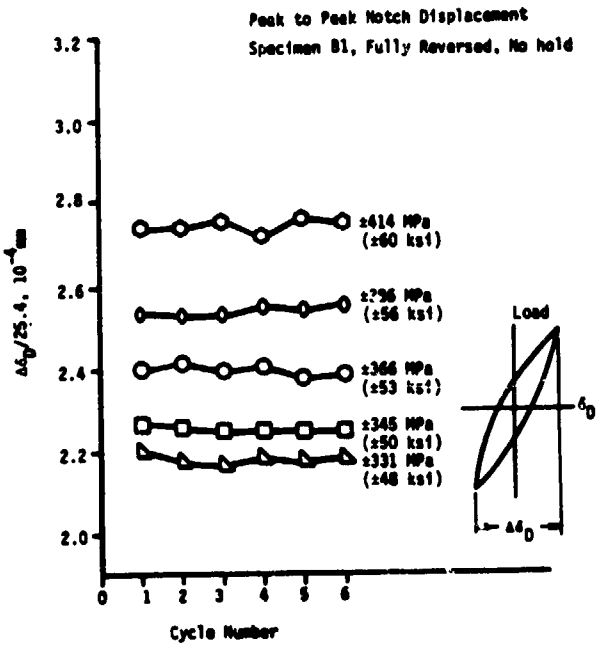

FIGURE 7.5. (a) PEAK TO PEAK DISPLACEMENT, TEST B1, FULLY REVERSED, NO HOLD.

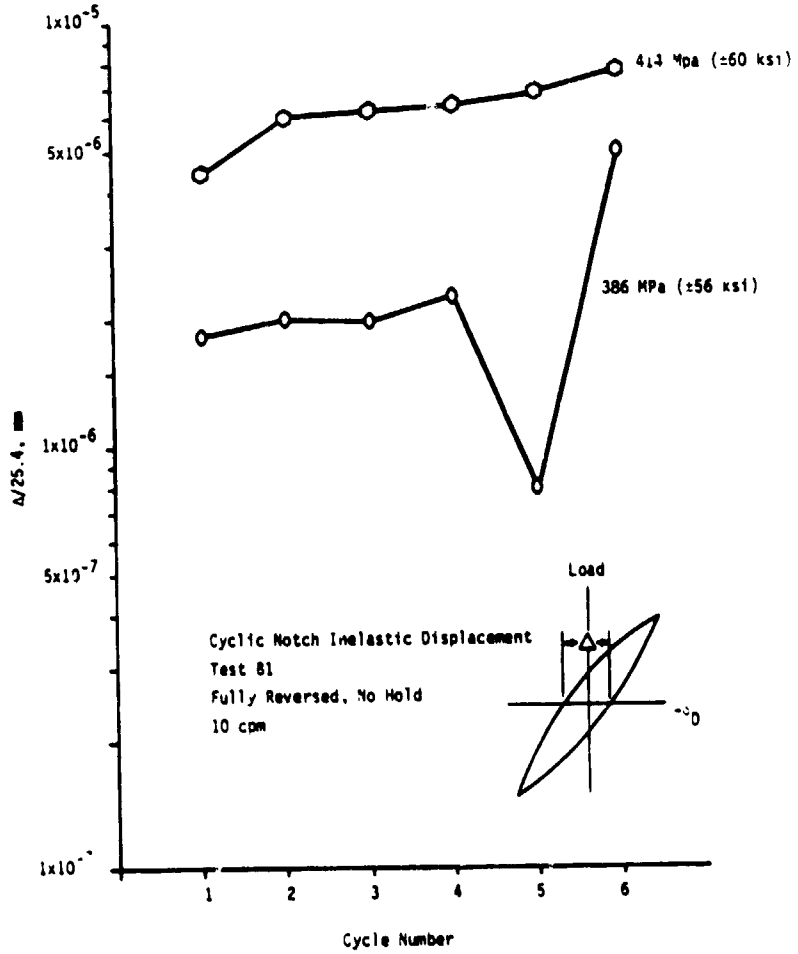

FIGURE 7.5. (b) CYCLIC NOTCH INELASTIC DISPLACEMENT, TEST B1, FULLY REVERSED, NO HOLD.

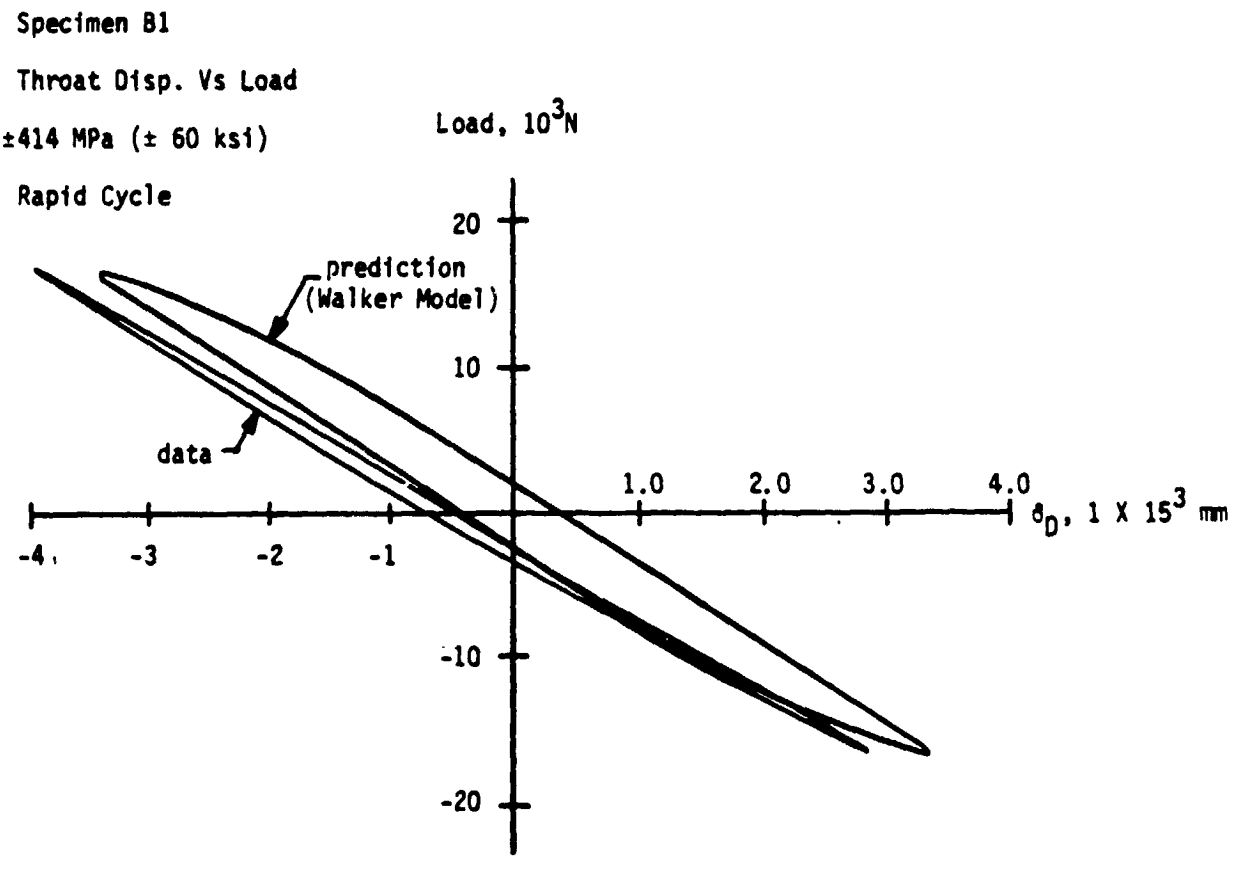

FIGURE 7.6. LOAD VS. NOTCH DIAMETRIAL DISPLACEMENT, TEST B1 FULLY REVERSED.

for the sixth cycle at the ± 331 MPa load level are presented in Figure 7.7. Hysteresis is present in the results. The cyclic drift in the mean notch diameter was small but always increased with increasing cycles and load level. The magnitude of the peak-to-peak notch displacement and the cyclic inelastic notch displacement, in Figures 7.8(a) and 7.8(b), shows little systematic variation with the cycle number.

The finite element calculation underestimates the peak-to-peak throat displacement by as much as seventeen percent, but predicts the cyclic inelastic notch displacement at the ± 414 MPa load level quite accurately. No hardening or softening is predicted, in agreement with the test data.

The variation of the mean notch displacement at the lowest (± 331 MPa) and highest (± 414 MPa) load levels with hold time is presented in Figures 7.9(a) and 7.9(b), respectively. The notch displacement during the one minute tensile holds is underpredicted by the analysis at both stress levels.

c) Fully Reversed Cycling with One Minute Hold in Compression (Specimen B5)

The specimen was cycled for ten cycles at each of five load levels with a one minute hold in compression. During the first and subsequent one minute compression hold, a notch diametrial expansion which was totally recovered on load reversal was observed. This behavior is in contrast to that observed in Specimen B4. The notch diametrial displacement variation with load for the sixth cycle at ± 331 MPa (± 48 ksi) is shown in Figure 7.10. Hysteresis is present in the load displacement response with no drift in the mean cyclic notch diameter at any load level. The magnitude of the peak-to-peak notch displacement and cyclic inelastic notch displacement with increasing cycles at each load level are summarized in Figures 7.11(a) and 7.11(b), respectively. The cyclic response stabilizes quickly upon load change. The

Specimen B4
Cycle 6
±331 MPa

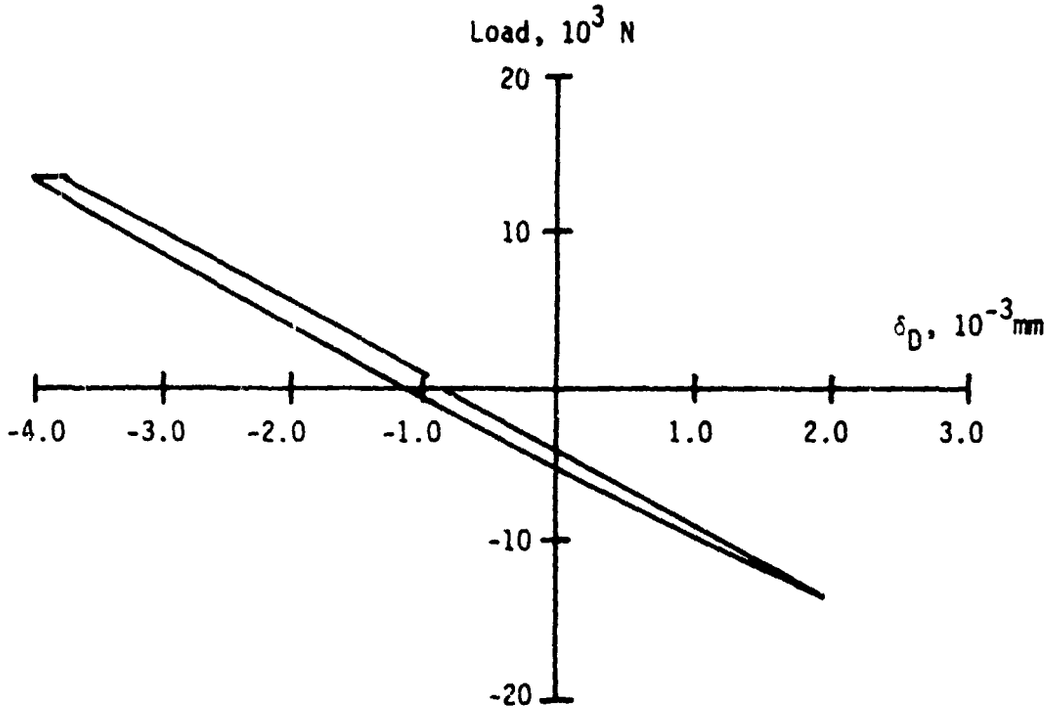

FIGURE 7.7. LOAD VS. NOTCH DIAMETRIAL DISPLACEMENT, TEST B4, FULLY REVERSED, ONE MINUTE HOLD TENSION AT 331 MPa.

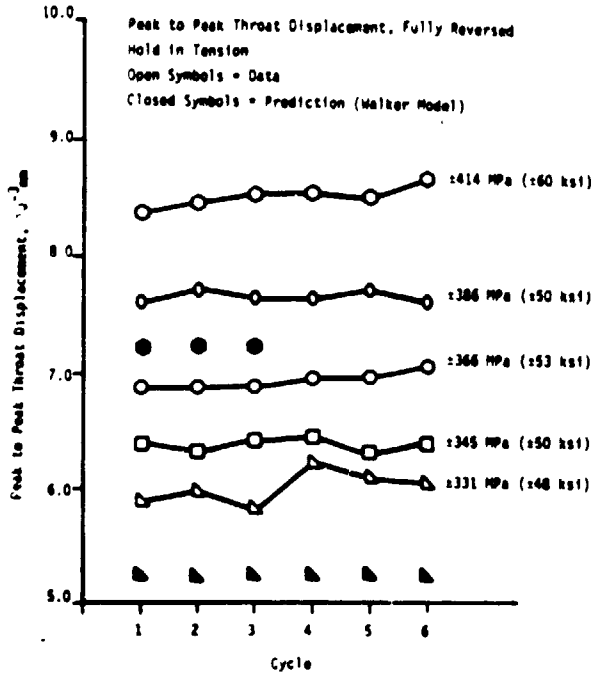

(a)

FIGURE 7.8. (a) PEAK TO PEAK NOTCH DISPLACEMENT, TEST B4, FULLY REVERSED, ONE MINUTE HOLD TENSION.

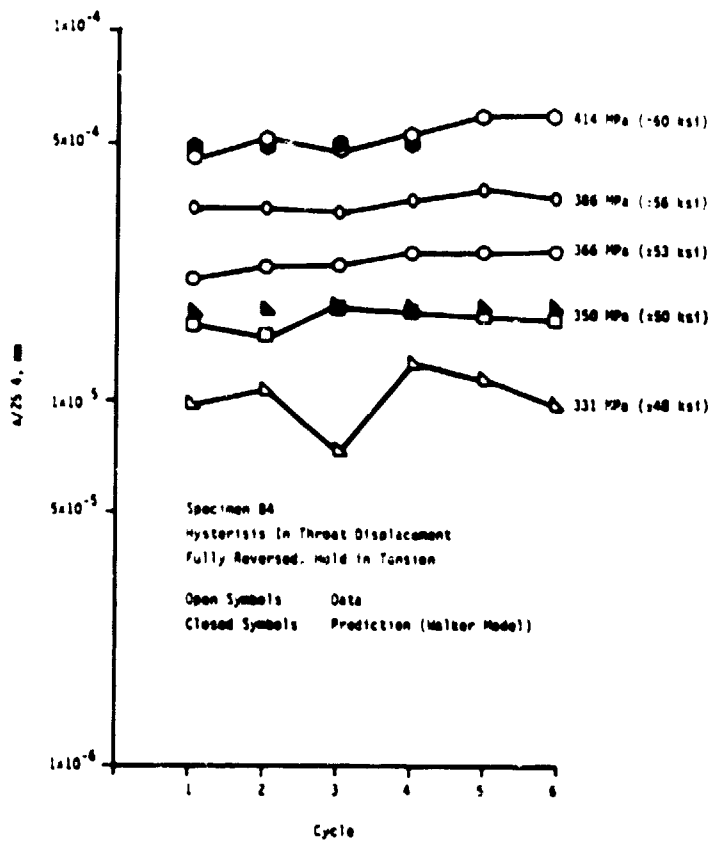

(b)

FIGURE 7.8. (b) CYCLIC NOTCH INELASTIC DISPLACEMENT, TEST B4, FULLY REVERSED, ONE MINUTE HOLD TENSION.

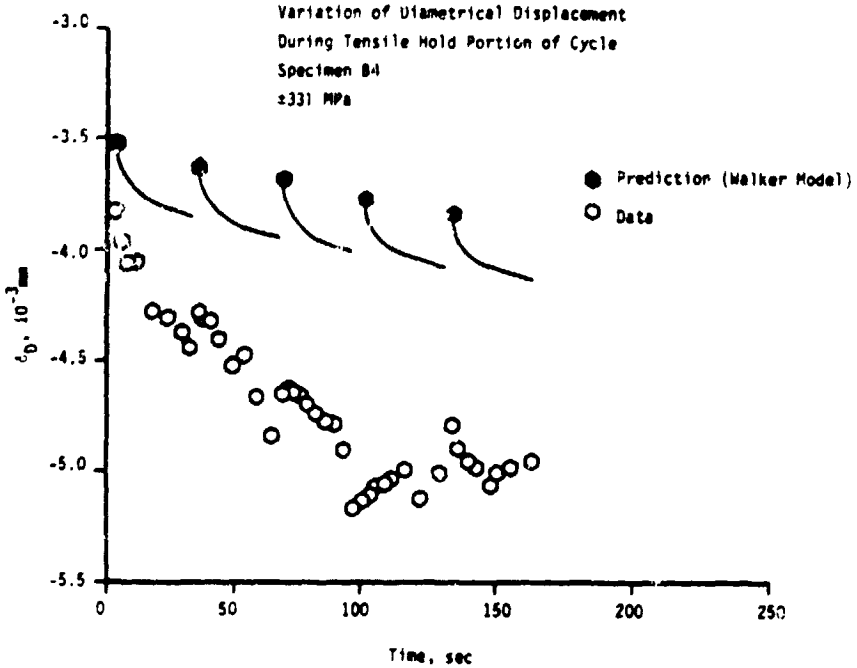

(a)

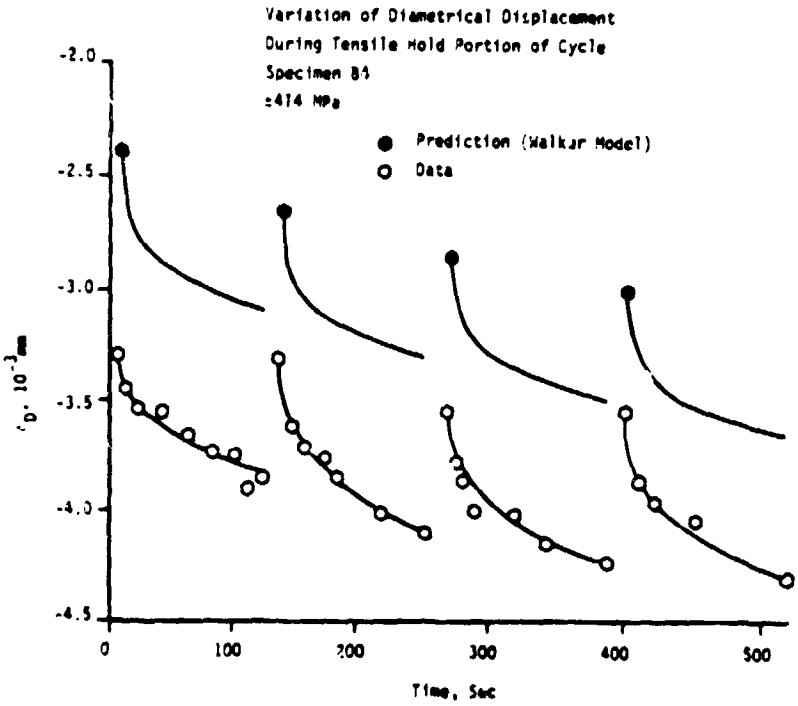

(b)

FIGURE 7.9. (A) VARIATION OF NOTCH DIAMETRIAL DISPLACEMENT DURING TENSILE HOLD PORTION OF CYCLE, 331 MPa, SPECIMEN B4, FULLY REVERSED, ONE MINUTE HOLD TENSION AND (B) VARIATION OF NOTCH DIAMETRIAL DISPLACEMENT DURING TENSILE HOLD PORTION OF CYCLE, 414 MPa, TEST B4, FULLY REVERSED, ONE MINUTE HOLD TENSION.

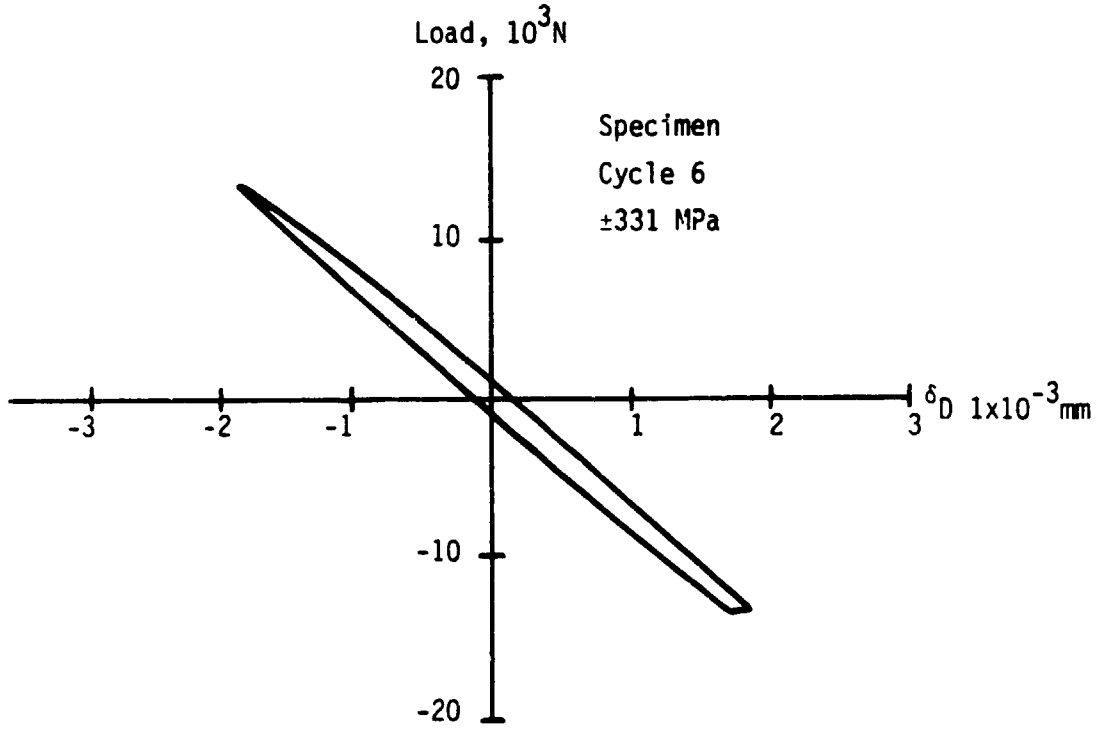

FIGURE 7.10. LOAD VS. NOTCH DIAMETRIAL DISPLACEMENT, TEST B5, FULLY REVERSED, 331 MPa, ONE MINUTE HOLD COMPRESSION.

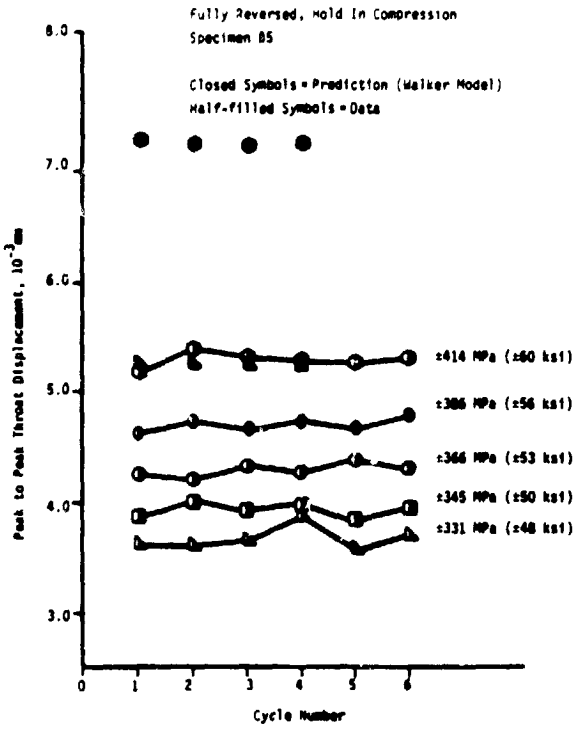

(a)

FIGURE 7.11. (a) PEAK TO PEAK NOTCH DISPLACEMENT, TEST B5, FULLY REVERSED, ONE MINUTE HOLD COMPRESSION.

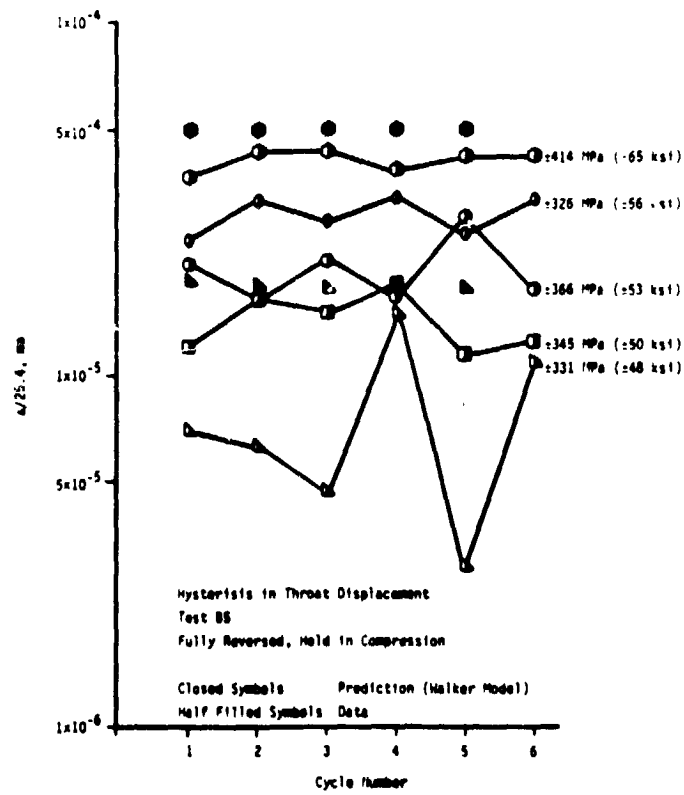

(b)

FIGURE 7.11. (b) CYCLIC NOTCH INELASTIC DISPLACEMENT, TEST B5, FULLY REVERSED, ONE MINUTE HOLD COMPRESSION.

accumulation of notch displacement with hold time and at the ± 331 MPa (± 48 ksi) load level is presented in Figure 7.12.

The finite element calculation overestimates the peak-to-peak throat displacement by as much as 44%, Figure 711(a). The cyclic inelastic notch displacement is also overestimated at the ± 414 MPa (± 60 ksi) load level by 22%, Figure 7.11(b). A constant load hold for one minute in compression results in slightly more predicted diametrial expansion at both load levels than observed in the data. A positive drift in the mean cyclic notch displacement with increasing test cycles and load level is predicted, contrary to test results in Figure 7.12.

d) **Fully Reversed Cycling with a One Minute hold in Tension and Compression (Specimen B6)**

The specimen was cycled with a one minute hold in both tension and compression. The variation of the peak to peak notch displacement and the cyclic inelastic notch displacement with the cycle number is shown in Figures 7.13(a) and 7.13(b), respectively. No cyclic hardening is noted in the response. The variation with time of the notch displacement during the tensile hold at both ± 331 MPa (± 48 ksi) and ± 414 MPa (± 60 ksi) load levels is presented in Figure 7.14. Results for the compression hold are presented in Figure 7.15. Note that the notch strain resulting from a tensile hold was not totally recovered during the compression portion of the cycle and a negative drift in the mean hoop strain occurs at all load levels with increasing cycles.

As noted in Figures 7.13(a) and 7.13(b) the finite element analysis predicts the peak-to-peak variation in the throat diametrial displacement to within 14%, but underestimates the cyclic inelastic notch displacement by

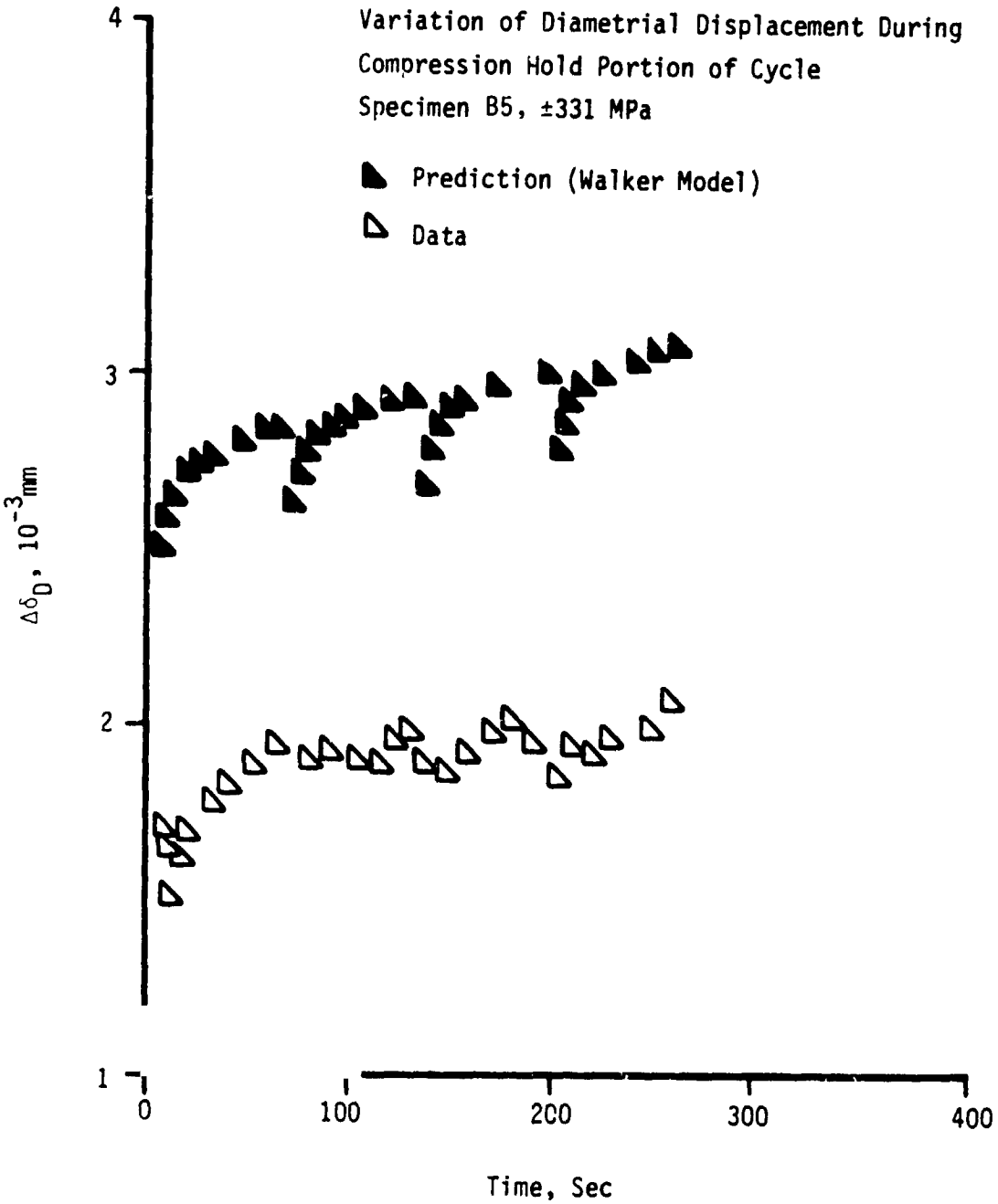

FIGURE 7.12. VARIATION OF NOTCH DIAMETRIAL DISPLACEMENT DURING COMPRESSION HOLD, TEST B5, FULLY REVERSED, ONE MINUTE HOLD TENSION AND COMPRESSION.

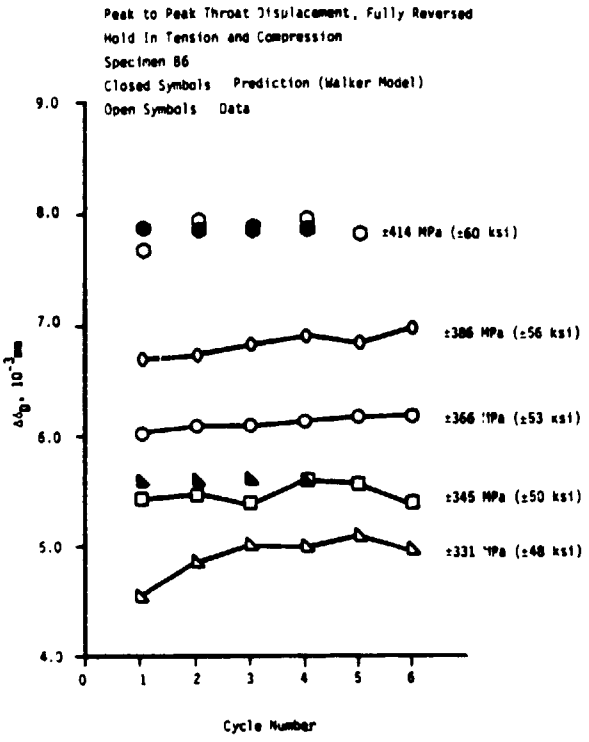

(a)

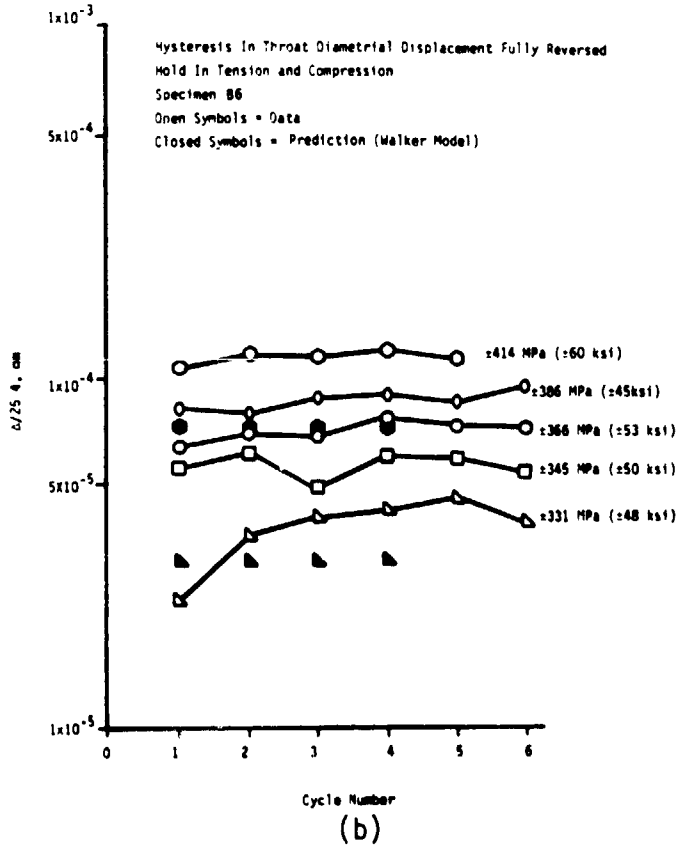

(b)

FIGURE 7.13. (A) PEAK TO PEAK NOTCH DISPLACEMENT, TEST B6, FULLY REVERSED, ONE MINUTE HOLD TENSION AND COMPRESSION AND (B) CYCLIC NOTCH INELASTIC DISPLACEMENT, TEST B6, FULLY REVERSED, ONE MINUTE HOLD TENSION AND COMPRESSION.

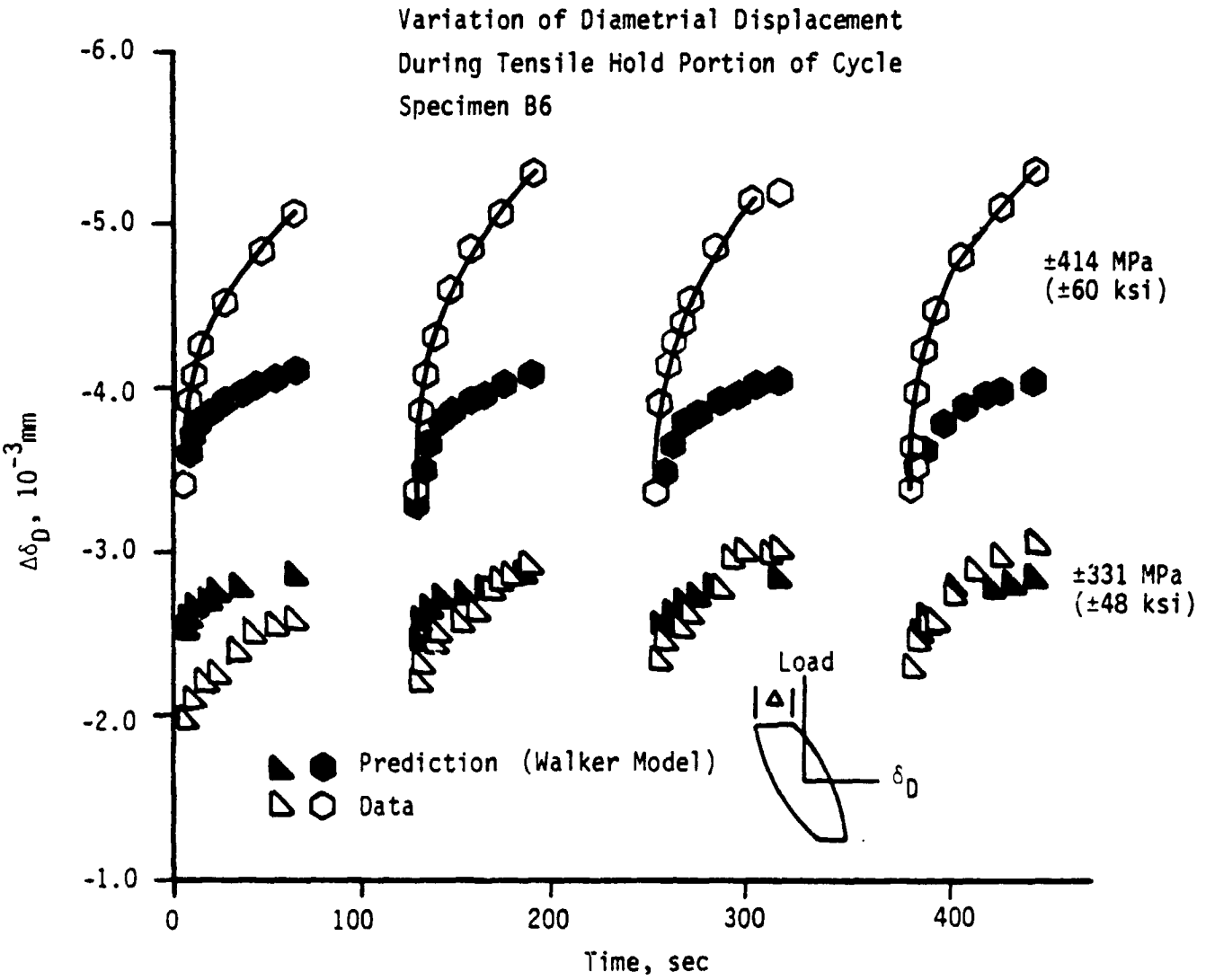

FIGURE 7.14. VARIATION OF NOTCH DIAMETRIAL DISPLACEMENT DURING TENSILE HOLD, TEST B6, FULLY REVERSED, ONE MINUTE HOLD TENSION AND COMPRESSION.

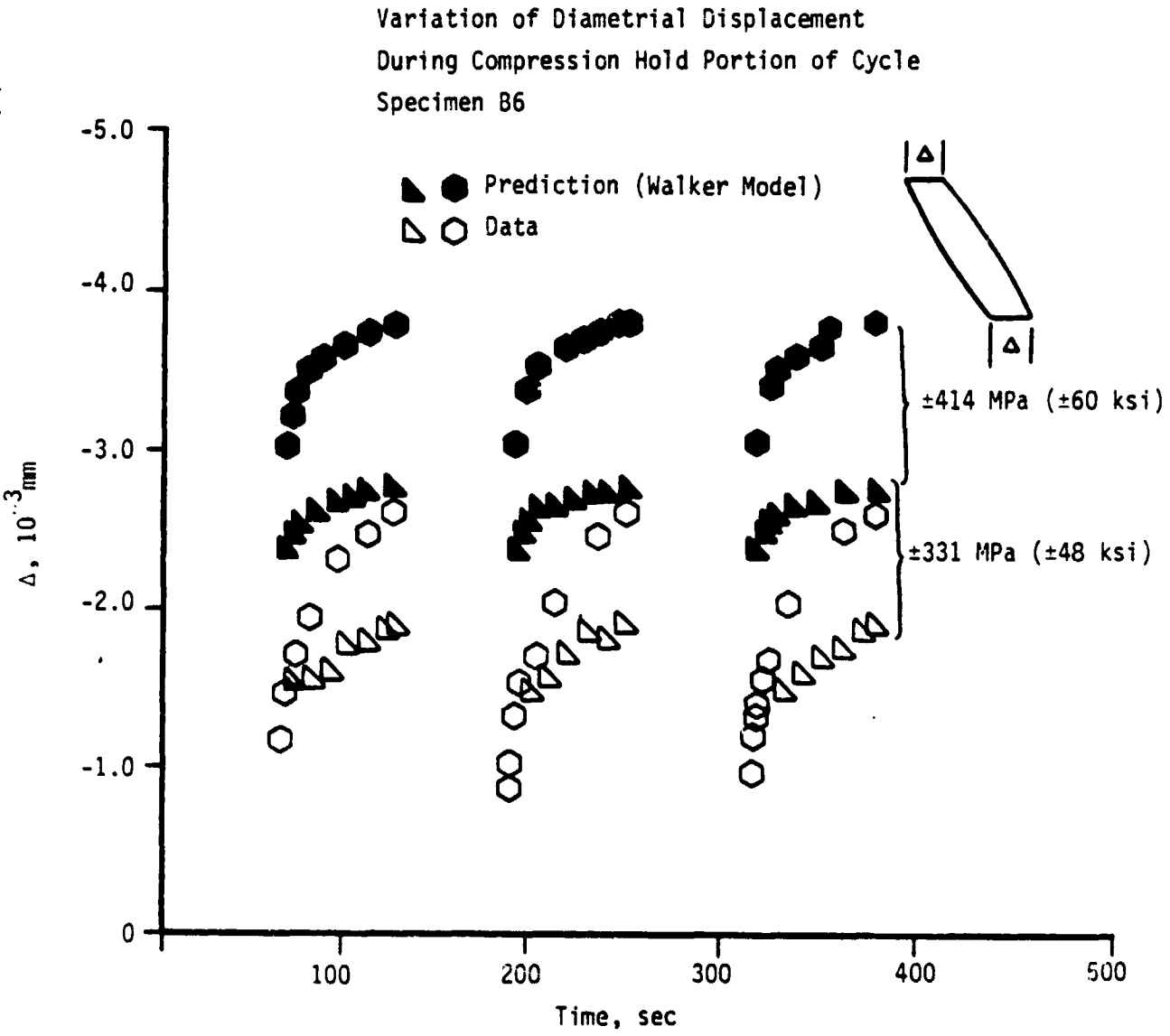

FIGURE 7.15. VARIATION OF NOTCH DIAMETRIAL DISPLACEMENT DURING COMPRESSION HOLD, 331 and 414 MPa, TEST B5, FULLY REVERSED, ONE MINUTE HOLD COMPRESSION.

nearly 60% at the highest test loads. The change in the throat displacement during the tensile and compressive holds, Figures 7.14 and 7.15, is well predicted at ± 331 MPa but is underestimated at ± 414 MPa.

e) Monotonic Tension (Specimen B3)

The variation in the displacement at the notch throat with specimen load level during the initial portion of the test is presented in Figure 7.16. At the imposed nominal strain rate of 2×10^{-5} sec^{-1} the limit load was 35,800N (8050 lb). Finite element load versus throat displacement predictions track the test data initially but diverge at strain conditions indicative of bulk yielding in the notch. The limit load is overestimated by 18%.

f) Stepped Load Tension with Dwell (Specimen B7)

The specimen was loaded to 379 MPa (55 ksi) and uploaded in 34.5 MPa (5 ksi) increments to a maximum load of 517 MPa (75 ksi). A 15 minute hold was applied at each load level. The change in the displacement at the notch throat during the initial and subsequent load changes is presented in Figure 7.17. The change in the displacement at the notch throat during the tensile hold is presented in Figure 7.18. The data is ordered well with increasing load level except at the initial load level.

The finite element analysis performed to simulate the test underestimates the diametrial displacement in the notch both during the fifteen minute holds and during the subsequent load change by as much as 50%.

7.3 Discussion

Failure to correlate results of a particular benchmark notch test against a finite element analysis may not be attributed solely to deficiencies

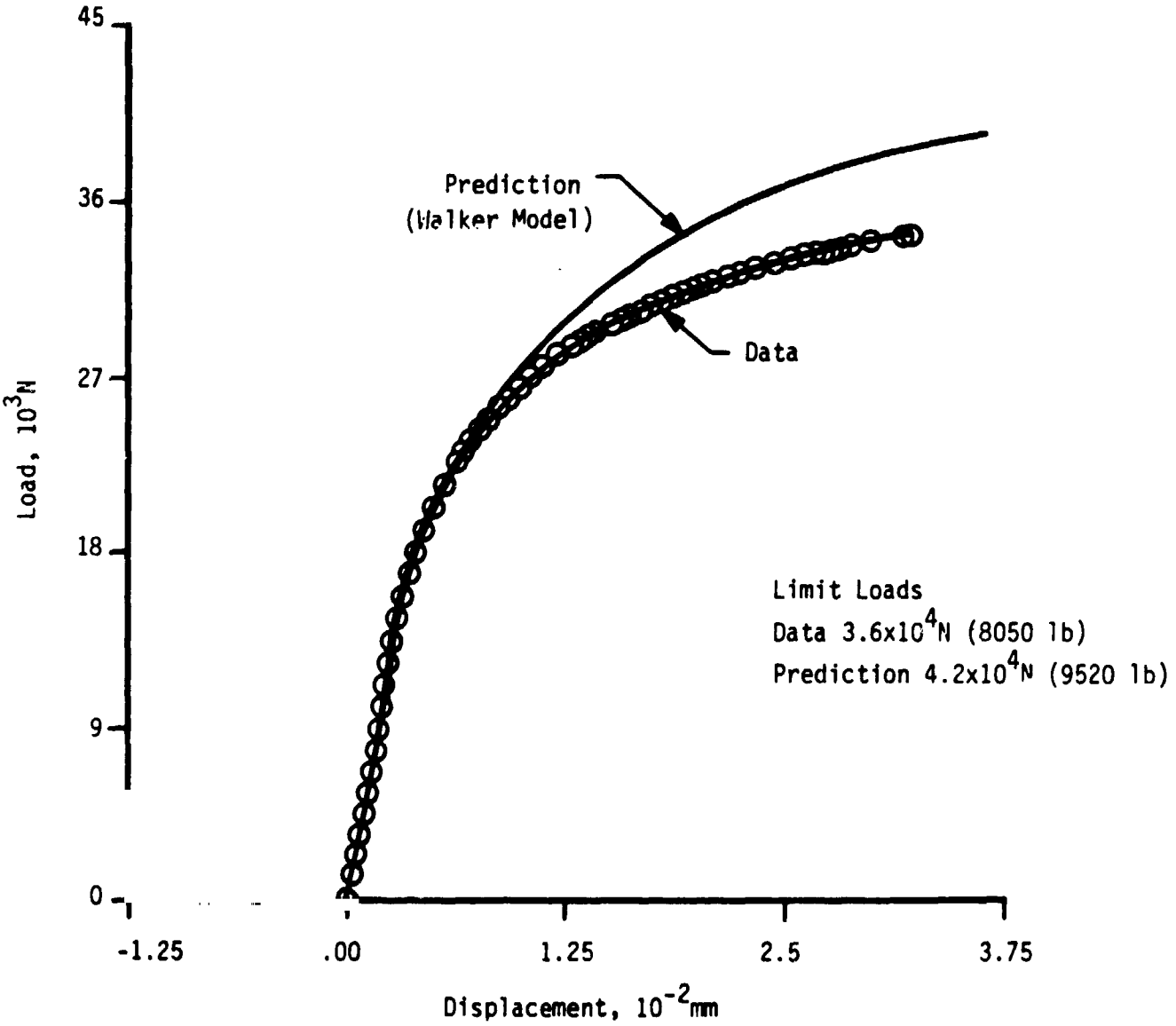

FIGURE 7.16. LOAD VS. NOTCH DIAMETRIAL DISPLACEMENT, TEST B3, MONOTONIC TENSILE TEST.

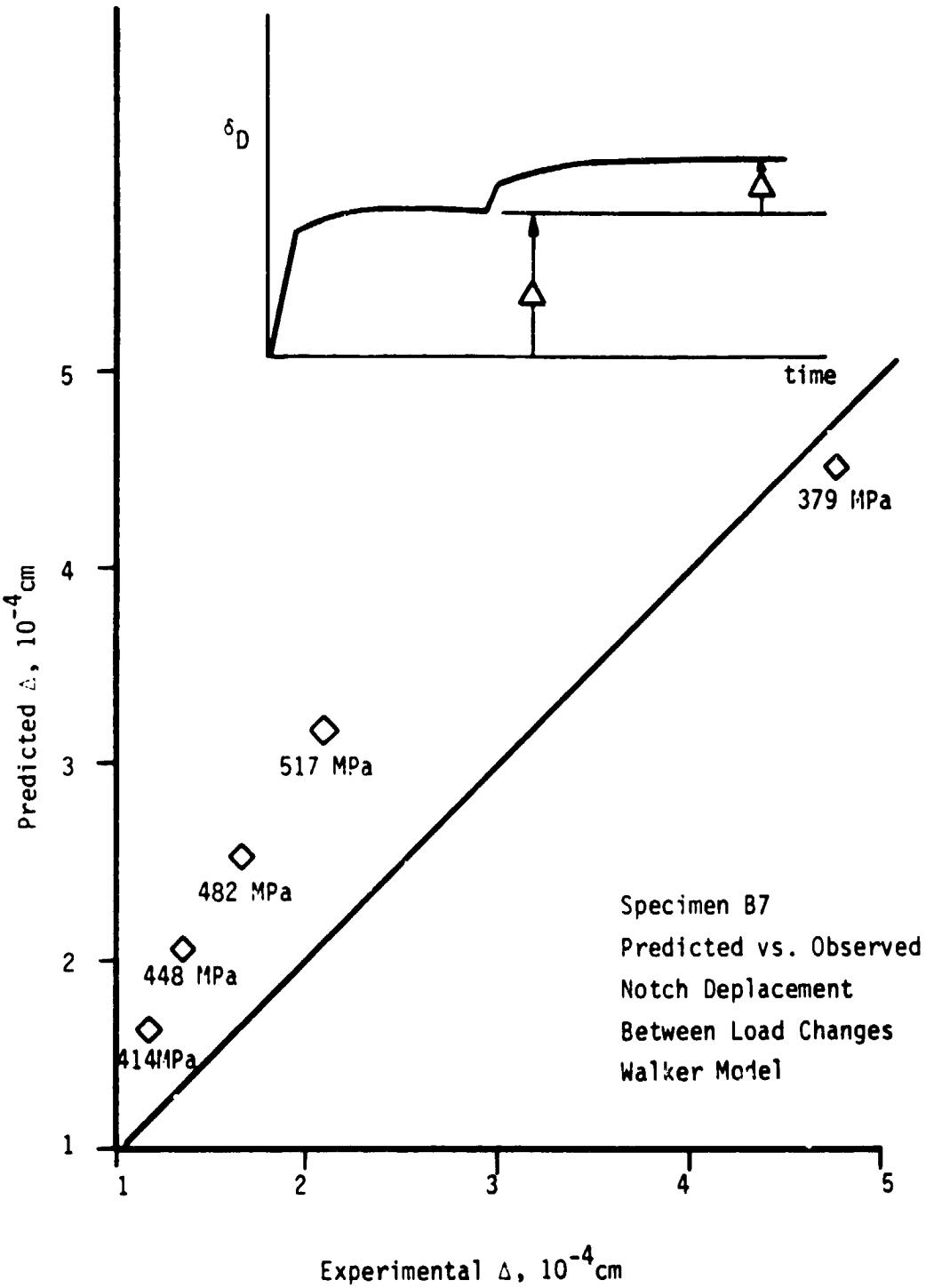

FIGURE 7. 17. PREDICTED VS. OBSERVED NOTCH DISPLACEMENT DURING LOAD CHANGE, SPECIMEN B7, STEP LOAD TENSILE TEST.

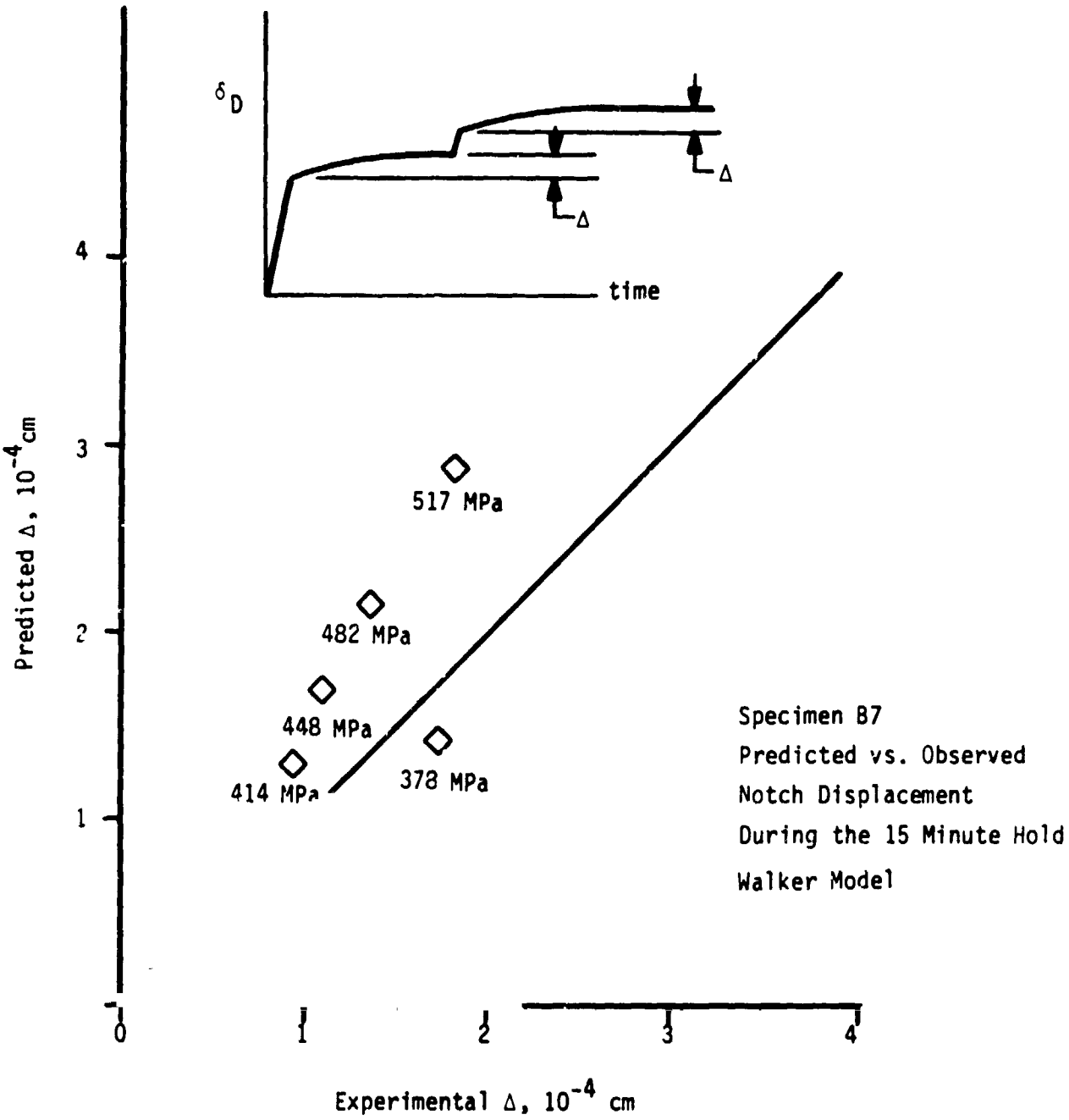

FIGURE 7.18. PREDICTED VS. OBSERVED VARIATION OF NOTCH DIAMETRIAL DISPLACEMENT DURING 15 MINUTE HOLD, TEST B7, STEP LOAD TENSILE TEST.

in the form of the constitutive model, assumed model constants, or finite element methodology. Experimental uncertainties and bar to bar scatter in material properties must also be considered in the assessment. Following is a discussion of these sources of error.

The variation of the notch displacement from bar to bar at low, nearly elastic load levels when normalized by the apparent modulus as determined from the longitudinal displacement measurements, should be a reasonable measure of the precision with which notch strains can be measured. Uncertainty in the notch strains may be introduced when displacement measurements are obtained between two points spanning too few grains or grains of acicular shape. The load-notch displacement response of each specimen was evaluated at elastic notch conditions and the apparent compliance established. Results, corrected for modulus differences, are presented in Table 7.6 for each of the six tests. Note that the apparent elastic diametrical compliance varies by up to 50% relative to the analytical prediction. Easy accessibility of the notch and the high level of reliability and precision of conventional extensometry implies that the source of the variability in the notch elastic deflection may be related to the structure of the material; in particular, the grain size, and/or shape of the grains in the vicinity of the notch.

The assessment is consistent with metallographic obtained by sectioning of the notch specimen, shown in Figure 7.19, which reveals that the number of grains across the cross-section of the notch is relatively small and the grain size is large compared to the notch radius.

The scatter in creep and tensile properties from bar to bar is an important consideration in evaluating the finite element simulation of the test results. To estimate the expected variability in the benchmark test data, a

TABLE 7.6

BENCHMARK NOTCH DATA CORRELATION WITH FINITE ELEMENT PREDICTIONS

Specimen	Relative Elastic Compliance*	Relative Hysteresis Width*	Relative Creep Deflection During Hold*
B1 Cyclic	1.3	.20	-
B3 Monotonic	-	-	-
B4 Cyclic	1.49	.83	1.27
B5 Cyclic	.90	.62	.76
B6 Cyclic	1.01	1.45	2.06
B7 Monotonic	1.37	.75	.76

* Actual Value/Predicted Value

FIGURE 7.19. A SECTIONAL VIEW OF THE NOTCH INDICATES THE PRESENCE OF LARGE STRAINS AT THE NOTCH ROOT.

statistical analysis was performed to examine the scatter in material properties from bar to bar. Stationary strain rate data from constant strain rate tensile tests at different strain rates were regressed to obtain a best fit at 871°C. A Weibull analysis of these data normalized by the regression predictions to obtain the material property scatter is shown in Figure 7.20 along with the the 5 and 95% confidence limits. To verify this estimated cumulative distribution, an analysis was performed on ten fatigue specimens with strain holds at 871°C. Of these ten, three were run with one-minute tensile strain holds and seven with one-minute compressive strain holds. All ten were run with a completely reversed strain range of .5% at a loading frequency of 10 CPM. Two measures of inelastic material behavior were extracted from these tests. The measures were: 1) inelastic strain range at zero stress and 2) the amount of stress relaxation which occurred during the one minute constant strain hold. Each of these measures were normalized by its average for the 10 tests and the results compared in Figure 7.21 with the best fit Weibull distribution taken from Figure 7.20. This second analysis confirms the original analysis of the creep and tensile data and lends assurance that the latter may be compared to the benchmark notch data and finite element predictions.

Table 7.6 presents two measures of the quality of the data correlation: (1) the relative width of the hysteresis loop in a cyclic test or the degree of nonlinear response during a load change in a monotonic test defined by the notch diametrial displacement versus load response, and (2) the relative notch diametrial "creep" during the cyclic or step load test. Each entry represents the average value of the parameter when MARC analysis was performed

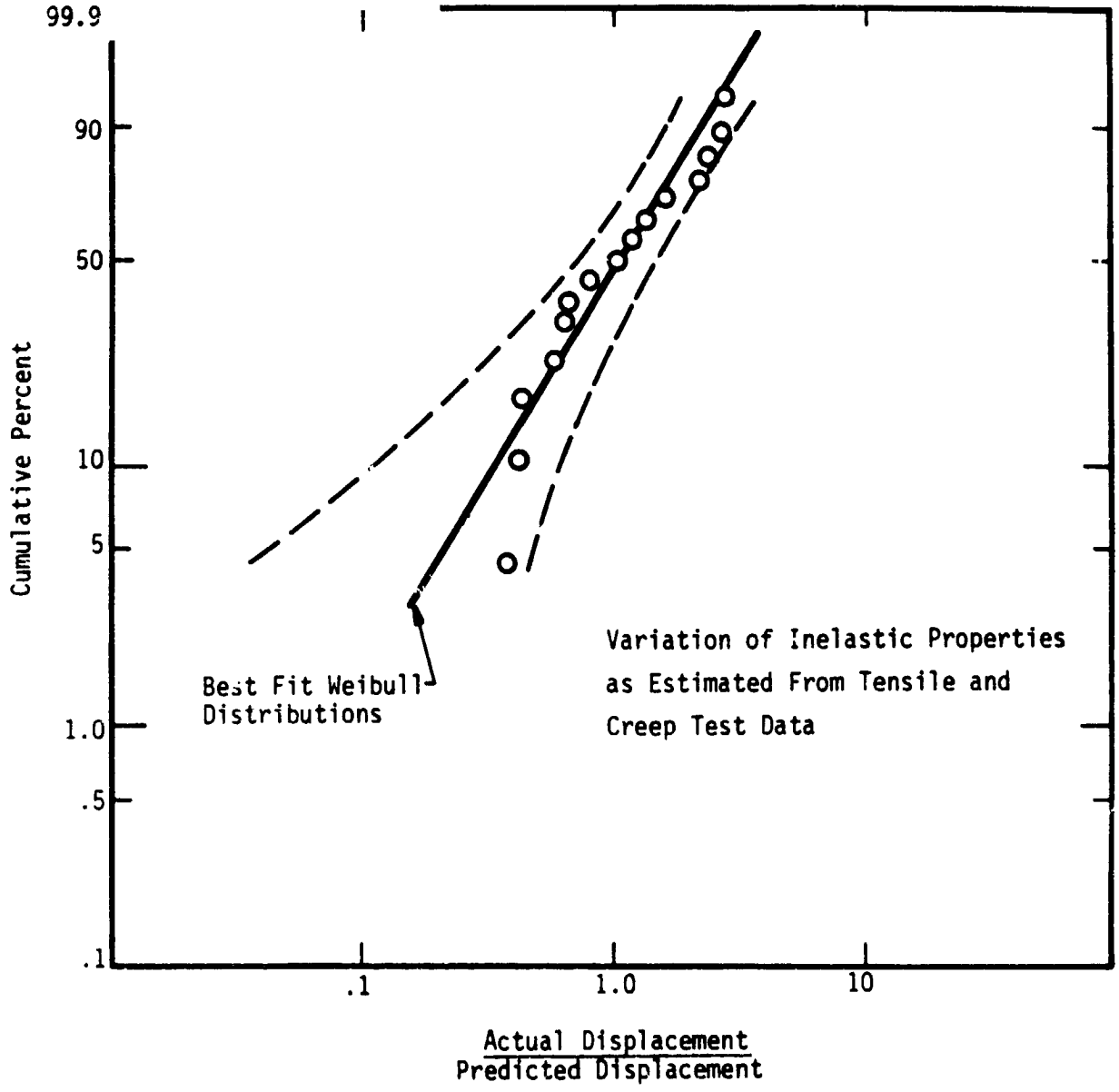

FIGURE 7.20. STATISTICAL ANALYSIS OF CREEP DATA.

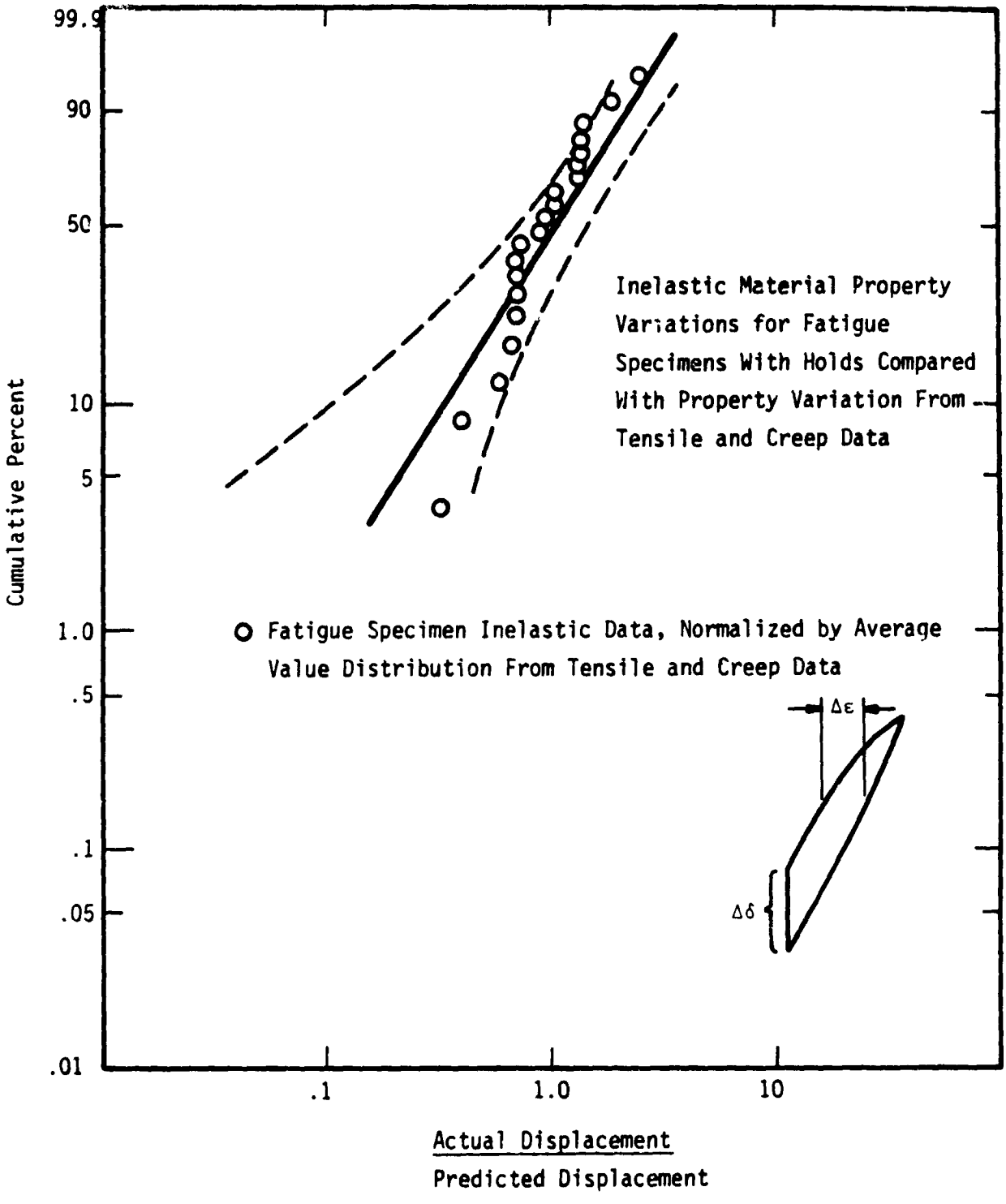

FIGURE 7.21. STATISTICAL ANALYSIS OF FATIGUE DATA.

at more than one load level. A statistical analysis of these data is presented in Figure 7.22 and 7.23. Note that the scatter in results is consistent with that noted in the smooth creep and tensile data. On average, the value of the notch displacement during constant load holds is predicted, Figure 7.22, but the cyclic inelastic displacement or total inelastic displacement during the monotonic tests is overestimated, Figure 7.23. Additional fully reversed, no hold, notched round cyclic tests should be performed to confirm the variability in material properties.

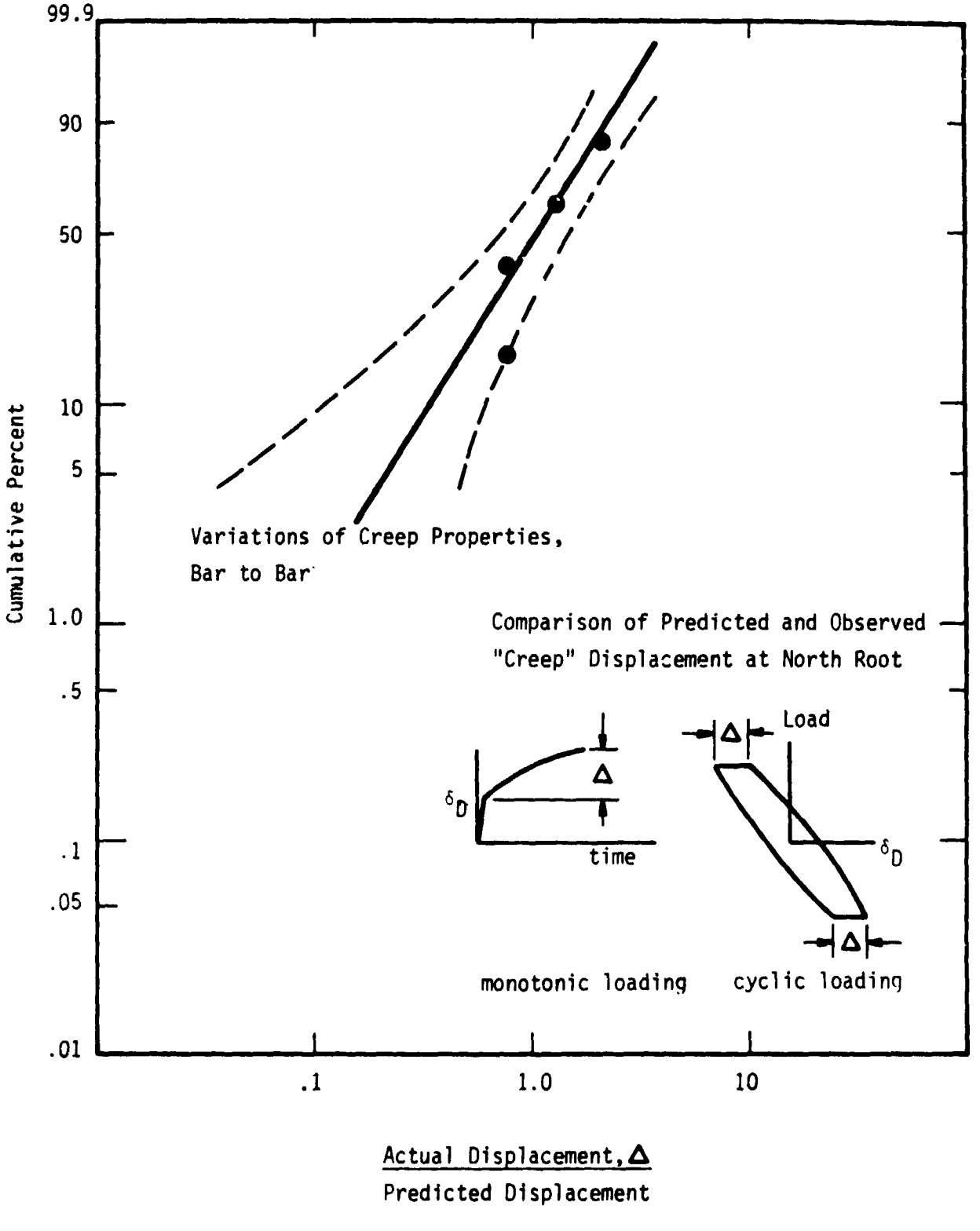

FIGURE 7.22. STATISTICAL ANALYSIS OF PREDICTED AND OBSERVED CREEP DISPLACEMENT AT NOTCH ROOT.

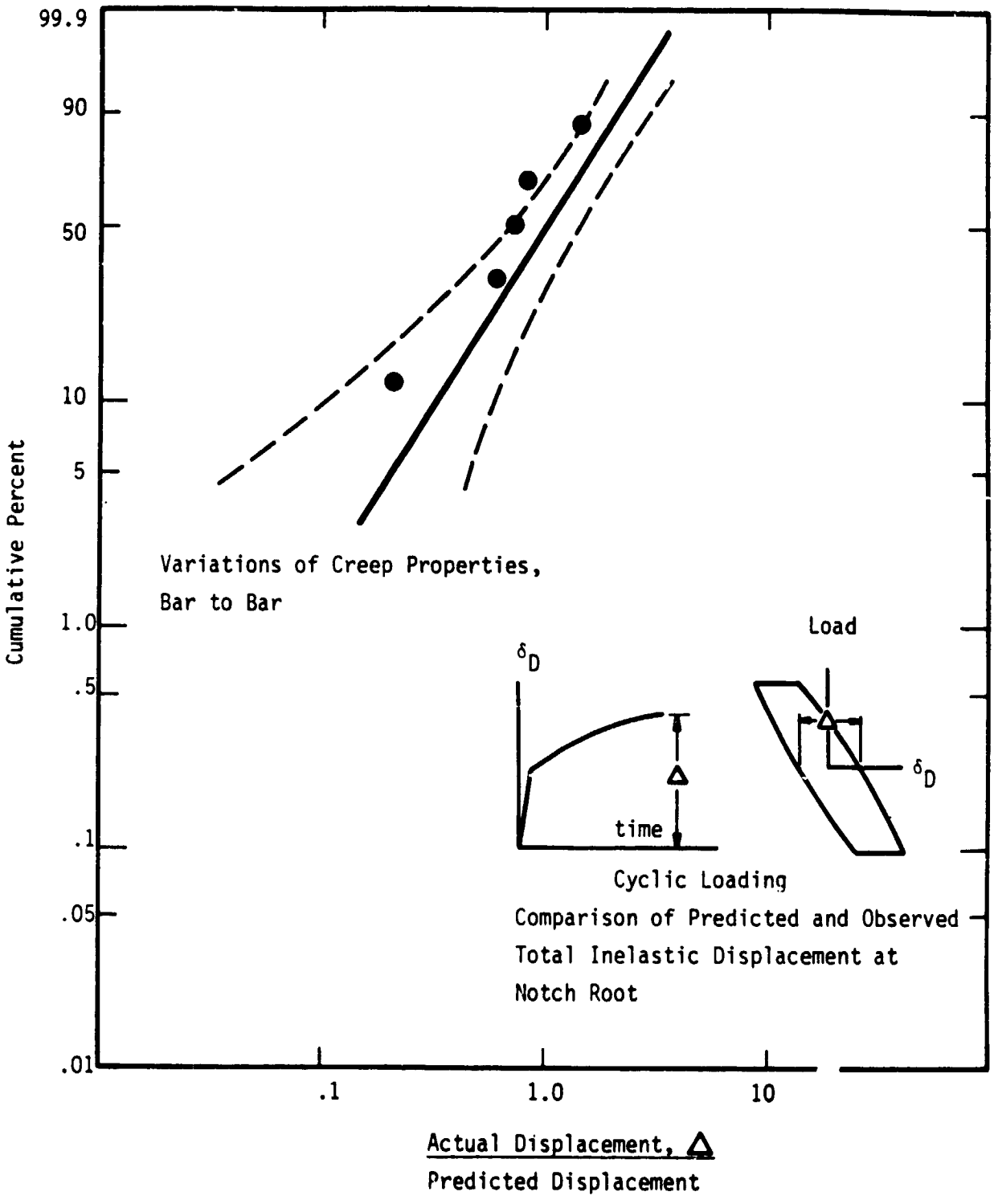

FIGURE 7.23. STATISTICAL ANALYSIS OF PREDICTED AND OBSERVED TOTAL INELASTIC DISPLACEMENT AT NOTCH ROOT.

8.0 HOT SECTION COMPONENT ANALYSIS

The airfoil section of a typical cooled turbine blade has been selected for demonstration analysis of one of the two constitutive models developed in this contract. Figure 8.1 depicts the finite element mesh selected for the analysis. The mesh includes two features which are intended to demonstrate the versatility of the constitutive model and its practical application to actual hot section components.

Two element types are used, as shown in Figure 8.1. A segment of the leading edge is modelled with higher order solid elements (MARC element Type 21) while the remainder of the airfoil is modelled with simpler elements (MARC element Type 7). Appropriate node tying equations are included in the finite element input stream to insure proper compatibility at the interface of the two element types. This technique of mesh refinement is commonly employed in structural analysis to reduce computing time and costs. Inclusion of two element types in the demonstration will illustrate the proper modular formulation of the constitutive model.

The second feature of the model is the simulation of internal features of the component by modifying the density and stiffness of certain mesh elements, Figure 8.2. The internal features being modelled in this case are small ribs connecting the two walls of the hollow airfoil. Of course, if detailed stresses and strains near these features and on a size scale comparable to the features are desired, a much more refined mesh would be required or the region would have to be subsequently analyzed using boundary conditions obtained from the cruder mesh. Inclusion of this feature demonstrates the ability of the model to be adapted for specialty use.

The computations using the MARC code with the Walker constitutive model are currently underway at PWA. The results will be included in a report to be issued separately.

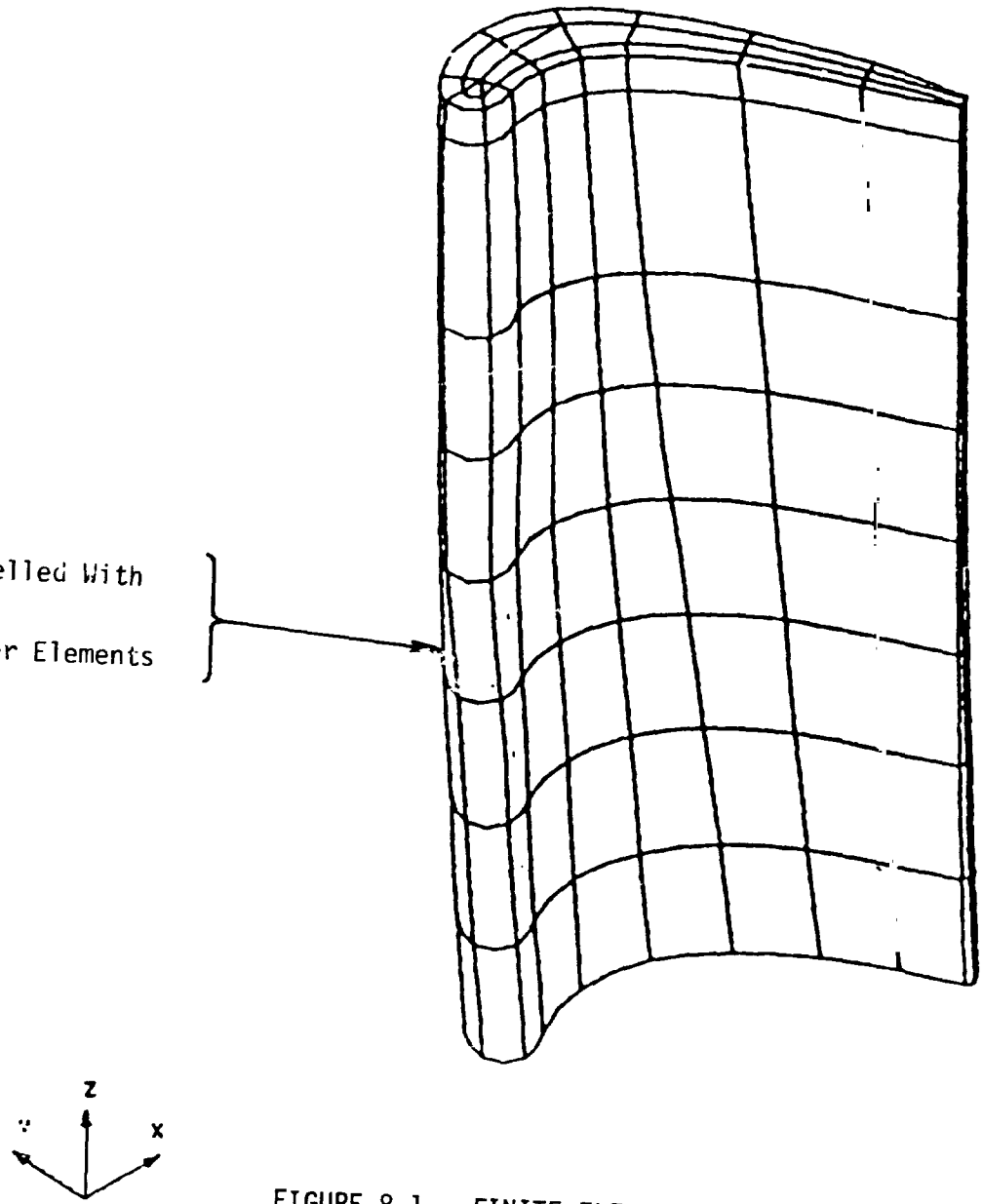

FIGURE 8.1. FINITE ELEMENT MESH USED FOR CONSTITUTIVE MODEL DEMONSTRATION.

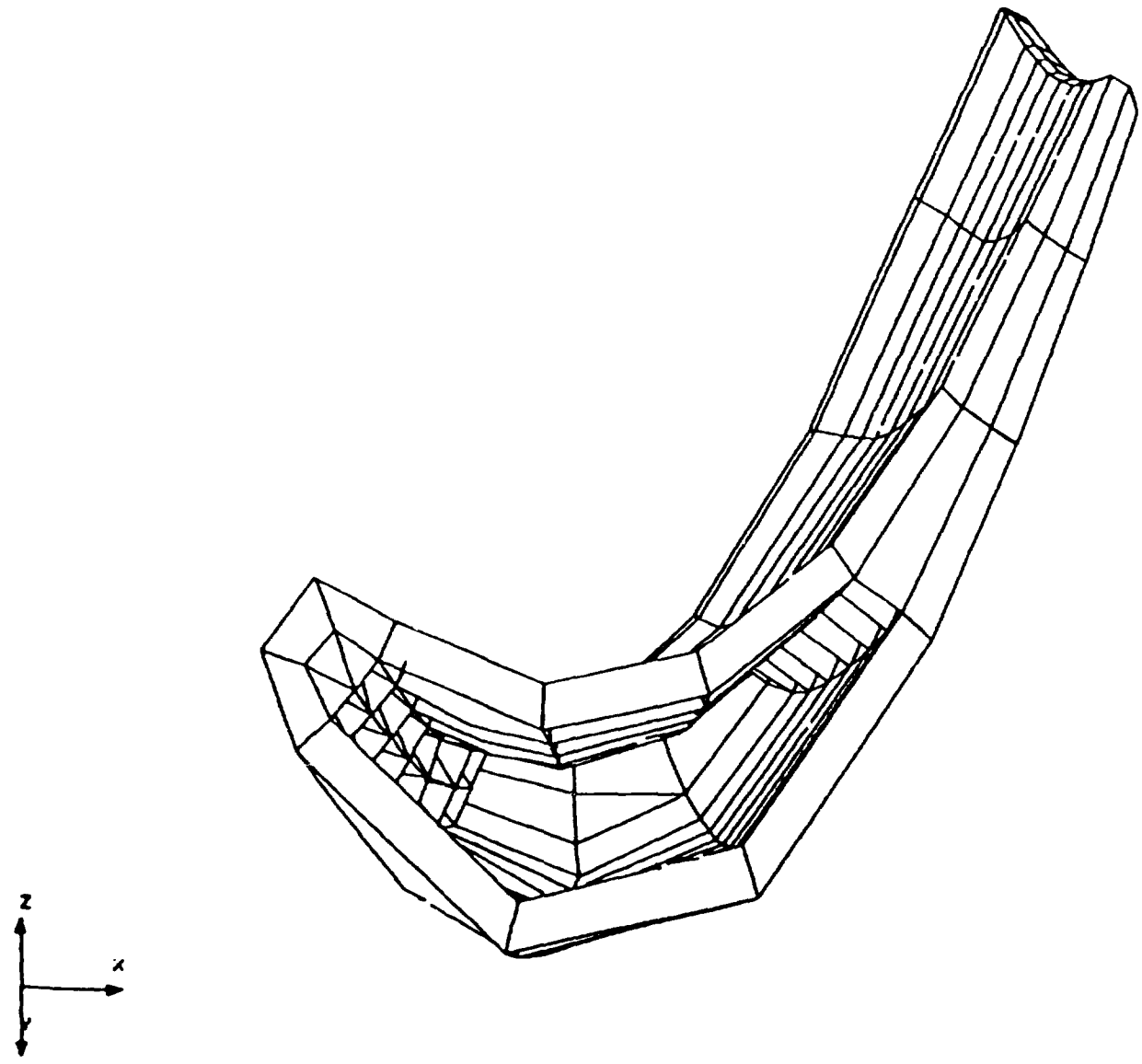

FIGURE 8.2. RADIAL VIEW ILLUSTRATING INTERNAL FEATURES OF THE HOLLOW AIRFOIL.

9.0 OVERALL EVALUATION OF CONSTITUTIVE MODELS

As indicated earlier [1], the unified constitutive equations have some common properties and some essential differences. In order to evaluate their relative merits, it is useful to keep in mind some basic characteristics that such equations should possess for the purpose of engineering applications. Some of these are the following:

(1) General Admissibility - the equations must be fundamentally correct from the viewpoint of the basic principles of thermodynamics and continuum mechanics. The equations should be consistent with the fundamental physics of elastic and inelastic deformation mechanisms and thereby be able to represent response properties over a wide range of strain rates, temperatures, and loading conditions with minimum alteration of the basic equations.

(2) Range of Applicability - the equations should be capable of representing essential material response characteristics such as strain rate sensitivity of plastic flow, microplasticity (i.e., small plastic straining at low stress levels), isotropic and directional hardening, thermal recovery of hardening, creep and stress relaxation, cyclic hardening and softening, cyclic creep and relaxation, temperature and pressure dependence of plastic flow, and, if applicable, temperature history effects.

(3) **Material Data Requirement** - the equations should contain a relatively small number of identifiable material constants which are determinable from standard test data. It is preferable, but not essential, that the material constants be amenable to physical interpretation.

(4) **Accuracy** - the equations must be capable of making accurate predictions of constitutive behavior. A high level of accuracy is required not only for the simple cases to which the constitutive models are fitted but also for cases of complex loading histories for which data are not used in the determination of the material constants.

(5) **Integrability** - the equations should be capable of being incorporated into standard finite element structural programs in a direct manner.

These five criteria will be used to evaluate the overall performance of the Bodner-Partom and the Walker models.

(1) **General Admissibility:**

Both the Bodner-Partom and the Walker models appear to be fundamentally correct from the mechanics and thermodynamics viewpoint and are consistent with the overall elastic and inelastic deformation mechanisms. The modified Walker model utilizes an exponential function for the kinetic equation relating the inelastic strain rate to the stress and the internal variables. This function is similar, but not identical, to that used in the Bodner-Partom model. The form of the evolution equation for the isotropic

hardening variable is also similar for both models, with the exception that thermal recovery is not included in the Walker model. The main differences in the two models are in the flow law and the treatment of directional hardening. Comparison of model calculations with experimental data, however, reveals no practical difference in the ability of both models to predict cyclic behavior of B1900+Hf subjected to uniaxial and multiaxial loading under both proportional and nonproportional strain paths.

Theoretically, the Walker model, which is based on the equilibrium stress, is expected to be capable of modeling reversed creep, reversed stress relaxation, and a phase angle between the inelastic strain rate and the deviatoric stress vectors. On the other hand, stress relaxation and nonproportional multiaxial calculations and test results indicate that the lack of these potential capabilities in the Bodner-Partom model are not severe liabilities. For example, the stress relaxation results of the Bodner-Partom model are in quite good agreement with the experimental data for B1900+Hf even though the small amount of reversed stress relaxation observed in the data is not predicted. The practical importance of the phase lag in non-proportional loading requires further evaluation.

(2) Range of Applicability:

On the basis of this investigation, it appears that the range of applicability of the Bodner-Partom and the Walker models is quite broad. It is noted that the present investigation is limited to the relatively slow to moderate strain rate range (10^{-7} - 10^{-3} sec^{-1}) and that extension of the study to high strain rates would be of interest. For uniaxial loading, both models can be used for modeling: (1) monotonic stress-strain behavior, (2) creep behavior, (3) cyclic stress-strain behavior, (4) stress-relaxation behavior, and

(5) thermomechanical constitutive behavior. For multiaxial loading, both theories are capable of modeling inelastic response under complex loading histories involving either proportional and/or nonproportional loading paths. Because of this wide range of applicability, both theories demonstrate that the unified concept is a viable approach for modeling time-temperature dependent inelastic deformation. The Walker model, however, suffers from the drawback that it requires considerable modifications when the theory is applied to different structural alloys. This deficiency is evidenced by comparing the version of the Walker model for Hastelloy-X [3] to that for the B1900+Hf used in the present program.

(3) **Material Data Requirement**:

Both the Bodner-Partom and the Walker theories require only a limited data base for model constant determination. All the Bodner-Partom model constants, except α_1, can be evaluated from uniaxial tensile data. The multiaxial data of B1900+Hf indicate no additional cyclic hardening due to nonproportional loading. Since additional cyclic hardening resulting from nonproportional loading has been observed in Hastelloy-X [3] and other structural alloys [14,15], the nonproportional hardening effect is therefore material dependent and must be evaluated on an individual basis. Thus, it appears that some nonproportional multiaxial data would be required for evaluation of certain material constants in any unified constitutive model, e.g. α_1 in the Bodner-Partom model which equals to zero in this case. Material constants in the Walker model can be evaluated from uniaxial tensile, creep and cyclic data, while some nonproportional multiaxial data would also be required for including the nonproportional hardening effect.

The number of material constants that needs to be evaluated from experimental data is roughly the same in the Bodner-Partom and Walker models. A difference between these two theories is that most of the materials constants in the Bodner-Partom theory are temperature-independent, while most of those in the Walker theory are temperature-dependent for B1900+Hf. In addition, the Bodner-Partom model constants can be evaluated more readily and attributed to specific mechanisms. The consequences are: (1) the procedures for evaluating the Bodner-Partom model constants are simpler than for the Walker model, and (2) the data requirement is also less for the Bodner-Partom model.

(4) Model Accuracy:

Despite the fact that only tensile data were used for evaluating material constants, the Bodner-Partom model is as accurate, if not more accurate, than the Walker theory. Both models performed equally well in the tensile data correlation, with the difference that strain aging is included in the Walker model but not in the Bodner-Partom model. In principle, a strain aging term can also be included in the latter model. This high level of accuracy is expected because most of the material constants were determined using the tensile data. The Bodner-Partom model appears to be more accurate than the Walker model in correlating the steady state creep behavior of B1900+Hf. For correlating cyclic response, both models predict the stress and the plastic strain ranges equally well. The shape of the hysteresis loops and the drift of the mean stress are better predicted by the Bodner-Partom model. A rigorous test of the two models appear to lie in the TMF cycle. In all the three TMF cycles examined, both models predict the shape, the stress range, and the stress relaxation behavior associated with the TMF hysteresis loops

quite well. Note that the Bodner-Partom model is quite effective in predicting the stress relaxation behavior of B1900+Hf under both isothermal and TMF conditions. The success of these models in predicting the TMF hysteresis loops suggests that no additional terms need to be included in the unified constitutive models specifically for the TMF histories. Only the static thermal recovery terms and the variation of material constants with temperature were used in predicting the TMF response of B1900+Hf. Further study of non-isothermal behavior is included in future work.

Both models are able to predict the first cycle mean stress of the stable hysteresis loops of B1900+Hf cycled under an imposed mean strain. In the case of the Bodner-Partom model, the mean stress at the sixth cycle is also predicted in most instances, but the model appears to have difficulties of maintaining a mean stress at small inelastic strain ranges. Under these conditions, both models have difficulties in predicting the drift of the small mean stress over a large number of cycles (10-20 cycles).

Neither model is capable of predicting the hysteresis loops with dwell under load-controlled conditions. The discrepancies can be explained on the basis that load-controlled tests are more sensitive to material variation. Hardening of B1900+Hf generally saturates rather rapidly and the stress-strain curves level off after a few tenths of one percent of strain so that a slight variation in the material properties would cause a large difference in the plastic strain under load-controlled conditions. As a result, the unified models have difficulties in predicting creep strain as function of time in both the primary and steady-state creep regimes, even though the steady-state creep rate, which is the slope of the creep strain vs. time curve, is predicted fairly accurately.

The viscoplastic model analysis did not yield an adequate prediction of the benchmark notch behavior of B1900+Hf. Material variability is certainly one aspect of discrepancies which need to be considered. Model accuracy may also be a factor. It appears there is a need to perform the same benchmark notch calculations using the Bodner-Partom model in order to have a one-to-one comparison and to examine whether better correlations could be obtained.

(5) Integrability:

The TMF calculations indicate that the Bodner-Partom model required approximately 3 times as much as computer time as the Walker model for performing the same calculations. The stiffness of the Bodner-Partom model is generally attributed to the exponential kinetic equation. Since the modified Walker model also uses a similar, though not identical, exponential equation, it is not clear why the Bodner-Partom calculations require more CPU time. In addition, the Walker model contains more internal variables and evolution equations. The issue of the integrability of the unified models needs to be studied in more detail.

10.0 SUMMARY AND CONCLUSIONS

10.1 Summary

During the base program, the following tasks were accomplished and results obtained:

- o A literature review of existing unified constitutive models for time and temperature dependent inelastic behavior of high temperature alloys was completed. All models contain three essential components - a flow law; a kinetic relationship between stress, inelastic strain rate, internal variables, and temperature; and evolution equations for the hardening variables. Ten different models were compared relative to these components.
- o A review of numerical integration procedures applicable to these "stiff" equations was completed.
- o The particular models of Bodner and Partom and of Walker were selected for detailed study and implementation in a finite element code.
- o The alloy selected for testing under th ase program was cast B1900+Hf. Specimens were fabricated at PWA from a single heat of this material, which included tensile, creep, cyclic, TMF, biaxial, and benchmark notch round specimens.

- Mechanical tests including tensile, creep, cyclic, stress relaxation, TMF and biaxial tests were conducted to generate uniaxial and multiaxial data for correlation and verification of the unified constitutive models developed in this program.
- A systematic approach was developed for evaluating material constants for the Bodner-Partom and for the Walker models.
- Both the Bodner-Partom and the Walker models were used to correlate the uniaxial and multiaxial behavior of B1900+Hf. Correlations include tensile, creep, cyclic, stress relaxation, TMF, and biaxial deformation under simple and/or complex histories. Predictions of the two models are generally in good agreement with experimental data.
- Benchmark notch round data were generated and correlated with the Walker model. Agreement between theory and experiment is less than desirable. Material property variation may be a factor in influencing the agreement between theory and experiment.
- Both models were implemented in the MARC finite element computer code. The in-phase TMF cycle was calculated using both the Bodner-Partom and the Walker models by means of an Euler integration scheme. The former model was found to be numerically less efficient than the latter model in this exercise.

- A hot section component is being analyzed using the Walker model in conjunction with the MARC finite-element computer code. The component being analyzed is the airfoil section of a typical cooled turbine blade. A separate report will be issued describing this analysis.

10.2 Conclusions

The results of this program provide strong evidence for the applicability of the unified constitutive equation approach to describe the strongly nonlinear, time and temperature dependent response of metals to arbitrary load or deformation histories. We believe that the current effort, perhaps the most comprehensive verification of plasticity models to date, has demonstrated positively the essential feature of the "unified" model, i.e., that all aspects of inelastic deformation can be incorporated in a single term. This term is based upon a tensorial relation (flow law) between the deviatoric components of inelastic strain-rate and stress, a scalar kinetic relation expressing the dependence of deformation rate on stress, internal variables and temperature and a set of evolution equations describing both isotropic and directional strain or work hardening. As a minimum, the two models studied were correlative in that they demonstrated reasonable agreement with all the experimental data generated over a very wide range of temperature, deformation rate and load cycle. This was accomplished with a fixed model and fixed set of material constants. In a broader sense, the models were predictive in that the functional representations and the material constants were obtained from a

small subset of the total tests performed. Even better overall correlation could have been achieved if all the data were used to optimize the functions and constants in each model. Some more detailed conclusions follow.

A major criticism of the unified models has been the apparent (and often real) difficulty in defining and experimentally determining the multiple material constants employed in the models. We believe we have made significant progress in this regard. The different terms in the constitutive equations are very interactive so that it is essential to have a physical insight into the meaning of each function and its associated constants. Procedures presented in this report delineate a deterministic method for determining the constitutive constants in a sequential manner from a relatively small material test data base. In the Bodner-Partom model, which is functionally less complex and has fewer material constants than the Walker model, it was possible to identify all the constants for B1900+Hf from a set of monotonic tensile stress-strain curves. Future work will determine if this procedure is more generally applicable and if it is possible to automate the constant determination procedure for a given model.

The additional complexity of the Walker model (and other functionally similar models) resides primarily in the inclusion of the "back stress" or more appropriately designated "equilibrium stress" tensor in the flow law. This is a controversial area. The Bodner-Partom formulation, which does not employ the equilibrium stress formulation, has been shown in this study to be equally satisfactory (in some cases better) than the equilibrium stress form employed in the Walker model. This parity is achieved with fewer material constants. However, more analysis of the data and study is needed of the vectorial relationship between the incremental strains (or strain rate) and the

deviatoric stress. These relationships will be more sensitive to the detailed flow law than are the magnitudes of the independent variables. The biaxial data for B1900+Hf also show some indication of departure from the J_2 based flow criterion assumed in both models. A more complex J_2, J_3 criterion would additionally affect the directional aspects of incremental strains with respect to the applied stress state.

The question as to whether the time integral of plastic strain rate or of plastic work rate or of some other deformation related parameter is the appropriate measure of current state (hardening) is left open. It may well be a material dependent parameter. However, the choice does result in some specific differences in predicted response such as in cross hardening and deformation history dependence.

The current results indicate that properties determined from isothermal tests yield quite accurate results for non-isothermal strain cycling tests, even when the temperature cyclic range includes thermal recovery processes. This result, if general, would reduce the material testing requirements to isothermal only. The need for biaxial testing at this point appears to be material dependent, some alloys showing significant additional hardening under non-proportional biaxial load cycling while B1900+Hf demonstrated equivalent hardening under proportional and non-proportional cycling under the conditions tested. Additional work is needed to determine whether a generalized model can be developed based upon uniaxial test data only. Biaxial testing significantly increases the data generation complexity and cost and, therefore, is not routinely available. Fortunately, the non-proportional biaxial effects are small in most practical applications so that the uniaxial data provides a close approximation.

While the correlative and predictive capacity of the unified models has been demonstrated, their practical application will depend on their adaptability in efficient computational algorithms when incorporated into finite element or other numerical methods for structural analysis. Preliminary use with the MARC finite element code indicates that some improvement is desirable in the numerical integration procedures used with these stiff, nonlinear equations. The computation time for an equivalent problem is approximately the same order of magnitude as when using classical, time-independent plasticity formulations.

11.0 REFERENCES

1. U. S. Lindholm, K. S. Chan, S. R. Bodner, R. M. Weber, K. P. Walker, and B. N. Cassenti, "Constitutive Modeling for Isotropic Materials," Annual Report NASA CR-174718, May 1984.
2. S. R. Bodner and Y. Partom, ASME J. of Applied Mechanics, Vol. 42, p. 385, 1975.
3. K. P. Walker, NASA Contract Report NASA CR-165533, 1981.
4. S. R. Bodner, Mechanical Behavior of Materials Under Dynamic Loads, ed. by U. S. Lindholm, Springer-Verlag, New York, pp. 176-190, 1968.
5. S. R. Bodner and Y. Partom, ASME Journal of Applied Mechanics, Vol. 39, pp. 741-757, 1972.
6. S. R. Bodner and Y. Partom, Proc. Eighth Congress of the International Council of the Aeronautical Sciences, (ICAS), Amsterdam, 1972.
7. S. R. Bodner and Y. Partom, ASME J. of Applied Mechanics, Vol. 42, p. 385, 1975.
8. S. R. Bodner, I. Partom, and Y. Partom, ASME J. Applied Mechanics, Vol. 46, p. 805, 1979.
9. S. R. Bodner, "Evolution Equations for Anisotropic Hardening and Damage of Elastic-Viscoplastic Materials," Proc. Conference on Plasticity Today, Elsevier Applied Science Pub., London, 1984.
10. J. Friedel, "Dislocations," Addison Wesley Pub. Co., pp. 277-279, 1967.
11. B. N. Cassenti, "Research and Development for the Development of Advanced Time-Temperature Dependent Constitutive Relationships," Vol. 1, 2 NASA CR-168191, July 1983.

12. T. G. Tanaka, "A Unified Numerical Method for Integrating Stiff Time-Dependent Constitutive Equations for Elastic/Viscoplastic Deformation of Metals and Alloys," Dissertation, Stanford University, Department of Materials Science and Engineering, 1983.

13. V. Kumar, M. Morjaria and S. Mukherjee, "Numerical Integration of Some Stiff Constitutive Models of Inelastic Deformation," Transaction of the ASME, Journal of Engineering Materials and Technology. Vol. 102, pp. 92-96, January 1980.

14. H. S. Lamba and O. M. Sidebotton, ASME J. of Eng. Mats. and Technology, Vol. 100, p. 96, 1978.

15. N. Nouailhas, H. Policella, and H. Kaczmarek, Proceedings of Int. Conf. on Constitutive Laws for Eng. Materials, edited by C. S. Desai and R. H. Gallagher, Tucson, Arizona, p.45, 1983.

APPENDIX

The main difference in the various unified theories is the treatment of directional or kinematic hardening [1]. Differences exist not only in the choice of the flow law but also in the evolution equations of the internal variables. Two flow laws which are commonly used in the unified models are:

$$\dot{\varepsilon}^{p}_{ij} = \lambda_1 S_{ij} \tag{1}$$

and

$$\dot{\varepsilon}^{p}_{ij} = \lambda_2 (S_{ij} - \Omega_{ij}) \tag{2}$$

with $\dot{\varepsilon}^{p}_{kk} = 0$; $S_{ij} = \sigma_{ij} - \frac{1}{3} \delta_{ij} \sigma_{kk}$

where λ_1 and λ_2 are deformation-history-dependent parameters. S_{ij} and σ_{ij} are the deviatoric and direct stresses, respectively. The tensor Ω_{ij} represents the "equilibrium stress," the directional hardening internal variable which has also been referred to as the "back stress" and the "rest stress."

For uniaxial stress, the flow law represented by equation (1) can be rearranged as:

$$\sigma = f_1 (\dot{\varepsilon}^{p}, T) (K + D) \tag{3}$$

where K and D are the isotropic and directional hardening internal variables, respectively for this form of the flow law. The history dependent parameter,

f_1, is a function of inelastic strain rate and temperature. In a similar manner, the equilibrium-stress-based flow law, Equation (2), can be expressed as:

$$\sigma = f_2 (\dot{\varepsilon}^p, T) K + \Omega \tag{4}$$

$$\text{or} \quad \frac{\sigma - \Omega}{K} = f_2 (\dot{\varepsilon}^p, T) \tag{5}$$

where f_2 is also a function of inelastic strain rate and temperature and is generally different from f_1. An interesting observation of Equation (3) is that stress and internal variables can be scaled using the function f_1. On the other hand, Equation (4) indicates that stress cannot generally be scaled using the function f_2; instead, it is the ratio of the $[(\sigma-\Omega)/K]$ which is scaled by f_2. Thus, the manner in which the direction hardening variable is incorporated in the flow law appears to have significant ramifications on constitutive behavior. The effects are expected to be more complex at elevated temperature because of concurrent hardening and thermal recovery.

The objective of this appendix is to present a comparison of the different approaches for modeling directional hardening including thermal recovery effects. In addition to the flow law, the choice of the hardening measure will also be examined; the plastic work rate will be used in conjunction with Equation (3), whereas the plastic strain rate will be used with the equilibrium stress approach, Equation (4). A procedure for delineating isotropic and directional hardening from uniaxial data will be given.

(A) Low and Intermediate Temperature Behavior without Thermal Recovery

The evolution equations for the isotropic and the directional hardening internal variables without thermal recovery are generally written in a saturation-type format, which can be viewed as a combination of a linear hardening and a "dynamic recovery" term:

$$\dot{K} = m_1 (K_1 - K)\dot{M} \tag{6}$$

$$\dot{\Omega} = m_2 (\Omega_1 - \Omega)\dot{M} \text{ , or, alternatively,} \tag{7}$$

$$\dot{D} = m_2(D_1 - D)\dot{M}$$

where m_1 and m_2 are material constants. K_1 and Ω_1 (or D_1) are the limiting values for the isotropic and the directional internal variables, respectively. The hardening measure, $\dot{M}$, can be either the inelastic strain rate or the inelastic work rate. The dot above the internal variables denotes the rate of change with time.

The approach taken in Equation (3) using the plastic work rate as the hardening measure is first considered. A particular unified model which utilizes this approach is the Bodner-Partom theory [2]. In the absence of thermal recovery and on the physical basis that D saturates much more rapidly than K for most materials, i.e., $m_2 > m_1$, the following approximations to Equation (3) can be made in the region of small plastic strains,

$$K = (\sigma/f_1) - D \approx (\sigma/f_1) - D_1 \qquad (8)$$

and,

$$D = (\sigma/f_1) - K \approx (\sigma/f_1) - K_o \qquad (9)$$

where K_o is the initial value of K. Substituting these approximations in the general expression for $\gamma = d\sigma/dW_p$ obtained from the evolution equations and Equation (3), namely,

$$\gamma = f_1[m_1(K_1-K) + m_2 (D_1 - D)] \qquad (10)$$

leads to

$$\gamma = f_1 [m_1(K_1 + D_1) + m_2 (K_o + D_1)] - (m_1 + m_2) \sigma \qquad (11)$$

This indicates that a plot of γ against σ should be linear with a slope of $m_1 + m_2$ in the range of small plastic strains.

At the larger strains, D fully saturates to the limiting value D_1 so that setting $D = D_1$ and again using Equation (8) for K gives

$$\gamma = f_1 m_1 (K_1 + D_1) - m_1 \sigma \qquad (12)$$

which is a linear relation with slop m_1. These relations indicate that the γ-σ function should be essentially linear at both the low and high plastic strain regimes.

For models based on the equilibrium stress approach and the plastic strain rate as the hardening measure, the general expression for $\theta = d\sigma/d\varepsilon_p$ obtained from the evolution equations and Equation (4) is:

$$\theta = f_2 m_1(K_1 - K) + m_2(\Omega_1 - \Omega) \qquad (13)$$

Using Equation (4), K and Ω at small plastic strains can be approximated as:

$$K = (\sigma - \Omega)/f_2 \approx (\sigma - \Omega_1)/f_2 \qquad (14)$$

$$\Omega = \sigma - f_2 K \approx \sigma - f_2 K_o \qquad (15)$$

Substituting these approximations into Equation (13) leads to

$$\theta = m_1 (f_2 K_1 + \Omega_1) + m_2 (f_2 K_o + \Omega_1) - (m_1 + m_2) \sigma \qquad (16)$$

Assuming Ω saturates to Ω_1 at large plastic strains, setting $\Omega = \Omega_1$ and substituting Equation (14) for K into Equation (13) leads to

$$\theta = m_1(f_2 K_1 + \Omega_1) - m_1 \sigma \qquad (17)$$

Equations (16) and (17) indicate that the θ-σ curve should be linear with a slope of $m_1 + m_2$ at low plastic strains and with slope m_1 at high plastic strain.

(B) High Temperature Behavior with Thermal Recovery

The effect of static thermal recovery can be included by incorporating thermal recovery terms in the evaluation equations of the internal variables. The Orowan-Bailey hardening/recovery format is generally used [1];

$$\dot{K} = m_1 (K_1 - K) \dot{M} - A_1 K_1 \left[\frac{K - K_2}{K_1} \right]^{r_1} \tag{18}$$

$$\dot{D} = m_2 (D_1 - D) \dot{M} - A_2 K_1 \left| \frac{D}{K_1} \right|^{r_2} \tag{19}$$

where K_2 is the fully recovered value of K at a particular temperature T, and K_2 can generally be taken to be K_o, the initial value of K.

The general expression for γ including thermal recovery can be obtained by differentiating Equation (3) with respect to W_p and substituting for $\dot{K}$ and $\dot{D}$, from Equations (18) and (19), giving

$$\gamma = f_1 \left[m_1 (K_1 - K) + m_2 (D_1 - D) \right] - \frac{A_1 K_1^{1-r_1}}{\sigma \dot{\varepsilon}^p} (K - K_o)^{r_1} - \frac{A_2 K_1^{1-r_2}}{\sigma \dot{\varepsilon}^p} |D|^{r_2} \tag{20}$$

For small plastic strains, the approximation Equations (8) and (9) are substituted into Equation (20) and approximating $D_1 \approx D = (\sigma - \sigma_o)/f_1$ in the recovery term, leads to

$$\gamma = f_1 [m_1 (K_1 + D_1) + m_2 (K_o + D_1)] - (m_1 + m_1) \sigma - \frac{A_2 (f_1 K_1)^{1-r_2}}{\sigma \dot{\varepsilon}^p} (\sigma - \sigma_o)^{r_2} \tag{21}$$

with $\sigma_o = f_1 K_o (T)$ (22)

Assuming $A = A_1 = A_2$ and $r = r_1 = r_2$ the rate of work hardening including thermal recovery becomes:

$$\gamma = f_1 [m_1 (K_1 + D_1) + m_2 (K_o + D_1)] - (m_1 + m_2) \sigma - \frac{A (f_1 K_1)^{1-r}}{\sigma \dot{\varepsilon}^p} (\sigma - \sigma_o)^r \tag{23}$$

Usirg a similar procedure, the rate of strain hardening for the equilibrium-stress-based models using the plastic strain rate measure can be derived:

$$\theta = m_1(f_2K_1 + \Omega_1) + m_2\,(f_2\,K_o + \Omega_1) - (m_1 + m_2)\,\sigma -$$

$$\frac{A\,(f_2\,K_1)^{1-r}}{\dot{\varepsilon}^p}\,(\sigma - \sigma_o)^r \qquad (24)$$

It is noted that when A is zero, Equations (23) and (24) reduce to Equations (11) and (16), respectively. This occurs when static thermal recovery is unimportant. Furthermore, Equations (23) and (24) indicate that the slopes of the linear portions of either the γ-σ or the θ-σ curves are drastically changed when thermal recovery is prominent. Thus, it is possible to identify the temperature regime at which static thermal recovery is important by comparing the γ-σ or θ-σ data over a temperature range.

An examination of Equations (11), (16), (23), and (24) also reveals that the hardening expressions derived for the modeling approaches with or without the equilibrium stress concept are of similar forms. In both cases, the hardening rates, γ and θ, decrease with increasing stress linearly at the small and large plastic regimes when thermal recovery is not important and the slopes of these curves are influenced by thermal recovery. Significant results from the theoretical analysis are the observations: (1) the scaling of σ and (K+D) by the function f_1 in the approach without the equilibrium stress and the scaling of $(\sigma-\Omega)/K$ by another function f_2 in the equilibrium

stress approach; (2) scaling of the γ-σ or θ-σ curves by strain rate and temperature through their influence on f_1 and f_2, and (3) the possibility of delineating the isotropic and directional hardening components from uniaxial hardening data on the basis of the linear portions of the γ-σ or θ-σ. It should, however, be noted that despite many similarities, the two hardening approaches are different and their respective applicability should be examined with respect to the experimental data. Comparison of the γ-σ and θ-σ curves indicates that the former formulation is more appropriate for B1900+Hf, as demonstrated in Figure 4.7.